UNIVERSITÀ DI PARMA

UNIVERSITA' DEGLI STUDI DI PARMA

DOTTORATO DI RICERCA IN
Scienza e Tecnologia dei Materiali

CICLO XXXVI

High Pressure/High Temperature synthesis of novel functional perovskites and their structural, magnetic, and electrical characterizations

Coordinatore:
Chiar.mo Prof. Enrico Dalcanale
Tutor:
Chiar.mo Dr. Edmondo Gilioli

Dottorando: Chiara Coppi

Anni Accademici 2020/2021 – 2022/2023

UNIVERSITÀ DI PARMA

UNIVERSITA' DEGLI STUDI DI PARMA

DOCTORAL COURSE IN
Materials Science and Technology

Cicle XXXVI

High Pressure/High Temperature synthesis of novel functional perovskites and their structural, magnetic, and electrical characterizations

Coordinator:
Chiar.mo Prof. Enrico Dalcanale
Supervisor:
Chiar.mo Dr. Edmondo Gilioli

Candidate: Chiara Coppi

Academic Years 2020/2021 – 2022/2023

“Structure solution from Powder Diffraction Data is difficult but must stay a fun! If it does not work, let it sleep and come back a few days (weeks) later. It will work! You must like your unit cell! Nature has prepared many challenges for us. Enjoy it when you discover one!”

Prof. Radovan Černý

Hercules School 2023, Grenoble

Chiara Coppi

chiara.coppi@unipr.it
chiara.coppi@cnr.it

Department of Chemical Sciences, Life and Environmental Sustainability

Università degli Studi di Parma

Parco Area delle Scienze 17/A

I-43124 Parma, Italy

Institute of Materials for Electronics and Magnetism (IMEM)

Research National Council (CNR)

Parco Area delle Scienze 37/A

I-43124 Parma, Italy

Tables of Contents

1 Introduction

One crucial task of material science is to discover and develop innovative and applicable compounds which could improve everyday life quality. In concrete terms, this means that material scientists have to face several complex challenges, trying to master and manipulate fundamental science principles, explain and tune the emerging phenomena that occur, and hopefully fill the gap through the final implementation of a designed device.

Functional materials represent one of the main characters of significant breakthroughs in many fields like engineering, electronics, and energy. Specifically, to cover such a wide range of applications, functional materials possess exotic properties for instance semiconductivity, thermoelectricity, ferroelectricity, piezoelectricity, magnetism, photovoltaic effect, photo/electrocatalytic effect or gas sensitivity. Moreover, starting from these promising compounds, material science is nowadays aiming to tune or merge more than one functionality, creating the so-called multifunctional materials, such as the multiferroics or the ferro-photovoltaics, in which coexistence of two properties makes them very useful for creating single devices able to satisfy simultaneously different requirements.

In this framework, one of the most widespread and versatile systems which displays functional or multifunctional properties is represented by the inorganic perovskite oxides, with the general chemical formula ABO_3. Thanks to their wide tolerance to chemical substitutions, particularly on the A or B sites, and structural distortions of BO_6 octahedra in the crystal system, perovskite systems constitute a rich playground in which novel potential compounds suitable for application can be explored.

The current PhD thesis deals with the synthesis of new double perovskites in the form $AA'BB'O_6$ under high pressure/high temperature conditions through the use of a Multi-anvil Walker-type press which allows reproducing the extreme thermodynamic conditions that can be found in the Earth's crust in order to force and stabilize unusual phases that cannot be created in conventional ambient conditions. The aim is to obtain functional or multifunctional perovskites focusing on magnetic and electrical properties. Herein, the optimization of the synthesis conditions is discussed on the basis of several attempts that I have tried during my PhD, with the consequent characterization of physical properties of these new compounds focusing on the structural, magnetic and electric point of view, with the use of many different techniques that helped me fully understand the potential of my materials. Among them, I was particularly fascinated by crystallographic analysis, with its capability to predict, by first principle, the possible presence of specific macroscopic properties. For this reason, its investigation covers an extensive part of my Thesis, focusing on the combination of different kinds of probe sources in material science to highlight different features in my crystalline structures.

2 Perovskites

2.1 Crystal structure

The perovskite structure, one of the most abundant structural families and discovered for the first time in minerals of calcium titanium oxide in 1839, refers to all those crystalline materials that follow the general chemical formula ABX_3. Specifically, the ideal form of the perovskite, reported in Figure 2-1, is characterized by a cubic structure with space group Pm-3m (no. 221). In this configuration, the A site corresponds to the (0,0,0) position, i.e. the vertices of the unit cell, and is usually occupied by a large cation. On the contrary, a smaller cation is located on the B site at the body-centre position (1/2,1/2,1/2). The type X ions are negatively charged, and sit at face-centred positions (1/2,1/2,0), (1/2,0,1/2), (0,1/2,1/2). Although the following discussion can be carried out also for the iodine, bromine, fluoride or chloride cases, in this work I will always refer to oxide perovskites, where the X position is reserved for oxygen. In this way, the B ion is in coordination 6 with X, forming the characteristic BX_6 octahedra, while the A ion has a 12-fold coordination. The cubic perovskite structure is the densest phase of the ABX_3 form and is preferentially stabilized by the pressure effect. It's not surprising that in the Earth's lower mantle, more than 660 km below the terrestrial surface where the pressure ranges between 24 GPa and 127 GPa, the major crystalline compounds that can be found are Mg-, Ca- and Si-based perovskites, which constitute ~80% of its volume. In fact, the pressure lowers the free energy of the compound with respect to that of the starting components, helping the formation of the perovskite phase. Unfortunately, (or not) the ideal cubic unit cell describes only a few numbers of compounds, and some examples are represented by $SrTiO_3$ [1], $CsPbBr_3$ [2], and $CsSnI_3$ [3]. Indeed, the majority of perovskites diffused in nature are characterized by lattice distortions which reduce the number of symmetry

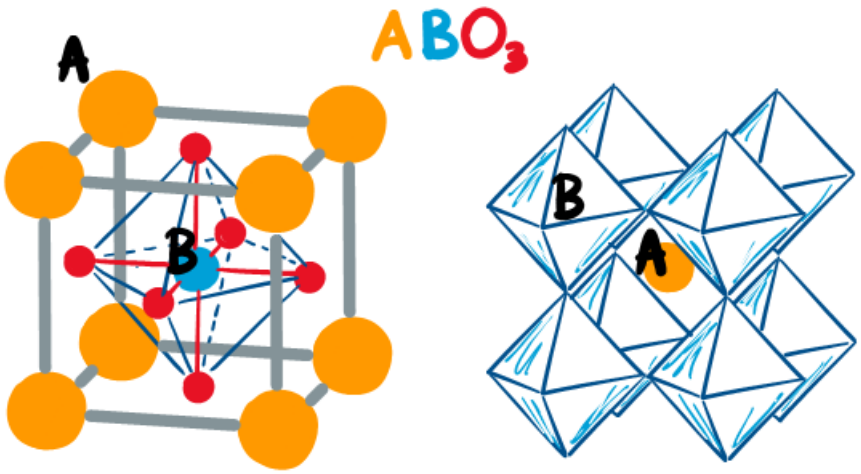

Figure 2-1. Perovskite structure with ABO_3 chemical formula.

elements needed to reproduce the unit cell, significantly deviating from the cubic structure. Coherently, the effect of high pressure forces an increase in the density of the crystalline phase, leading to more complex unit cells. This tendency to lower the crystal symmetry, while retaining the stoichiometry ABX_3, is allowed by the wide versatility and stability of the perovskite structure, confirmed by values of Goldschmidt tolerance factor t [4] which can significantly deviate from the ideal case t = 1; t is defined by the following equation:

$$t = (r_A + r_X)/\sqrt{2}(r_B + r_X) \quad (1)$$

where r_A, r_B, and r_X are the ionic radius of A, B and X species, respectively. Empirically, values of the tolerance factor $0.75 \leq t \leq 1.05$ are necessary to form perovskite structures, as will be discussed in Paragraph 2.2, but not a sufficient condition. Besides, another important geometrical parameter should be considered, i.e. the octahedral factor μ defined as the ratio between r_B and r_X. Based on the literature, reasonable values for μ which allow retaining the perovskite structure stability are between 0.4 and 0.8, where the strong constraint of $\sqrt{2}(r_B+r_X)<2r_X$, due to the octahedral coordination of B, is considered [5] [6] [7] [8] [9]. Consequently, the perovskite results to be highly adaptive to host different kinds of ions at specific sites, leading very often to BX_6 polyhedral distortions or tilting and the off-centre of B from the coordination positions in order to balance differences in the ionic sizes. As a consequence, perovskites usually display interesting physical properties which are usually related to such notable lowering of the structural symmetry, for

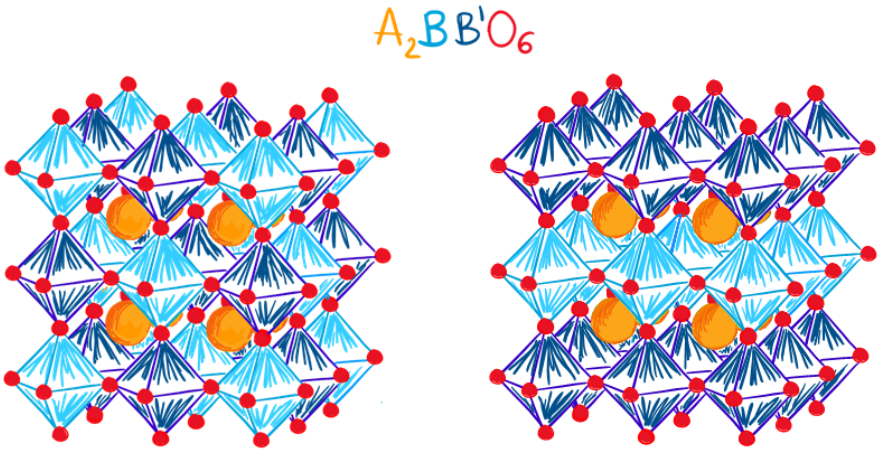

Figure 2-2 Perovskites with rock-salt (left) and layered (right) B-cation ordering.

instance, the superposition of multiple ferroic orders (i.e. multiferroism) [10] [11] [12], magnetoelectricity [13] [14] [15], spin-polarized carriers [16], magnetostriction [17], magnetoresistance [18], photocatalytic and photovoltaic effect [19] [20]. These effects can be exploited in an extensive range of applications as innovative magnetic memory systems, in the field of spintronic, as catalysts in fuel cells, in energy storage or as core materials in electronic devices and sensors and energy photoconversion and harvesting technology.

From these considerations, it comes out that the great potential of the perovskites can be extensively engineered by playing with the chemistry of their crystal structure. Specifically, by substituting different ions on the A and the B sites it is possible to tune and tailor exotic physical properties in a single crystalline phase. Taking into account geometrical and chemical constraints related to the A and B cations, like the atomic radius and the oxidation state, which are essential for the retention of structural stability, a widespread series of ionic combinations and partial substitutions on the two distinct sites can be investigated. Moreover, the type of cation introduced in these sites is pivotal and can induce a specific character itself, like magnetic or conductive tendency for ions with partially filled d shells, so high numbers of Bohr magnetons. Moreover, an important aspect is represented by the cationic ordering on the A or B site, as an additional symmetry-linked degree of freedom for modelling the physical properties. This condition pointed out two different configurations of ordering. Particularly, the two cations sitting at the A (or the B) site can have a relative periodic occupancy arrangement, like in the most

common rock-salt ordering or the layered pattern, where non-equivalent positions are then needed to describe the unit cell (Figure 2-2). Otherwise, random distribution can occur at the considered site, which is therefore characterized by the same occupancy probability respect with to the two species. In the first case, the system is referred to as a double perovskite, with chemical formula $A_2B'B''O_6$ considering B' and B'' cations ordered (or $A'A''B_2O_6$ by introducing two different cations at the A site), while in the random occupancy case the simple perovskite structure is retained, and the compound is a disordered perovskite with formula $AB'_{0.5}B''_{0.5}O_3$.

2.2 Chemistry of the A and the B site: stability conditions

As previously mentioned, a wide range of ions' combinations at the A and B sites can be found in the literature. In the vast majority of single or double perovskites, the A site is occupied by a large divalent or trivalent cation, although in some cases even alkali substitution is possible, like Na, K or Rb species [21] [22]. Specifically, in the A^{2+} case alkaline earth elements, like Ca, Sr, or Ba, are extensively studied [23] [24], but many works report on stable perovskites with Pb [25], Mn [26] or Cd [27] cations. On the other hand, A^{3+}-based perovskites prevalently contain La, Bi or rare earth elements [28] [29] [30]. The relatively larger size of A^{2+} cations respect with to the A^{3+} ones allows to access a greater range of valency state combinations for B' and B''. In fact, for divalent A cations the average oxidation state for the B site is four, thus a combination of elements with variable states from 1+ to 7+ is allowed, covering all the elements of the periodic table, while for trivalent A ones the mean value for B-valency state is three, with the consequent exclusion of oxidations states higher than 5+. In many cases, the B position is filled by 3d, 4d, and 5d transition metals, but in some cases also by lanthanides and actinides [31] [32] [33].

Considering the large variety of atomic species that can fit the perovskite structure, the difference in the cationic size has to be taken into account as a fundamental parameter. By a judicious choice, it is possible to vary the size of the ionic radius of the A or B site until about 65% or 70% respectively, i.e from the smallest radius of Al^{3+} (0.53 Å) on A or of Be^{2+} (0.45 Å) on B to the larger one of

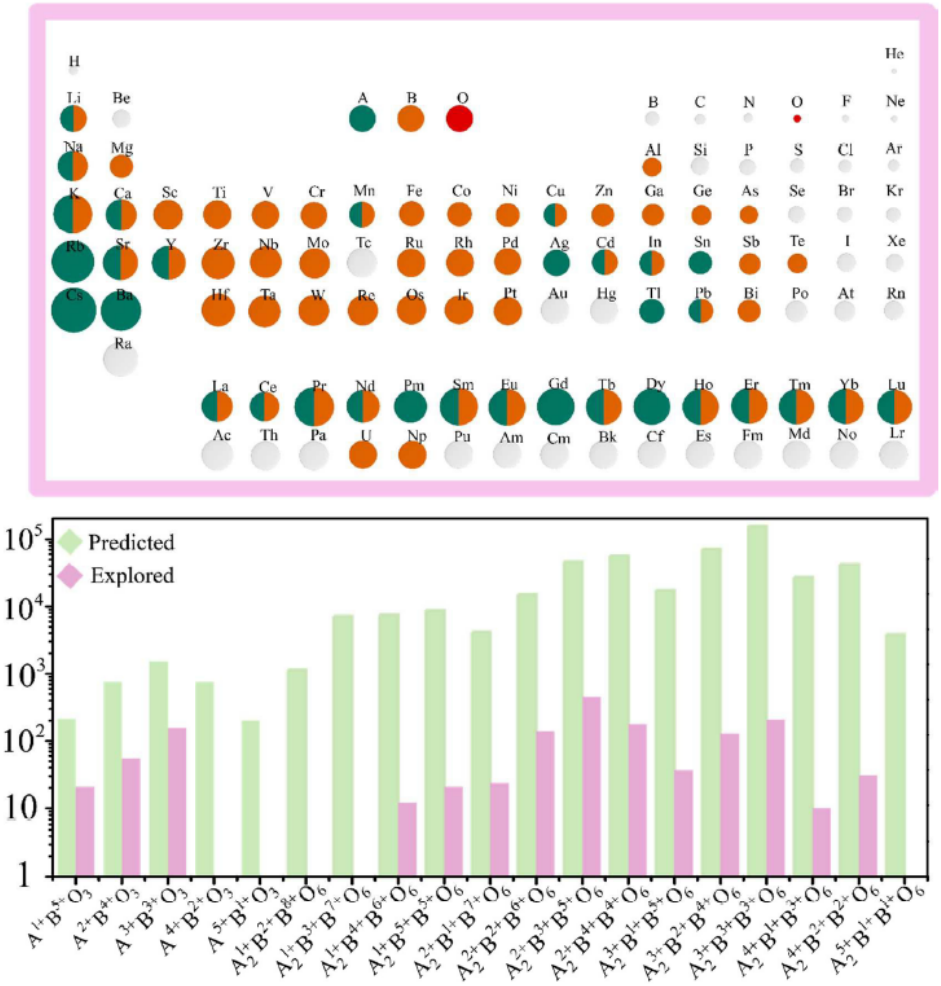

Figure 2-3 Possible A/B cations in perovskite structures (top) with predicted and explored possible combinations considering the valency states. [adapted from ref. [193]]

K^{1+} (1.52 Å) available on both the positions. As shown in the former paragraph, the dimension mismatch is described by the Goldschmidt factor, and some considerations on the changes vs. the ideal cubic structure can be pointed out. Particularly, for t values lower than 1, the radius of A cation is small and, to compensate for the discrepancy, the structure stabilizes itself with the BO_6 octahedra tilting, usually adopting a cubic ($0.9<t<1.0$) or orthorhombic ($0.8<t<0.9$) configuration. For lower t values, compounds usually lose the perovskite structure and turn into hexagonal ilmenite phases, like in the case of $FeTiO_3$ [34]. On the contrary, when *t* is higher than 1, the A cation is large and typically precludes the retention of the perovskite structure, with the tendency to revert into a hexagonal symmetry. However, the double perovskite $Ba_2Bi_{0.1}Sc_{0.2}Co_{1.7}O_{6-x}$ still displays a cubic structure with one of the greatest limiting values for *t*, equal to 1.084 [35]. For double perovskites, the ionic radii difference of B' or B'' cations seems to be quite large without strictly affecting the stability of the perovskite, as in Ba_2KIO_6

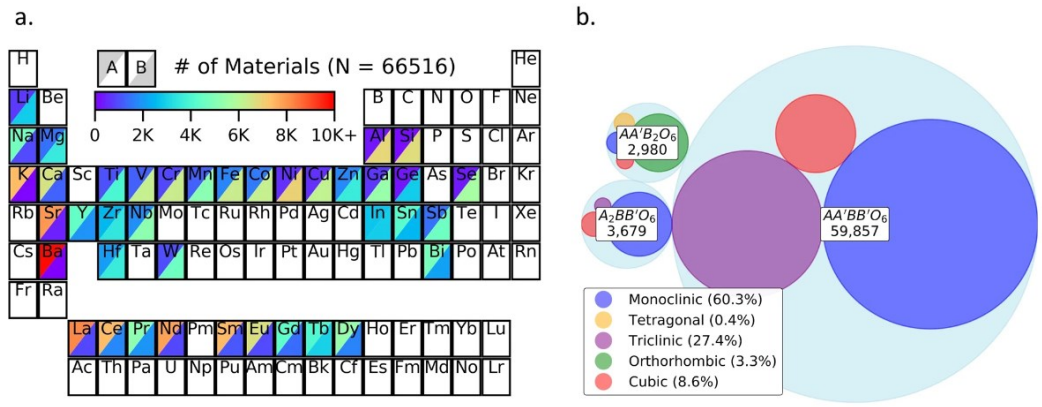

Figure 2-4 (a) Periodic table plot showing A and B sites frequencies of different cations, with (b) the predicted crystal symmetry abundance from DFT. [adapted from ref. [37]]

in which the Δr between potassium and iodine ions is about 0.85 Å (or 160%), so the main condition for stability is represented by the different radii between A and B cations [36]. Although this empirical parameter condition may not always be very precise, based on the literature, we can consider a tolerance factor criterion of $0.75 \leq t \leq 1.05$ as a reasonable range for perovskite structure stability. Considering the restrictions the valence of the cation states at the A and B sites and the previous range for tolerance factor values, an extremely high number of new in principle stable perovskites has been predicted. The results depicted in Figure 2-3 show all the possible cations which can be selected to form a single or a double perovskite, with the already explored compounds and those that are just theoretically predicted. Moreover, recent studies reported on the possibility to evaluate and to predict, by the application of density functional theory (DFT) and other specific codes the crystal structure of around 60000 unexplored double perovskite oxides, as reported in Figure 2-4 [37]. It comes out that most of the ideally stable double perovskites have not yet been synthesized pushing material scientists to develop novel compounds.

2.3 Lowering of crystal symmetry

From a geometrical point of view, in accordance with the tolerance factor formula, all the perovskite lattice parameters can be described starting from the single cubic perovskite depending on the B-site cation ordering [38]. In fact, in the ideal condition, the A-O bond length is $\sqrt{2}$ times the B-O bond length, with the cell parameter of the standard cubic structure ABO_3 around $a_p \approx 3.9$Å (space group Pm-

Serial number	Symbol	Lattice centring	Multiple cell	Relative pseudocubic subcell parameters	Space group
3-tilt systems					
(1)	$a^+b^+c^+$	I	$2a_p \times 2b_p \times 2c_p$	$a_p \neq b_p \neq c_p$	*Immm* (No. 71)
(2)	$a^+b^+b^+$	I		$a_p \neq b_p = c_p$	*Immm* (No. 71)
(3)	$a^+a^+a^+$	I		$a_p = b_p = c_p$	*Im*3 (No. 204)
(4)	$a^+b^+c^-$	P		$a_p \neq b_p \neq c_p$	*Pmmn* (No. 59)
(5)	$a^+a^+c^-$	P		$a_p = b_p \neq c_p$	*Pmmn* (No. 59)
(6)	$a^+b^+b^-$	P		$a_p \neq b_p = c_p$	*Pmmn* (No. 59)
(7)	$a^+a^+a^-$	P		$a_p = b_p = c_p$	*Pmmn* (No. 59)
(8)	$a^+b^-c^-$	A		$a_p \neq b_p \neq c_p \alpha \neq 90°$	$A2_1/m11$ (No. 11)
(9)	$a^+a^-c^-$	A		$a_p = b_p \neq c_p \alpha \neq 90°$	$A2_1/m11$ (No. 11)
(10)	$a^+b^-b^-$	A		$a_p \neq b_p = c_p \alpha \neq 90°$	*Pnma* (No. 62)*
(11)	$a^+a^-a^-$	A		$a_p = b_p = c_p \alpha \neq 90°$	*Pnma* (No. 62)*
(12)	$a^-b^-c^-$	F		$a_p \neq b_p \neq c_p \alpha \neq \beta \neq \gamma \neq 90°$	$F\bar{1}$ (No. 2)
(13)	$a^-b^-b^-$	F		$a_p \neq b_p = c_p \alpha \neq \beta \neq \gamma \neq 90°$	*I*2/*a* (No. 15)*
(14)	$a^-a^-a^-$	F		$a_p = b_p = c_p \alpha = \beta = \gamma \neq 90°$	$R\bar{3}c$ (No. 167)
2-tilt systems					
(15)	$a^0b^+c^+$	I	$2a_p \times 2b_p \times 2c_p$	$a_p < b_p \neq c_p$	*Immm* (No. 71)
(16)	$a^0b^+b^+$	I		$a_p < b_p = c_p$	*I*4/*m* (No. 78)
(17)	$a^0b^+c^-$	B		$a_p < b_p \neq c_p$	*Bmmb* (No. 63)
(18)	$a^0b^+b^-$	B		$a_p < b_p = c_p$	*Bmmb* (No. 63)
(19)	$a^0b^-c^-$	F		$a_p < b_p \neq c_p \alpha \neq 90°$	*F*2/*m*11 (No. 12)
(20)	$a^0b^-b^-$	F		$a_p < b_p = c_p \alpha \neq 90°$	*Imcm* (No. 74)*
1-tilt systems					
(21)	$a^0a^0c^+$	C	$2a_p \times 2b_p \times c_p$	$a_p = b_p < c_p$	*C*4/*mmb* (No. 127)
(22)	$a^0a^0c^-$	F	$2a_p \times 2b_p \times 2c_p$	$a_p = b_p < c_p$	*F*4/*mmc* (No. 140)
Zero-tilt system					
(23)	$a^0a^0a^0$	P	$a_p \times b_p \times c_p$	$a_p = b_p = c_p$	*Pm*3*m* (No. 221)

* These space group symbols refer to axes chosen according to the matrix transformation

$$\begin{pmatrix} 1 & 0 & 0 \\ 0 & \frac{1}{2} & -\frac{1}{2} \\ 0 & \frac{1}{2} & \frac{1}{2} \end{pmatrix}.$$

Table 2-1 List of possible tilting by Glazer notation. [adapted from ref. [43]]

3m). If a rock-salt ordered sublattice is present, a doubling of the lattice parameter $2a_p$ is needed to describe the unit cell, with face-centred space group symmetry Fm-3m [39] [40] [41]. Instead, it has been shown that many perovskites with random-B cation distribution crystallize in an orthorhombic unit cell with lattice parameters close to a=b≈$\sqrt{2}a_p$ c=$2a_p$ and Pbnm symmetry [42] [43] [44], while in the rock-salt ordered case the as-obtained perovskite is preferentially monoclinic $P2_1/n$ [45] [46] [47], whose stabilization is linked to small BO_6 polyhedra distortions. In fact, as an additional degree of freedom, the perovskite can distort due to competing cationic bonding of A, B', and B'' species, leading to a displacement of cations [48], or the distortion [49] or, commonly, the tilting of octahedra [50]. It is usually difficult to discriminate octahedral modifications in order to solve the crystalline structure of a new perovskite because the main role is played by oxygen positions, which can generate superstructure features not easily detectable without for instance neutrons sources. However, based on chemical considerations of the involved cations, some analogies can be stated also for the type of displacements/distortion. One example is represented by disordered perovskites with a small A cation, where the BO_6 tilt occurs to optimize the bond with A [51] [52]. These tilting phenomena can be described and identified by the Glazer notation [53], which links the octahedral

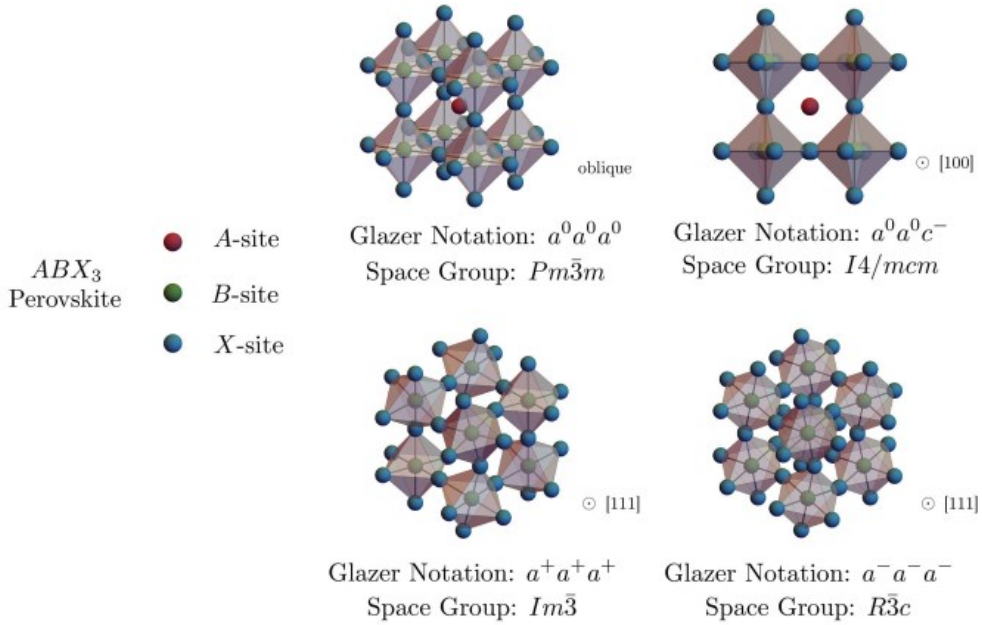

Figure 2-5 Examples of distorted perovskites with corresponding Glazer notation and space group. [adapted from ref. [96]]

changes with space group representations. Such an elegant notation is used to describe the rotation of the oxygens octahedra around the [100], [010], and [001] axes, with possible in-phase (+) or anti-phase (-) tilting. The whole list of possible tilted systems is reported in Table 2-1, and some examples of ABX_3 perovskite distorted lattices are shown in Figure 2-5. In real cases, it is difficult to predict the type of distortion which can occur, but, as for the crystallographic lattice, some correlations with the tolerance factor values can be found in the literature. Moreover, because of its non-completely ionic nature, the existing bonds of the perovskite cell also display a covalent character that should be considered. Specifically, observations reported in the literature highlights that highly charged A cation with small octahedral tilting is to stabilize primary a rhombohedral structure, because of its high electronegative tendency [54] [55]. On the contrary, regarding the covalent nature of the B cation, a switching to tetragonal and orthorhombic structures is more common.

2.3.1 Physical and electrical origin of distortion mechanisms

Lattice distortions and relative lowering of the crystal symmetry in perovskites are strongly associated with intriguing physical properties in such

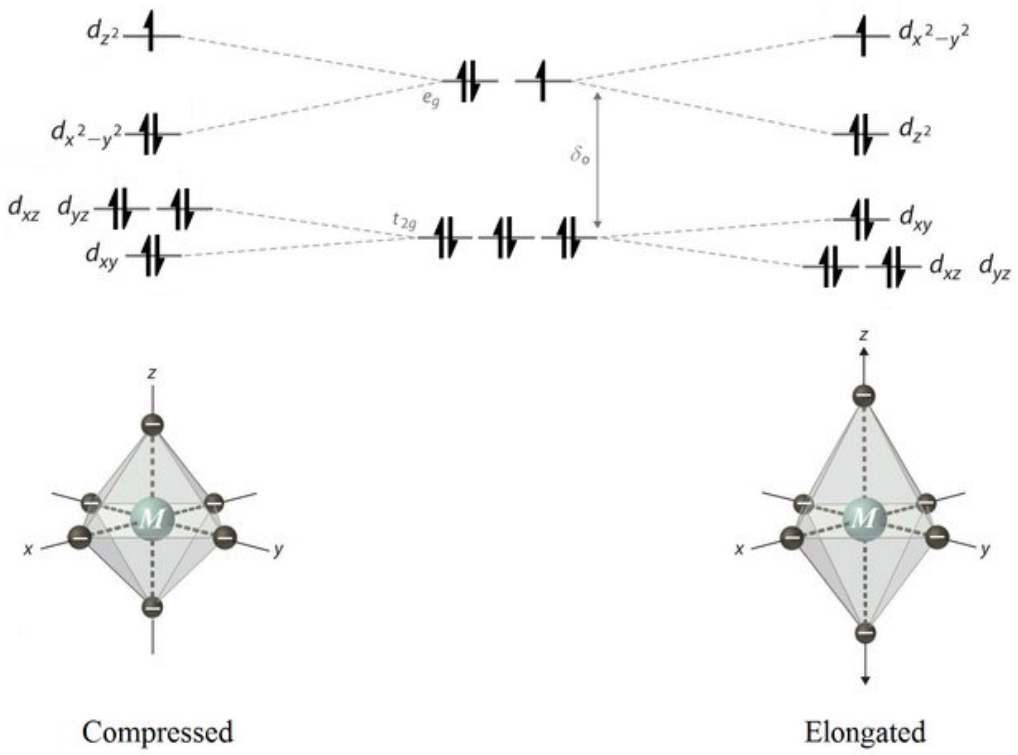

Figure 2-6 Jahn-Teller effect of Cu^{2+} in octahedral coordination. When the unpaired electron resides in the dz2 orbital (left), the octahedra is compressed along the z direction. Alternatively, an unpaired electron in the dx2□y2 orbital (right) elongates the octahedra. [adapted from ref. [194]]

compounds. These distortions and structural modifications are in turn caused by physical and electronic mechanisms inside the crystal lattice that can vary by selecting specific kinds of cations.

One important example is the *Jahn-Teller (JT) distortion* [56], a mechanism of spontaneous symmetry breaking which originates from the electric configuration of the cations. Particularly, this effect is common in octahedral complexes of transition metals, like for instance Mn^{3+} (d^4 high spin), Co^{2+} (d^7 low spin) or, even more significantly, for Cu^{2+} (d^9) ions, in which a degenerated electronic ground state undergoes a geometrical distortion in order to remove the degeneracy, thus providing an energetic stabilization [57]. In perovskites, the B-site cation, with its intrinsic octahedral coordination, can be a JT active center, resulting in a cooperative phenomenon of global crystal distortions due to local degeneracies. Specifically, in octahedral coordination, the d-shell ground state degeneration of a transition metal leads to an energy splitting with the consequent formation of three t_{2g} low energy orbitals and two e_g orbitals with a higher energy of δ_0 due to the crystal field acting on the cation. In the prominent case of Cu^{2+} species, thanks to

its relatively strong electronegativity and more covalent bonding, the t_{2g} shell is completely filled by six electrons, while the remaining three occupy the e_g shell, as shown in Figure 2-6. The unpaired electron of the latter shell can occupy any of e_g orbitals, specifically the dz^2 or the dx^2-y^2 level. If the first orbital is occupied, the high energy electron and the oxygens in the octahedral configuration repulse each other, causing an elongation of the polyhedral along the apical z direction. On the contrary, the occupancy of the dx^2-y^2 orbital leads to an attractive interaction that ends with a compression of the octahedra with a consequential stretch along the basal plane. For instance, cuprate double perovskites $A_2CuB''O_6$ with A=Ba, Sr and B''=W, Te display tetragonal structure with elongation of CuO_6 octahedra along the c-axis due to the JT effect of Cu^{2+} ions [58]. In these compounds, due to the presence of such the elongated octahedra, superexchange interactions between copper via non-magnetic ions occur predominantly in the ab plane, resulting in a two-dimensional antiferromagnetic behaviour. This anisotropy in magnetic interactions is reported also with the presence of JT active Mn^{3+} cations, as in the family $RMnO_3$ (with R=rare earth) [59] or $Dy(FeMn)O_3$ solid-solution [60]. Therefore, the cooperative JT effect in such compounds induces a strong coupling between orbital, charge and magnetic ordering, which in some systems leads to exotic properties like the colossal magnetoresistance displayed for example by the extensively studied $LaMnO_3$ [61], in which cooperative JT distortions are present in both the compressed and elongated geometry [62].

In many perovskites a reduction of the crystal symmetry has been observed related to the presence of stereochemically-active cations with *lone-pair* electrons, like Pb^{2+} or Bi^{3+} ions, at the A site. Namely, the $6s^2$ electronic shell of this species tends to hybridize with the oxygen 2p orbitals due to a comparable energy of the two orbitals. As a consequence, the stereochemically-active cation is shifted from the ideal position with respect to the surrounding nearest neighbour oxygens giving rise to high directional bonds and electronic cloud polarization. From the structural point of view, this mechanism can cause and stabilize tilts and distortions of the octahedra which often determine non-centrosymmetric crystallographic structures, as displayed in many famous perovskites like the multiferroic $BiFeO_3$ [63], whose electron localization is shown in Figure 2-7, $BiMnO_3$ [64], $PbTiO_3$ [65], $BiFe_{0.5}Mn_{0.5}O_3$ [66], or the quadruple perovskite $BiCu_3Cr_4O_{12}$, in which the Bi

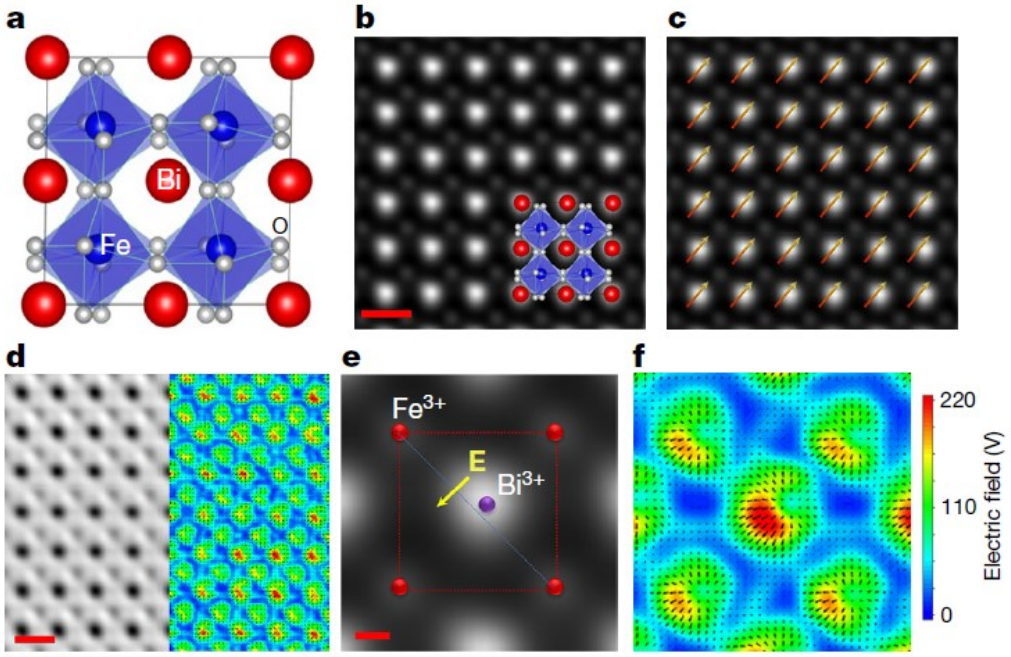

Figure 2-7 $BiFeO_3$ structure (a) with HAADF-STEM image (b) and dipole moment polarization (c). Electric map with the localizazion of lone-pair electrons (d, e, f). [adapted from ref. [195]]

lone-pair effect generates a charge disproportion of $Cr^{4+}/Cr^{3.5+}$ and an asymmetric distortion of BiO_{12} polyhedra [67]. The polarizability of lone-pair electrons has been demonstrated to produce a net electric dipole and thus a ferroelectric behaviour in some of the previously cited perovskites.

In analogy with the case described above, a decrease of crystal symmetry is observed in many perovskites to occur due to mechanisms involving the B-site cation. Particularly, the insertion in this site of a d^0 transition metal, like Ti^{4+}, Zr^{4+}, or Nb^{5+}, can lead to a partial hybridization of its d orbital with the 2p ones of oxygens of the octahedral cage. Consequently, the *off-centering of the B cation* respect with the high symmetric position occurs. The most significant example is reported for $BaTiO_3$, which displays a lowering of crystal symmetry from cubic centrosymmetric to tetragonal polar structure due to Ti^{4+} off-centering of about 0.1 Å (see Figure 2-8), favouring the appearance of a non-zero electric dipole moment so ferroelectric state [68].

Another example of crystallographic symmetry reduction is displayed in *geometrically frustrated l*attices, like the Kagome patterns, in which atoms tend to fit non-regular crystallographic sites, generally as a consequence of large differences in the size of cations. To this class belong the hexagonal perovskites

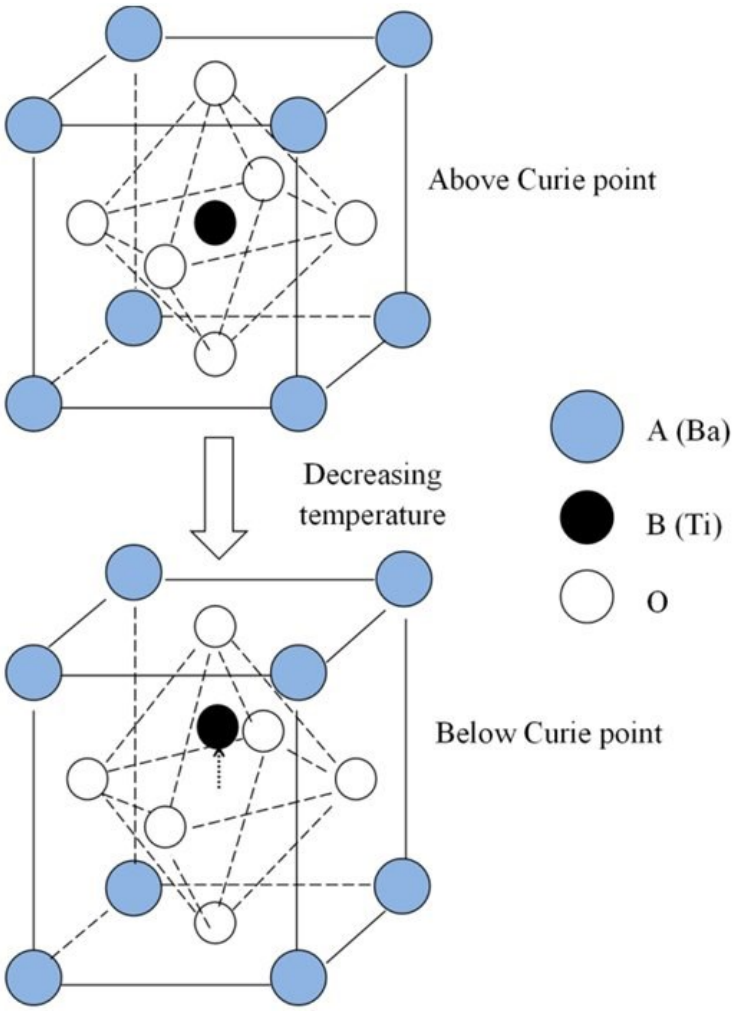

Figure 2-8 $BaTiO_3$ cubic perovskite structure with Ti off-centering across the structural/ferroelectric transition. [adapted from ref. [196]]

with chemical formula $RMnO_3$ (R = Rear Earth or Y), where the low dimension of the R ion leads to significant deviations from the cubic structure till possible ferroelectric distortion. Additionally, the geometrically frustrated systems are usually characterized by complex spin arrangements, with consequent geometrical magnetic frustration of non-collinear spins.

2.4 Electrical properties of perovskites

The considerations reported so far underline the possibility of predicting the lattice and symmetry features in a perovskite in relation to the selected cationic species on the different sites, with special emphasis on the cationic ordering aspects. Moreover, as reported so far, the crystalline structure strongly affects the physical properties, and it is essential to correlate how to tune the observed micro- and

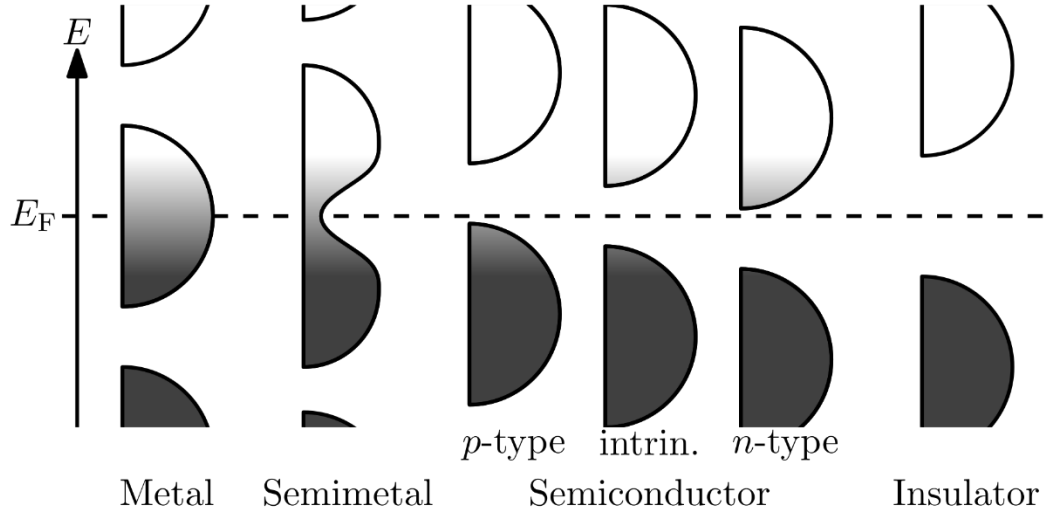

Figure 2-9 Band width of different materials and Fermi level E_F at the thermodynamic equilibrium following the Fermi-Dirac distribution of occupancy probability (black colour for fully occupied states, while white for empty energy levels). [adapted from ref [197]]

macroscopic properties of the perovskites by playing with the chemistry of the A and B sites. As described before, the versatility and adaptability of this structure allow it to accommodate cations with several intrinsic tendencies, thus it is possible to obtain a wide variety of physical properties, particularly regarding electric behaviour and magnetism, and eventually combine them in unusual ways.

Starting from the electrical point of view, as in perovskite systems it is possible to face different kinds of electrical transport mechanisms and intrinsic characters, I want to discuss some basic theoretical aspects related to dielectrics, semiconductors, and metals formulations that will be useful to better follow the analyses reported in the next experimental chapters.

Considering the band theory of solids, fundamental treatment in order to describe the energy levels occupied by the electrons in solid materials, it is possible to discriminate different electrical behaviours taking into account the Fermi level [69]. This thermodynamic quantity, E_F, is defined as the highest energy level occupied by an electron at 0 K, and its value enters the equation of the definition of the distribution function which describes the probability for an electron to occupy a particular energy level ε at the temperature T, following the Fermi-Dirac equation:

$$f(\varepsilon) = \frac{1}{e^{(\varepsilon - E_F)/k_B T} + 1} \quad (2)$$

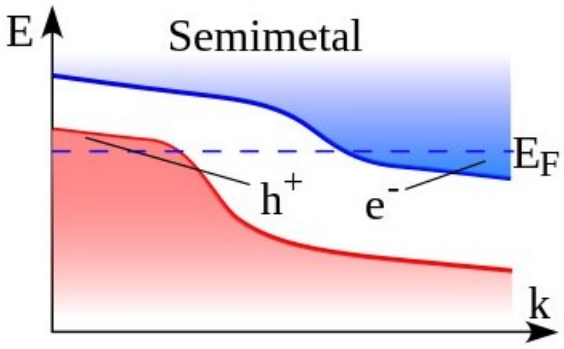

Figure 2-10 Representation of valence (red) and conduction (blue) bands in semimetal compounds. [adapted from ref. [198]]

where k_B is the Boltzmann constant. The relative position of E_F with respect to the possible energy levels for the electrons determines the material's electrical character (Figure 2-9). Namely, for insulators the E_F falls into a large band energy gap between the conduction and the valence band of the electrons (e.g. higher than 4 eV), in a range far from any possible occupied levels. On the contrary, in semiconductor materials, E_F is nearer to the conduction or valence bands, which are energetically spaced less than 4 eV, so it is probable for an electron (or hole, depending on the carrier type) to overcome this smaller energy gap with a thermal excitation or through solar photon absorption. On the other hand, in metallic materials the E_F level crosses the continuum of possible states formed to the partial overlap between the bands and a considerable number of electrons can be involved in the electrical conduction. Perovskite metal oxides can be employed in energy conversion and storage, sensing and spintronics [70]. Another class of materials can be defined between semiconductors and metals, the so-called semimetals. In such compounds, there is no band gap (as in metals) but the valence and conduction bands do not cross the Fermi level at the same momentum space k, defined from the Bloch theory and Brillouin zone description of crystals [71]. Moreover, both electrons and holes can contribute to electronic transport, like in semiconductors, as highlighted in Figure 2-10.

As in the experimental part of my Thesis, I have focussed the attention on dielectric and semiconductive perovskites, in which, in general, more than one functionality can be found (multifunctional perovskites), I will expand the theoretical discussion only for these two classes of electric behaviour.

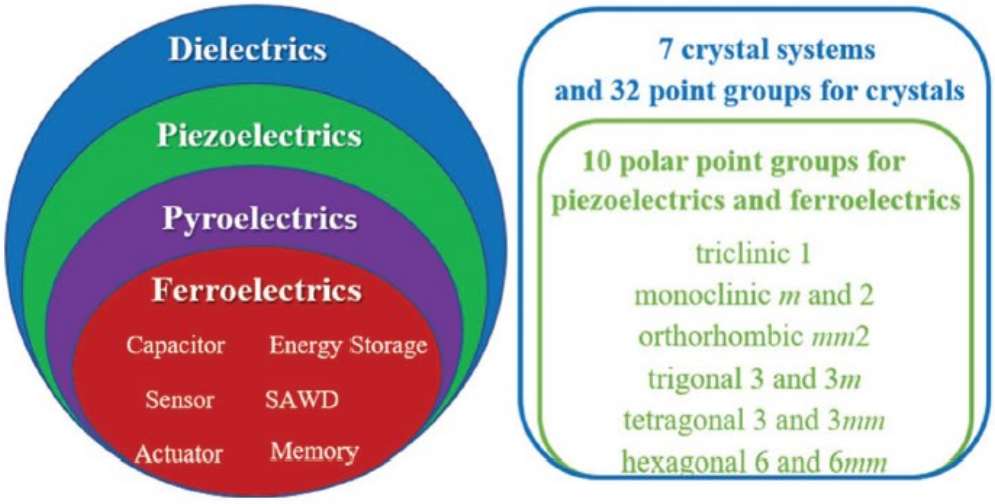

Figure 2-11 Classes of dielectric, piezoelectric, pyroelectric, and ferroelectric materials (left) with the related crystal systems and point groups that allowed these properties. [adapted from ref. [199]]

2.4.1 Dielectrics

Dielectric perovskites represent a large class of functional materials, whose peculiar behaviour usually originates from the lowering of crystallographic symmetry, as described in the previous subchapters. A dielectric material is defined as an electrical insulator in which due to the application of an external electric field no/negligible flow of current is detected but electrical polarization is induced with a sign opposite to the applied electric field $\vec{E}$. This static charge separation is defined by the so-called displacement vector $\vec{D}$:

$$\vec{D} = \varepsilon_0 \varepsilon_r \vec{E} \tag{3}$$

where ε_0 is the vacuum permittivity and ε_r is the relative static permittivity.

The removal of the external field for simple dielectrics causes the collapse of this electrical charge separation and the re-neutralization of the material. Dielectrics are divided into two main categories: apolar and polar dielectrics. Polar dielectrics, i.e. piezoelectrics (see Figure 2-11), are characterized by the lack of symmetry space inversion center. Among the 32 possible point groups, the non-centrosymmetric ones are only 21. In piezoelectrics, the internal electrical polarization occurs and thus a voltage is generated by the material when it is subjected to a proper mechanical stress, as a compression, along the polar axis (direct piezoelectric effect) and, vice versa, mechanical energy is produced when

Materials	Properties	Applications
$BaTiO_3$	dielectric	capacitor, sensor
$(Ba,Sr)TiO_3$	pyroelectric	pyrodetector
$PbTiO_3$	pyroelectric piezoelectric	pyrodetector acoustic transducer
$Pb(Zr,Ti)O_3$	dielectric pyroelectric piezoelectric electro-optic	nonvolatile memory, pyrodetector surface acoustic wave device, substrate waveguide device
$(Pb,La)(Zr,Ti)O_3$	pyroelectric electro-optic	pyrodetector waveguide device, optical memory display
$LiNbO_3$	piezoelectric	pyrodetector, surface acoustic wave device
$(LiNbO_3/Ti)$	electro-optic	waveguide device, second harmonic generation, optical modulator
$K(Ta,Nb)O_3$	pyroelectric electro-optic	pyrodetector waveguide device, frequency doubler
$Pb(Mg_{1/3}Nb_{2/3})O_3$	dielectric	memory, capacitor

Table 2-2 Examples of dielectric perovskite oxides. [adapted from ref. [200]]

the system undergoes and external bias application (indirect piezoelectric effect). Within the piezoelectric family material, a small subset of materials possesses 10 non-centrosymmetric point groups from 21 which allow the presence of spontaneous electric polarization even without an external stimulus. These are the pyroelectric materials. In these materials electrical polarization can be permanently developed or suppressed by a specific cooling or heating thermal process, crossing the Curie Temperature of the electrical ordered phase. A sub-group of pyroelectrics, called ferroelectrics, gathers those polar materials in which electrical polarization can be switched by an external electric field, describing the so-called ferroelectric loop, analogously to ferro/ferrimagnets. Often, perovskites host dielectric properties. Indeed, insulator character is common in single or double perovskites, for example when d0 transition metals, like Ti^{4+} or Zr^{4+} are located at the B site. Even though there are many dielectric $A_2B'B''O_6$ perovskites, with A = Ca, Sr, Ba, and B' or B'' = La, Nd, Sm, Yb, Nb, Ta, it's more difficult to observe high-temperature electronic properties. Small co-substitutions at the B sites can increase the working temperature, as demonstrated in $Bi_{0.5}Na_{0.5}TiO_3$-based ceramic [72]. B-ordering seems to favour the applicability of such systems by reducing the dielectric losses. As previously described in Paragraph 2.3, the ferroelectric behaviour can be induced by introducing a stereochemically-active cation at the A site, as Pb^{2+} or Bi^{3+} ions, where the $6s^2$ lone pair electrons allow ferroelectric distortions in the perovskite structure, as described in the previous paragraph. One extensively

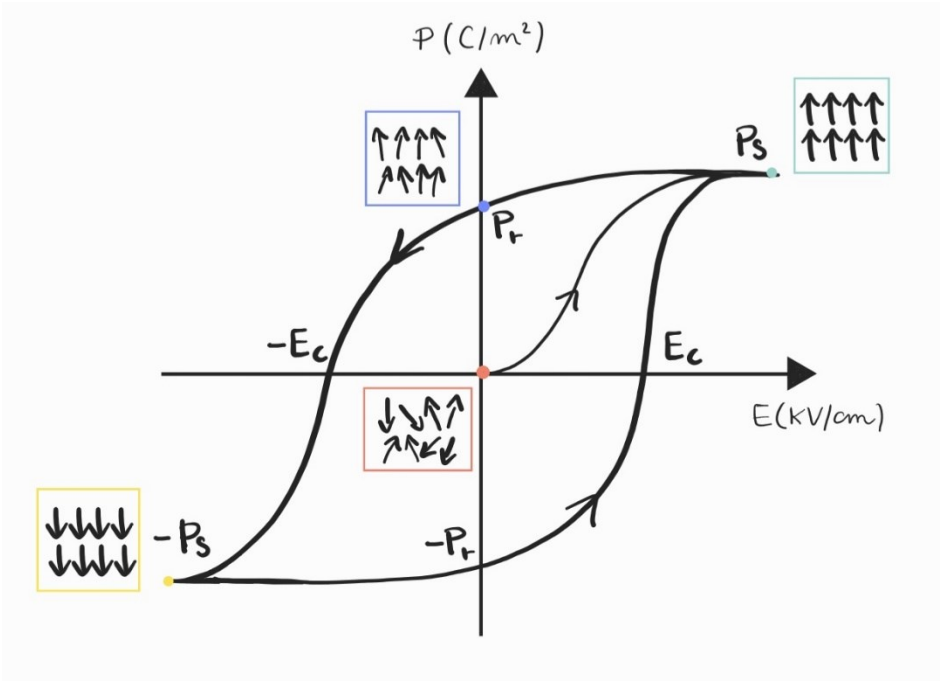

Figure 2-12 Hysteresis loop of ferroelectric materials. [adapted from ref. [206]]

studied example is represented by $Pb(Zr_xTi_{1-x})O_3$ perovskite family, in which the cationic order at the B site usually leads to ferro- or antiferroelectric structures A list of dielectric perovskites is reported in Table 2-2, specifying which kind of character they possess.

2.4.2 Semiconductors

Even though insulating character is the expected behaviour of oxide perovskites, many artificial perovskites display semiconductive behaviour due to a narrowing of the optical band gap, and some examples of such compounds are listed in Table 2-3, highlighting their applications. The majority of semiconductive perovskites with a band gap compatible with the visible range are employed as photovoltaics (PV), or optoelectronics and/or as catalysts or cathodes in photo-electrochemistry (PEC) for oxygen reduction (ORR) or evolution reactions (OER) [73] [74] [75] [76] [77]. In the following, I am going to focus my attention only on the description of the main models of electrical transport which can be employed for disordered or complex perovskites, without considering any optical or photochemical properties.

It is known that ideal semiconductors are characterized by a transport mechanism which follows the thermally activated model, in which the electrical

Alloy compounds	Tolerance factor	Applications
$(Sm_{0.5}Ba_{0.5})CoO_3$	1.031	OER
$(Gd_{0.5}Ba_{0.5})CoO_3$	1.029	OER
$(Ho_{0.5}Ba_{0.5})CoO_3$	1.020	OER
$La_{0.58}Sr_{0.4}Co_{0.4}Fe_{0.6}O_3$	1.002	ORR and OER
$La_{0.38}Sr_{0.6}Co_{0.2}Fe_{0.8}O_3$	1.003	ORR and OER
$La_{0.58}Sr_{0.4}Co_{0.6}Fe_{0.4}O_3$	1.007	ORR and OER
$La_{0.58}Sr_{0.4}Co_{0.8}Fe_{0.2}O_3$	1.013	ORR and OER
$La_{0.58}Sr_{0.4}Co_{0.2}Fe_{0.8}O_3$	0.996	ORR and OER
$Ca_{0.6}La_{0.4}Al_{0.4}Mn_{0.6}O_3$	1.006	ORR
$Ca_{0.7}La_{0.3}Al_{0.3}Mn_{0.7}O_3$	1.005	ORR
$Ca_{0.8}La_{0.2}Al_{0.2}Mn_{0.8}O_3$	1.005	ORR
$Ca_{0.9}La_{0.1}Al_{0.1}Mn_{0.9}O_3$	1.005	ORR
$LaNi_{0.25}Co_{0.75}O_3$	1.002	OER
$La_{0.8}Sr_{0.2}Mn_{0.6}Ni_{0.4}O_3$	1.002	OER
$La_{0.6}Sr_{0.4}Mn_{0.2}Ni_{0.8}O_3$	1.021	ORR and OER
$Ca_{0.9}Yb_{0.1}MnO_3$	0.997	OER
$La_{0.4}Sr_{0.6}CoO_3$	1.026	OER
$NdBa_{0.25}Sr_{0.75}Co_2O_{5+6}$	1.018	ORR
$Ca_2Mn_2O_5$	1.004	OER
$Ba_{0.9}Co_{0.5}Fe_{0.4}Nb_{0.1}O_3$	1.082	ORR and OER
$La_{0.8}Sr_{0.2}MnO_3$	0.997	ORR
$LaNi_{0.8}Fe_{0.2}O_3$	0.992	ORR and OER
$PrBa_{0.25}Sr_{0.75}Co_2O_{5.95}$	1.020	ORR and OER
$La(Co_{0.55}Mn_{0.45})_{0.99}O_3$	0.995	ORR and OER
$La_xSr_{1-x}Fe_yCo_{1-y}O_3$ (x = 0.8, 0.6, 0.4 and 0.2; y = 0.1, 0.2, 0.4, 0.6 and 0.8)	0.992 – 1.027	OER
$Pb(Zr,Ti)O_3$	0.991	PV
$(Pb,La)TiO_3$	0.996	PV
$(Pb,La)(Zr,Ti)O_3$	0.970	PV
$SrCo_{0.9}Ti_{0.1}O_3$	1.037	OER
$PrBa_{0.5}Sr_{0.5}Co_{1.5}Fe_{0.5}O_5$	1.020	OER
$LaNi_{0.85}Mg_{0.15}O_3$	0.986	ORR and OER
$LaTi_{0.65}Fe_{0.35}O_{3-\delta}$	0.955	ORR and OER
$Ba_2Bi_{1.4}Nb_{0.6}O_6$	0.942	OER and HER
Ba_2BiBiO_6	0.928	HER
Bi_2FeCrO_6	0.948	PV and HER
$CaCu_3Fe_4O_{12}$	0.875	OER
$CaCu_3Ti_4O_{12}$	0.866	Non PEC PC
$Ba_2Bi_{0.1}Sc_{0.2}Co_{1.7}O_6$	1.084	OER
$[KNbO_3]_{1-x}[BaNi_{0.5}Nb_{0.5}O_{3-\delta}]_x$	1.055 (x=0.1)	PV

Table 2-3 List of some semiconductive perovskites with their tolerance factors and the major applications. [adapted from ref. [193]]

conductivity of the charge carriers is triggered as a function of a particular activation energy E_A. Specifically, the resistivity ρ of this type of semiconductor is described with the temperature-dependent exponential Arrhenius law of the following equation:

$$\rho(T) = \rho_0 \cdot exp\left(\frac{E_A}{k_B T}\right) \quad (4)$$

where ρ_0 is the value of resistivity at infinite temperature. In literature many examples of thermally-activated electrical transport in perovskites, can be found for instance in $LaSrMnCoO_6$ [78], Ba_2ErNbO_6 [79], or $Sr(La,Ce)Co(Fe)O_{3-x}$ family [80].

A different common electronic transport mechanism which can be observed in perovskites is the one described by the Adiabatic nearest Neighbour Hopping of Small Polarons (ANHSP), in which the resistivity is modelled in the following equation:

$$\rho(T) = \rho_0 T \cdot exp\left(\frac{E_{HOP}}{k_B T}\right) \quad (5)$$

where $\rho_0 = 2k/(3ne^2a^2\nu)$ represents the effective resistivity, depending on the density of the carriers n, on the electronic charge e, on the hopping spatial distance a, and on the longitudinal optical phonon frequency v. Here, in the temperature-exponential dependency of the resistivity enters the parameter E_{HOP} as the hopping threshold energy, that allowed to start of the electronic transport. The conductivity is in this way caused by the carriers' hopping, driven by small polarons, resulting from the interaction between the charge carriers with the inhomogeneities that are present and localized in such polycrystalline materials [81]. $Ln_{0.85}Ca_{0.15}MnO_3$ (Ln=Nd, Pr and Sm) [82], $La_{1-x}Ca_xMnO_3$ [81], or $LaCoO_3$ [83] are some perovskites that belong to this category of electronic transport mechanism.

Moreover, particularly for disordered-B perovskites or when oxygen vacancies occur, the hopping electronic transport is observed along a preferential direction, or more than one, as predicted in Mott's 1D, 2D, or 3D variable-range hopping (VRH) model for the electrical resistivity:

$$\rho(T) \approx \rho_0 \cdot exp\left(\frac{T_0}{T}\right)^{1/(D+1)} \quad (6)$$

where T_0 is the characteristic temperature, while the D parameter specifies the dimensional degree of conductance, and it can assume values equal to 1, 2, or 3 if the transport is along one, two or three directions.

A_2MnReO_6 with A= Ca, Sr, or Ba [84], Sr_2MnRuO_6 [85], or Pr_2CrMnO_6 [86] are only a few examples of double perovskites in which VRH mechanisms of the electronic transport have been observed.

2.5 Magnetic properties of perovskites

Perovskites constitute an even richer playground from the magnetic point of view. Indeed, in these systems a large variety of different and sometimes very complex behaviour can be found. As said before, magnetism in perovskites is brought by introducing magnetic ions both at the A and B sites. The presence of unpaired electrons on the valence shell leads to localized magnetic dipole moments that can interact with each other in a cooperative or competitive way. Due to the oxygen presence as a non-magnetic anion, super-exchange interaction usually is the main order mechanism taking place in such structures. For only one paramagnetic cation inserted at the B site, like in Ba_2CoWO_6, there are two possible configurations of the super-exchange interaction: the 90° nearest-neighbour interaction and/or 180° next-nearest neighbour interaction. The resultant of these interactions strongly varies with the system considered, with the type of ion, and with its structure and crystal field. By the insertion at B' and B'' of two different paramagnetic cations, B'-O-B'' and B'-O-B''-O-B' interactions usually occur whether no cationic order in the octahedral is established. Generally, the former type is stronger, but it depends also on the degree of B ordering. In these systems, collinear spin lattices can be found, showing antiferromagnetic (AFM) [87], ferromagnetic (FM) [88] or ferrimagnetic (FiM) [89] ordering and several works reported in literature highlight the possibility of tuning the ordering temperature (Curie temperature T_C in FM or Néel temperature T_N in AFM or FiM) of these magnetic perovskites by cations substitution at the B sites.

From a fundamental theoretical study by Goodenough-Kanamori-Anderson (GKA) [90] [91] [92], the type of interactions that take place in magnetic compounds can be predicted by considering the symmetry of electronic orbitals. Specifically, from the cation-anion orbital overlap and its symmetry, additionally to the mutual geometrical arrangement of the two species, i.e. the octahedral coordination in perovskites, it is possible to determine the sign of the exchange integral J of the (partially) occupied orbitals, from the Heisenberg-Dirac-van Vleck operator [93]:

$$\widehat{H}_{HDV} = -J\,\widehat{S_1} \cdot \widehat{S_2} \tag{7}$$

By evaluating these features, GKA rules state that the interaction arising between two spins S_1 S_2 of the two paramagnetic B'/B'' cations, mediated by virtual electron transfer processes via oxygen is linked to the electronic occupancy of the external atomic shells. Namely, an antiferromagnetic (AFM) interaction is predicted to take place whether both considered species have half-filled orbitals (i.e., negative values of J). On the contrary, positive J values and a ferromagnetic (FM) interaction appear when the exchange is from a half-filled orbital to an empty orbital, or from a full orbital to a half-filled one. For interactions that arise in the exchange from a fully occupied orbital to an empty one, the sign of J cannot be determined in advance [94]. Examples of super-exchange interactions with AFM coupling can be found in the case of Mn^{4+}-O-Mn^{4+}, Cr^{3+}-O-Cr^{3+}, Ni^{2+}-O-Ni^{2+}, Fe^{3+}-O-Fe^{3+} interactions, while for the interacting species Fe^{3+}-O-Cr^{3+}, Ni^{2+}-O-V^{2+} a FM behaviour have been experimentally reported [95] [96] [97]. In the case of a 90° interaction between cations in octahedral sites, different type of magnetism can be observed and predicted, following GKA theory, by considering the number of 3d electrons of the interacting cations involved. For instance, Ni^{2+} (d^8) interacting cations, as Cr^{3+} (d^3) ones, results in FM super-exchange mechanism, while Ni^{2+} (d^8) -V^{2+} (d^3) leads to AFM interaction. [91]

Although GKA rules can be very helpful in understanding what kind of interactions can result by mixing different cations, from an experimental point of view, in real systems, its application is usually not so effective, as for the case of tolerance factor analysis discussed in Paragraph 2.2. In fact, the flexibility of the perovskite structure allows it to bear significant structural distortions of oxygen

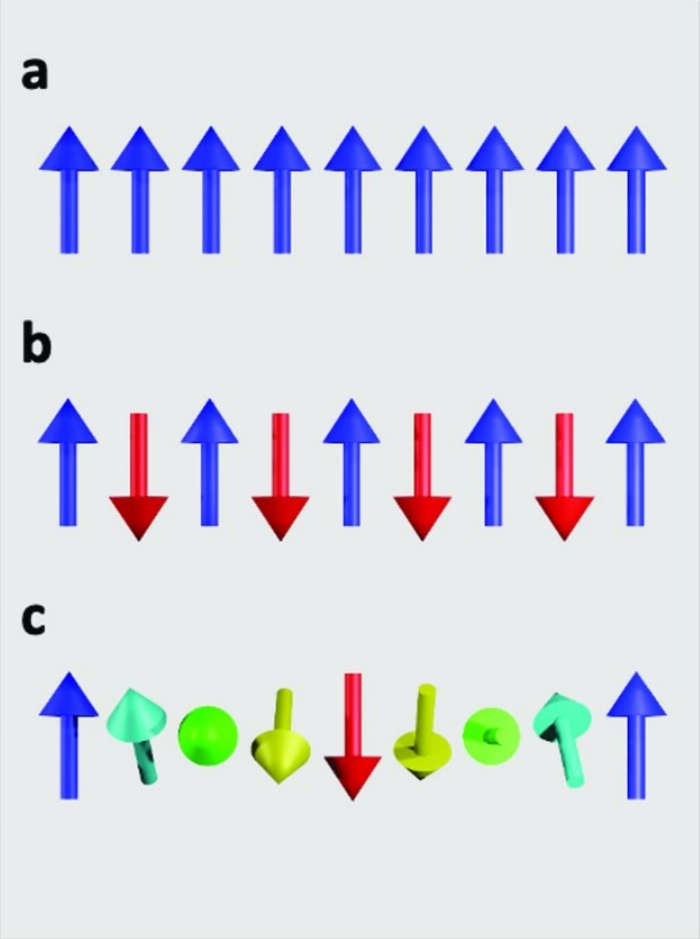

Figure 2-13 Spin alignment with (a) parallel (FM) or (b) antiparallel (AFM) configuration. In (c) the combination of Heisenberg and DM interactions leads to a non-collinear spiral state. [adapted from ref. [201]]

octahedra which, as a countereffect, cause bonds angle between the paramagnetic cations deviating from 180° (a symmetry constraint required for GKA prediction). As mentioned before, these distortions, described by the Glazer notation, modify the orbital overlap between the species and, as a consequence, lead to more complex non-collinear spin arrangements driven for example by the so-called Dzyaloshinskii–Moriya (DM) interaction [98] [99] or Single Ion Anisotropy (SIA) [100]. In the first mentioned interaction antisymmetric exchange due to spin-orbit coupling favours a spin canting of the magnetic moments that usually leads to an incommensurate magnetic structure [101] [102] [103], where spins are not collinear to each other but irrational values for propagation vector are needed to reproduce their order along the crystalline cell. The expression for the Hamiltonian term of DM, which is induced by inversion symmetry breaking in non-centrosymmetric lattices, is reported here below:

$$H_{i,j}^{DM} = D_{ij} \cdot (S_i \times S_j) \quad (8)$$

Where D_{ij} is the atomic DM vector, whose direction depends on the particular crystal symmetry, and it has a null contribution if the two neighbouring magnetic ions *i* and *j* are in line with the single third ion responsible for the super-exchange mechanism. As a consequence, non-collinear antiferromagnetic perovskites show weak ferromagnetic character even with large macroscopic resultants.

Moreover, the cation ordering, thus the crystalline arrangement, is crucial in the strength of the final interaction to allow the generation of a specific magnetic structure, collinear or more complex. When B-disorder occurs, perovskites more commonly display magnetic frustration, which usually ends in a spin-glass state, where the spins have a random arrangement but behave in a cooperative way, able to align in an ordered magnetic state at the freezing temperature [104] [105] [106]. Additionally, it should be noted that in double/quadruple perovskites it is common to observe the presence of one particular cation with mixed-valence state configuration. A great example is represented by manganese, which can be inserted both at the A and B sites with 2+, 3+ or 4+ oxidation states, leading to variable competing interactions between the other species, as in the cases of $MnCu_3Mn_4O_{12}$ quadruple perovskite [107], $(La,Ca)MnO_3$ solid solution [108] or $Ca_3Mn_2NbO_9$ [109].

Besides Mn^{2+} [110], other paramagnetic cations can be introduced at the A site, namely several syntheses have been reported with A= Nd^{3+} [111], Gd^{3+} [112], Sc^{3+} [113], In^{3+} [114]. The magnetic tendency of these cations can sometimes cause a magnetic spin coupling with the B site cations [115] or other interesting properties like the magnetocaloric effect [116]. Additionally, by playing with the size of the A cation, it is possible to induce the tilting of oxygen octahedra, with the consequent modification of B-O orbital overlap and thus a change in the character of the magnetic interactions [117].

2.6 Multifunctional perovskites

As described in the previous paragraphs, there are several advantages of working with perovskites, primarily due to their versatile character. Indeed, this family of chemical compounds displays a wide range of physical properties that can be merged together, in order to obtain the so-called multifunctional materials. From the general definition, a multifunctional material can merge simultaneously more than one functionality in a single crystallographic phase. For this reason, it is required to invest time and energies in the development of new materials like these to advance in technological applications.

Many multifunctional perovskites have been reported in a large number of intriguing research fields and, particularly, much progress has been done in energy conversion applications, a critical subject of recent years. Namely, an interesting combination of the right electrical and catalytic properties in single or double perovskites allows their development in solid oxide fuel-cells as anodes, cathodes or electrolyte components, like (LaSrCa)TiO_3 [118] or $LaNiO_3$ [119]. $ATiO_3$ perovskites have extensively been reported to show piezo-photocatalytic properties, applied for the purification of air and water from organic and inorganic pollutants. In these high-polarizable crystalline systems, external ultrasonic, heat or/and light irradiation leads to the tilting of the valence and conduction bands with the final formation of reactive oxygen species. Their efficiency and selectivity can be tuned by controlling the morphology, the oxygen vacancies or the doping cations content. Some examples are constituted by $BaTiO_3$-, $SrTiO_3$-, $PbTiO_3$-based perovskites with substitutions at the A site. Moreover, a subgroup of these materials, like $Sr_xCa_{1-x}TiO_3$ [120], displays antibacterial activity for specific microbial species. By also considering the thermal properties of perovskites, some thermoelectric and photothermal applications have been reported for (Sr,La)(Co,Ti)O_3 and (La,Sr)CoO_3, respectively.

From the magnetic point of view, an intriguing class of multifunctional perovskites is constituted by those reporting half-metallicity. Namely, these compounds, mostly ferro- or ferrimagnets, display a conductor behaviour only for a specific spin orientation, while the other spin channel acts as a quasi-insulator.

The most studied family of half-metal perovskites is A_2FeMoO_6 with A = Ca, Sr, Ba, in which this character is a consequence of orbital hybridization [121] [122]. Moreover, these compounds usually present tunnelling (and even giant or colossal) magnetoresistance effects, enhanced by the presence of grain boundaries and ordering of B cations.

One of the most promising applications of multifunctional perovskites is represented by the ferro-photovoltaics or ferro-photocatalysts, in which the ferroelectricity plays a central role as a driving force for the additional functionality, as already discussed in the previous paragraphs. For the latter behaviour, $PbSrBiNbO_3$ has been reported, while one of the most famous ferro-photovoltaic materials is Bi_2FeCrO_6 double perovskite. This compound, by a proper design of the multilayer cell, can reach a photoconversion efficiency of close to 8% [123]. Besides its ferroelectric and photovoltaic properties, Bi_2FeCrO_6 is also a proper multiferroic material.

2.6.1 Multiferroic perovskites

Multiferroics are characterized by the coexistence of two or more primary ferroic orders in a single phase, such as ferromagnetism, ferroelectricity, ferroelasticity or ferrotoroidicity. These orders are in principle incompatible because magnetism is usually induced by the presence of unpaired electrons, i.e. a partially filled d-shell, whereas d^0 cations help the occurrence of ferroelectric distortions. Therefore, the simultaneous presence is not so common in chemical compounds, making multiferroics a rich and stimulating playground for fundamental material science [124]. Particularly, the simultaneous breaking of both spatial and time inversion symmetry is required to accommodate multiferroicity in a single phase. This strong symmetry constraint is proper of only 13 Shubnikov magnetic groups over 122 (1, 2, 2', m, m', 3, 3m', 4, 4m'm', m'm2', m'm2', 6, and 6m'm'), according to Landau-Lifschitz theory applied to the magnetic crystals [125]. In order to retain both magnetism and ferroelectricity in perovskites, a possible solution is to assign these two fundamental properties to the B and A sites of the perovskites, respectively, by introducing magnetic B cations and stereochemically active cations, like Pb^{2+} or Bi^{3+} at the A site. For instance,

Bi_2NiMnO_6 double perovskite has been addressed to be ferroelectric below 470 K, but its FM state arises only at a relatively low temperature (around 140 K) [126].

Among these exotic materials, the magnetoelectric multiferroics are characterized by the magnetoelectric (ME) effect, which is any coupling between the electric and magnetic properties [127]. The analytical description of the linear ME effect is expressed by the ME susceptibility tensor α_{ij}, which derives from the power series expansion of the component of Helmholtz free energy F dependent on magnetic H and electrical E fields:

$$F(E,H) = F_0 - P_i^S E_i - \mu_0 M_i^S H_i - \frac{1}{2}\epsilon_0 \chi_{ij}^e E_i E_j - \frac{1}{2}\mu_0 \chi_{ij}^v H_i H_j - \alpha_{ij} E_i H_j - \frac{1}{2}\beta_{ijk} E_i H_j H_k - \frac{1}{2}\gamma_{ijk} H_i E_j E_k + \cdots \quad (9)$$

where β and γ coefficients represent fourth power order effects. P_i and M_i are respectively the electrical polarization and the magnetization, differentials of the free energy and in terms of electrical χ^e and magnetic χ^v susceptibility:

$$P_i = \sum_j \varepsilon_0 \chi_{ij}^e E_j + \sum_j \alpha_{ij} H_j \quad (10)$$

$$\mu_0 M_i = \sum_j \mu_0 \chi_{ij}^v H_j + \sum_j \alpha_{ij} E_j \quad (11)$$

In order to display a non-zero contribution, the α_{ij} tensor must be antisymmetric under time-inversion symmetry, as previously described in terms of point groups, and this condition is quite rare [128]. Moreover, the ME coupling between magnetic and electrical properties is very intriguing also from the point of view of technological applications, but many of the known magnetoelectric multiferroics are characterized by low ordering temperatures, and this prevents their use in technology.

Starting from this background, during my PhD activity I have dealt with the synthesis of novel double perovskites with the aim of tuning physical properties and trying to merge multiple functionalities related to magnetism and electrical properties.

3 High Pressure/High Temperature synthesis

3.1 Learning from nature: perovskites under pressure

As underlined in the previous chapter, the perovskite structure offers a rich playground in material science, by playing with the chemistry at the A and the B sites in order to merge and control several functionalities in a single crystallographic phase. Since these kinds of compounds are naturally formed under the terrestrial crust, where extreme conditions of temperature and pressure are present, it is reasonable to explore the synthesis of novel perovskites by reproducing such exotic geological conditions in research laboratories. Indeed, it has been demonstrated that performing solid-state reactions under High pressure/High temperature (HP/HT) conditions represents a tool to stabilize metastable perovskite structures that cannot be obtained with any other techniques. In this way, a wider range of possible chemical substitutions can be investigated by forcing some cations to fit the perovskite A or B sites, exploring novel compositions and rarer physical properties.

Although the effect of a very high temperature (more than 1000°C) is a standard experimental practice, for instance with the use of chamber furnaces, high pressure conditions in the GPa regime are definitely more tricky to reproduce since common hydraulic presses reach “only” hundreds of bars (order of 0.01 GPa). Extremely high pressures, from 100 GPa to around 400 GPa, can be achieved in the so-called Diamond anvil cells (DAC), compact devices of ~60 mm in diameter constituted by a pair of opposite diamonds compressed. Between the two components, the applied pressure is thus very high but confined in a narrow space, limited to a volume around 10^{-5} mm^3, preventing the use of such devices for synthesis processes while useful and catchy for in-situ studies under pressure. On the contrary, large volume presses (LVP) allow performing solid-state reactions in

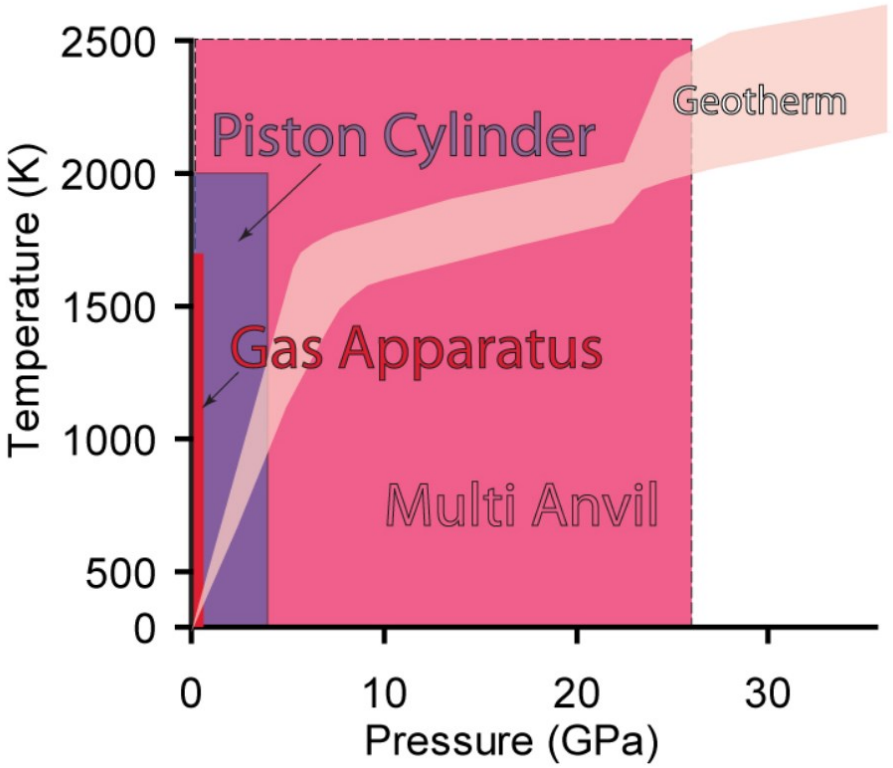

Figure 3-1 Temperatures and pressures achievable in different HP/HT apparati for solid-state chemistry. [adapted from ref. [202]]

a larger volume, on the order of hundreds of mm^3, by sacrificing the magnitude of DAC achievable pressures. For instance, with the piston-cylinder press it is possible to produce pressures between around 1 GPa and 3 GPa.

An additional key consideration is that it is quite complex to recreate an isotropic force acting on a certain volume, unless considering a vapour/fluid compression as for the hydrothermal syntheses, the usual method to grow synthetic single crystal for commercial value. Nevertheless, this technique is not safe since dangerous solvents such as ammonium chloride are generally required and isotropic pressures of up to 3-4 kbars (i.e. fractions of GPa) can be obtained.

In this scenario, multi-anvil LVP presses constitute an optimal solution to reproduce a static isotropic pressure condition in the GPa regime, combining the heating effect. There are many devices and geometry variants reported in the literature about different LVP apparati, such as the Belt [129], Kawaii-type [130], or Cubic anvil press [131], but I will extend the discussion only to my Walker-type multi-anvil press with which I worked in the years of my doctorate.

Figure 3-2 Walker-type multianvil press at IMEM-CNR (Parma, Italy).

3.2 Walker-type Multianvil press

During my PhD research activity, I've personally carried out many solid-state reactions with the Walker-type multi-anvil press, available in our HP/HT laboratories at IMEM-CNR. This geometry module was first proposed in 1990 by the geologist Dr. David Walker, who modified the well-established octahedron-within-cubes geometry with a simpler and compact design, in order to be adapted to the more conventional oil presses used in piston-cylinder laboratories [132] [133].

In this system it is possible to explore the pressure range between 2 GPa and 22 GPa by following the principle of intensification. Namely, the unidirectional pressure, applied vertically by a cylindrical piston of an oleodynamic press, is

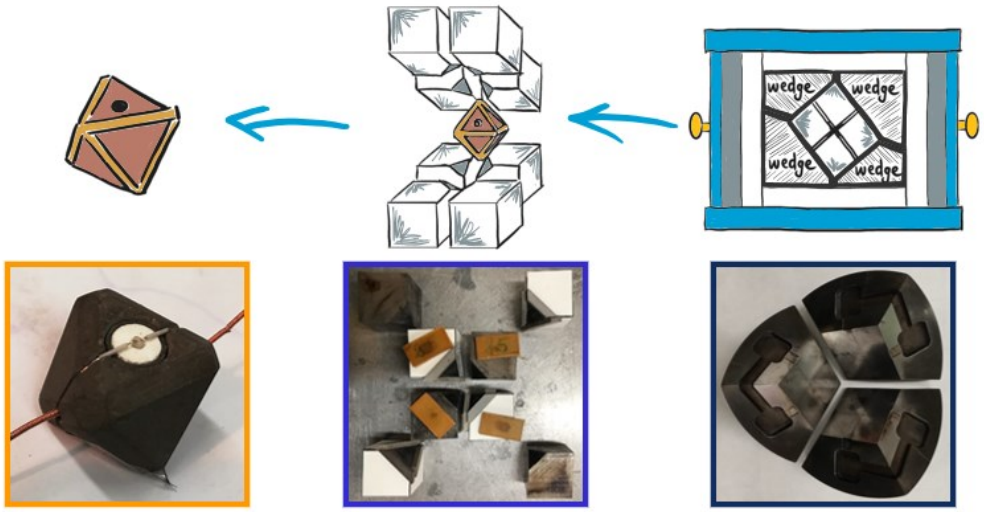

Figure 3-3 Pressure decomposition elements in the Walker-type Multianvil press: (from right to the left) wedges, cubes, and octahedral cell.

decomposed and amplified thanks to different solid modules (i.e. the anvils) with increasing hardness, leading to a final quasi-isostatic pressure acting on the reaction cell. The pressure decomposition can be described following the scheme of the anvils' configuration reported in Figure 3-3. Firstly, the axial pressure is applied to the upper circular surface of a quite large cylindrical case (Figure 3-3, section of this case in the right panel, light blue). This modulus hosts inside six tempered steel wedges which are placed in a cylindrical geometry and pushed by the main piston ramp. The action of these wedges is to amplify and split the external unidirectional pressure along three orthogonal directions and apply the load in its inner internal cubic cavity. In this cavity is filled by eight tungsten carbide cubes packed together, visible in the central panel of the previous figure, each one designed with a truncated edge. The cubes are spaced to each other with pyrophyllite gaskets, positioned at the truncated boundary in order to reduce the load dissipation to friction. The cubes' truncation leaves an octahedral cavity at the centre of the as-assembled cube where the force is again distributed along 4-fold octahedral geometry. This is the place in which the octahedral reaction cell is located (Figure 3-3, left panel). This element, that constitute the core of the solid-state reaction, is made by porous MgO doped with 5% of Cr_2O_3, which exhibits a plastic to elastic deformation in the GPa regime, allowing in this way an almost isotropic effect of pressure on the sample, which is introduced inside the octahedral cell by a tricky cylindrical assembly. Specifically, as shown in Figure 3-4, the cell is drilled along two opposite octahedral faces, allowing the insertion of a hollow cylindrical

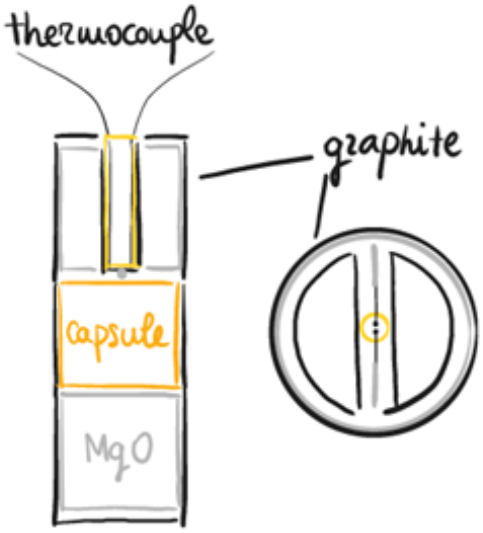

Figure 3-4 (left) Cylindrical assembly inside the octahedral cell, with MgO elements surrounding the capsule in the middle part. On the top of the capsule, a thermocouple provides temperature control. (right) Vertical view of the upper part of the capsule, with cut in half graphite disk.

graphite oven as the furnace of the synthesis process. Inside the graphite, three MgO components are finely shaped in order to protect the central gold or platinum thin foil capsule where at the end the reagents' powdered mixture is introduced. The heating procedure is then performed by the Joule effect, by providing an external AC current to two opposite tempered steel wedges, which are insulated from the others while they are put in direct contact with those two cubes which act on the top and the bottom side of the octahedra where the graphite furnace emerges. The electrical insulation from the other anvils and cubes allows an efficient heat conductivity without dispersions in the whole system. A small thermocouple (generally an S-type made by wires of Pt and Pt 90%-Rh 10%) enters through one of the two graphite disks, passes through the top MgO sleeve and it is positioned in contact with the upper layer of the reagents' capsule, enabling the control of the temperature during the entire reaction process with precision around 0.1°C. Along the whole capsule dimensions, a maximum temperature gradient of ΔT of about 1°C/mm, while the pressure gradient ΔP=0.1 GPa/mm can be estimated.

Due to the fact that the Walker-type multianvil press can cover a very extended range of pressure, from 3 GPa to 22 GPa as previously said, different sizes of the octahedral cell, and consequently different sizes of truncated tungsten carbide cubes must be used to achieve a specific pressure regime. Particularly, three different sets of cubes (and cells) are available in our press. A fundamental size parameter to consider is the truncated edge length (TEL) of the cube with respect

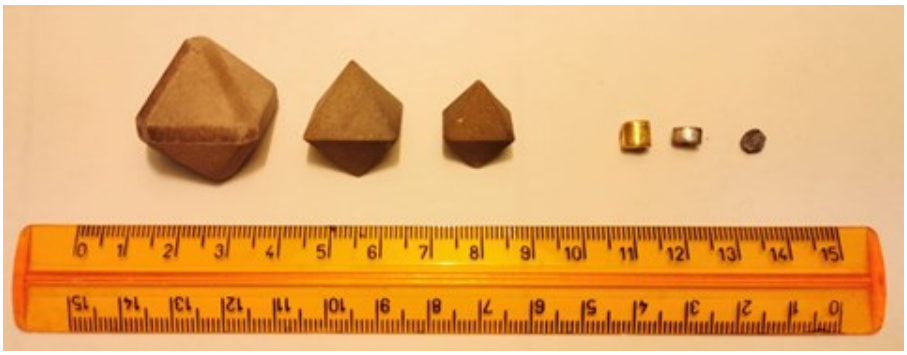

Figure 3-5 Octahedral cells related to 25/17, 18/11, and 14/8 assemblies, with the relative sample capsule.

to the length of the non-truncated one. In this way, we can distinguish TEL of 17 mm, 11 mm, and 8 mm, commonly identified as 25/17 (range 2-6 GPa), 18/11 (range 6-15 GPa), and 14/8 (range 15-22 GPa) cubes. Each set of cubes hosts an octahedral cavity increasingly smaller by lowering the TEL, as pictured in Figure 3-5. Therefore, all the assembly components are proportionally modelled to fit inside the octahedral cell. The most relevant ultimate size is the one of the reagents' capsule, which determines the mass/volume amount of the final sample. As visible in Figure 3-5, the cylindric capsules are around 5-3 mm in diameter, and for the bigger assembly, 25/17, through which pressures up to 6 GPa can be reached, samples with a mass of around 700 mg can be obtained, a relatively large amount considering the extreme conditions applied during the synthesis.

The HP/HT solid-state reactions performed with our Walker-type multianvil apparatus follow a specific and got up to speed protocol which is reported below.

1) The first step involves the gradual increase of the pressure applied to the whole system, up to the selected set-point pressure that acts on the sample. This pressure ramp is slow, typically with a rate of around 600 Pa/min, in order to prevent damages and even breaking of anvils due to high mechanical stress, and to give the system the right time to adapt to the stress condition.
2) When the P set-point is achieved, the heating process can start via Joule effect from room temperature up to the selected T set-point, with a temperature ramp of 25°C/min or 50°C/min. After the stabilization of the system at the selected final temperature, those PT conditions are kept for a certain reaction time t.

3) Once the solid-state reaction is concluded after t, the system temperature is abruptly quenched down to room temperature by interrupting the power supply unit. When also the external system of anvils is significantly cooled, not so far from room temperature, it is possible to start releasing the pressure to ambient conditions. As in the first step, this process must be slow (about 300 Pa/min) to safely keep all the components.

The thermal quenching constitutes the key step of the procedure since it allows to freezing of the HP/HT metastable phase and keeps it stable at ambient conditions.

However, the best solid-state synthesis conditions (i.e. pressure, temperature, and duration time) required to get a pure single crystalline phase of a novel compound are a priori unknown. Some hypotheses on the starting P, T, and t values to try can be provided by considering similar compounds previously synthesized, but having the possibility to vary three different parameters considerably amplify the phase-diagram regions to be studied. Additionally, working with such exotic conditions a completely new science can be found, so even undesired spurious phases are not easily identified because of the lack of information on such uncharted impurities in scientific databases. Considering all these aspects, without in-situ studies and considering the requested time for one synthesis, the synthesis conditions' optimization of a new compound is mandatory for its premier presentation to the scientific community, making this kind of research quite hard and laborious. Moreover, it must be underlined the efforts required to perform every single HP/HT synthesis which somehow compensate for the unique potentialities of this apparatus. The preparation of all the components, as the shaping of MgO/graphite pieces with CNC micro-lathe, the covering of cubes with gaskets and insulating elements, the self-manufactured thermocouple, the capsule closing and cold-welding, and of course the assembly of all these elements together require around two days of steady work. Usually, the pressure ramp is done overnight, while the heating and the synthesis process can be concluded the next day. So, in approximately three days, an HP/HT solid-state reaction can be carried out. Unfortunately, excluding anvils, all the manually made and assembled

components are destroyed in each synthesis, highlighting the energy, costs and time-consuming character of this technique.

Nevertheless, I have to say that the multianvil press evokes in me conflicting emotions, typical features of the best love-hate relationships, since each of the sweaty dirty forty-six syntheses that I have performed during my PhD leaves me a sense of pride for my ability to dominate such extreme conditions, ending with a tiny polycrystalline cylinder of something unknown. Several synthesis attempts miserably failed with high impurity levels or even worst the breaking of cubes or losing of thermocouple control, but some successful results, that I will present you in the experimental part, have definitely balanced and rewarded my efforts. It has required great dedication. The artistic side of my personality has been quite satisfied by this act of creativity.

Before entering the description of my HP/HT new perovskite compounds, in the following chapter I will describe the characterization techniques that I have employed for their physical properties investigation. Like the synthesis process, the physical characterizations also represented a consistent part of my experimental work, mandatory facing novel materials. Particularly, I had the chance to personally perform the majority of the measurements that I will report later. Spending my time on such techniques really helps me to acquire quite good knowledge, particularly from the structural point of view, on how to solve complex challenges related to my materials.

4 Characterization techniques

4.1 Introduction to structural characterization

When you have in your hands a new material, with not so much prior knowledge about it, the characterization of its structural properties is primarily fundamental. Specifically, by performing my HP/HT solid-state reactions, I ended up with a bulk polycrystalline perovskite material which differs significantly in its physical and chemical properties from the starting powder reagents that I initially selected. Additionally, the extreme HP/HT conditions employed intrinsically lead to highly defective polycrystalline products, characterized by the twinning of the crystals [134] [135], while the growth of quite big single crystals (~1 mm) is not so common. Thus, most of the time, the as-obtained defective small grains (generally of the order of tens micrometres) prevent the use of conventional single crystal characterization techniques. Moreover, since the polycrystallinity of HP/HT highly defective compounds leads to intrinsic challenges and possible non-unique or trivial structure solutions, I exploited the benefits of using different kinds of matter probes, such as electrons, X-rays, and neutrons. The combination of such diffraction techniques (i.e. selected-area electron diffraction mode of transmission electron microscopy, X-ray powder diffraction, and neutron powder diffraction) represents a robust strategy to extract complementary crystallographic information with the aim to properly solve the crystal structure and the space-time symmetry of novel complex compounds.

Since I have extensively characterized the crystallographic-structural properties, and also learned how to perform data analysis of such results by exploiting such distinctive kinds of matter-probe interactions, I want to discuss and

examine in detail the employed diffraction techniques and their potentialities, while a shorter discussion on the other characterization techniques will follow.

4.2 X-rays Powder Diffraction

Powder Diffraction (PD) is one of the most important methods to investigate the structural, and even morphological, properties of crystalline solid materials, especially when single crystals cannot be employed. Namely, PD is nowadays a standard technique for compositional and microstructural analyses, such as for the detection of crystalline phases in mixed composition samples, with the possibility to perform quantitative analysis in order to evaluate the volume fractions of each component. Nevertheless, PD constitutes an even more powerful tool for crystallographers in providing essential information to solve and refine the structural symmetry of crystals, especially by using high-resolution sources and high-performance data analysis methods. These structural information are enclosed within the diffraction pattern, as the result of the scattering process between a specific probe, characterized by a wavelength comparable with the interatomic distances, and the crystal lattice of the large number of randomly oriented crystallites.

I have performed powder X-rays diffraction (PXRD) experiments with a Rigaku Smartlab XE diffractometer, available at the Department of Chemistry, Life-Science, and Environmental Sustainability of the University of Parma. This instrument, shown in Figure 4-1, works in the Bragg-Brentano geometry, making use of Cu Kα wavelength ($\lambda = 1.5406$ Å), and it is equipped with an Anton Paar TTK 600 chamber which allows the vacuum control and temperature-dependent PXRD measurements from 80 K to around 900 K. For standard acquisitions, such as those that I will report in the experimental section, a Ni filter is used to suppress the K_β contribution, while soller slits (commonly 5.0°) are used both on the incident and diffracted beam, whose signal is collected using a HyPix3000 detector. Measurements can be performed in the 10–150° 2θ range with 0.01 step size, 0.5° min^{-1} speed, acquiring in continuous 1D mode.

Figure 4-1 Rigaku Smartlab XE diffractometer of the Chemistry Department of University of Parma.

In general, a monochromatic X-rays beam undergoes a diffraction process with the crystal lattice of the crystallites, describable by Bragg's law:

$$\lambda = 2d_{hkl} \sin \theta_{hkl} \tag{12}$$

where a series of crystallographic d-spacing, associated with a particular set of Miller indices (hkl), can be measured by moving the detector at different angular positions. The recorded diffraction pattern contains information regarding:

- the unit cell symmetry and size from the peak positions;
- the atomic distribution in the unit cell from the peak intensities;
- the particle size and defects from the peak shapes;
- the diffuse scattering of matrix or amorphous phases, as well as the sample holder, from the background.

Particularly, different contributions are involved in the peak intensities of a powder pattern, which can be summarized in the following equation:

$$I_{hkl} = K \cdot LP(\theta_{hkl}) \cdot A \cdot y \cdot m_{hkl} \cdot |F_{hkl}|^2 \tag{13}$$

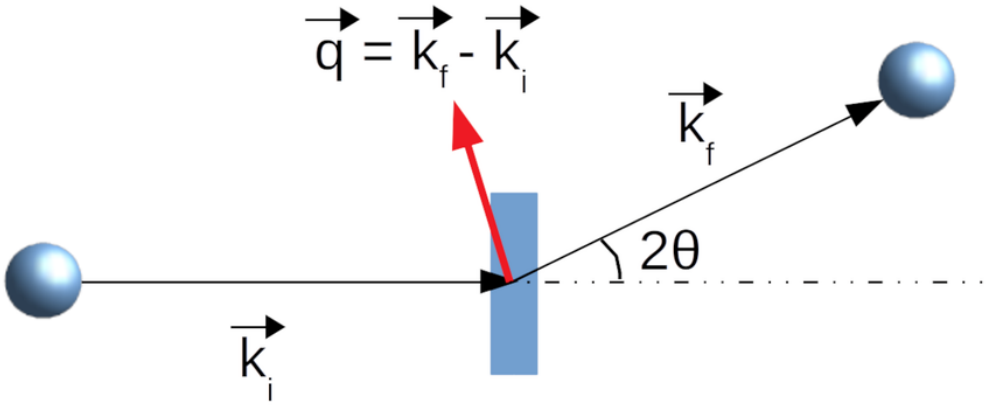

Figure 4-2 Elastic scattering process between X-rays and matter. The transfer momentum q is equal to the difference between the final and the initial radiation wave vector. [adapted from ref. [204]]

where K is a scale factor due to the kind of probe (i.e. incident beam intensity and wavelength) and the set-up geometry (i.e. slits, sample to detector distance), LP is the combination of Lorentz and polarization factors θ-dependent, A and y are the absorption and the preferential orientation extinction factor respectively, m is the (hkl) reflection multiplicity, while F_{hkl} is the structure factor of the (hkl) reflection. Moreover, the diffraction lines of real patterns are strongly affected by the particle size, local disorder and microstrain, which contribute to a broadening effect of the δ function that theoretically represents each non-extinguished reflection. The real diffraction peaks are thus characterized by a profile function, whose shape can be mathematically described with a Gaussian, Lorentzian, or Pseudo-Voigt function, which brings these morphological features.

The structure factor F gives a fundamental contribution from the crystallographic point of view, as it correlates the intensity of the diffraction peaks to the N atomic species arrangement in the unit cell as follows:

$$F_{hkl} = \sum_{i=1}^{N} f_i \cdot \exp\left(2\pi i(h,k,l) \cdot (x_i, y_i, z_i)\right) \qquad (14)$$

where f_i is the atomic scattering factor for the atom i, while x_i, y_i, z_i are its coordinates in the cell. The correlation between the appearance of the diffraction pattern with the crystal lattice motif starts to become clearer. Besides, the X-ray photons, characterized by wavelengths around ~0.1 nm and a corresponding initial wave vector $\overrightarrow{k_i}$, interact with a specific atom undergoing a scattering process, schematically reported in Figure 4-2, by its atomic charges, particularly by the electronic cloud. The f factor differs significantly varying the atomic species charge,

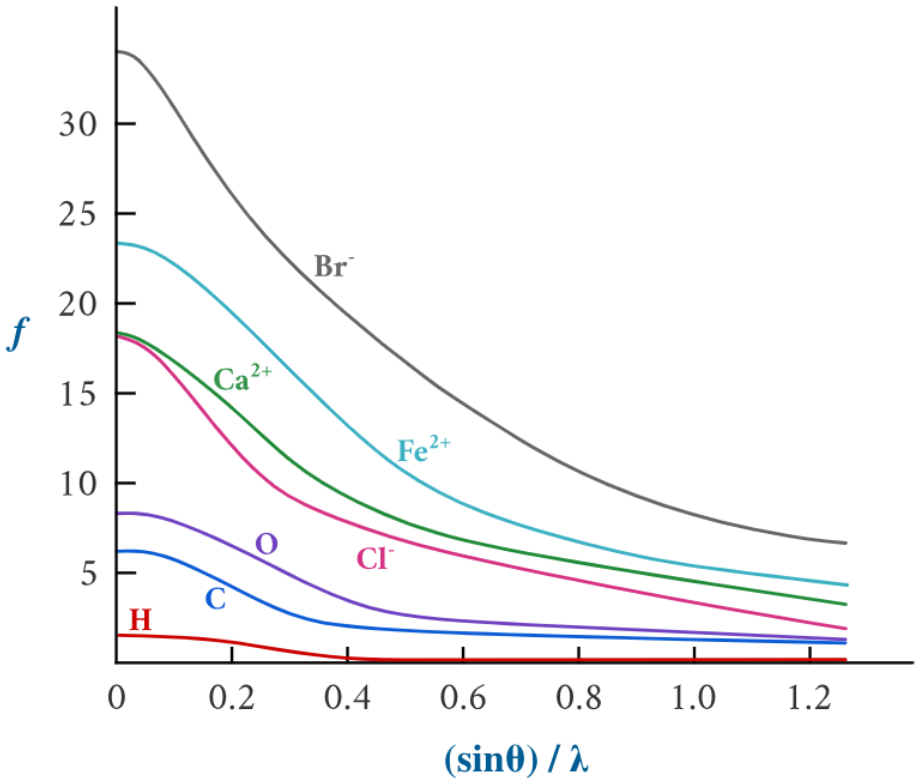

Figure 4-3 Scattering factor for different atomic species with its θ-dependence. [adapted from ref. [203]]

as it is deeply correlated with the number of electrons. Namely, as shown in Figure 4-3, the f value of a certain species is effectively proportional to its atomic number Z, making low Z elements such as H not visible, and decreases from the maximum value f($\vec{q}$=0)=Z if the scattering angle (or the momentum transfer in the scattering process $\vec{q} = \overrightarrow{k_f}\text{-}\overrightarrow{k_i} \propto (\sin\theta)/\lambda$) becomes larger.

4.3 Neutron powder diffraction

An analogous discussion can be done in the case of neutron scattering. However, as neutrons have different characteristics from X-rays, some essential observations are needed.

Neutrons, first discovered by J. Chadwick in 1932 [136], are neutral subatomic particles with wave-particle duality characterized by a non-zero spin, equal to 1/2, carrying out a magnetic dipole moment, making them interactive with magnetic species. The interaction of the neutron spin with the magnetic field of unpaired electrons generates an effective magnetic scattering, which intrinsically

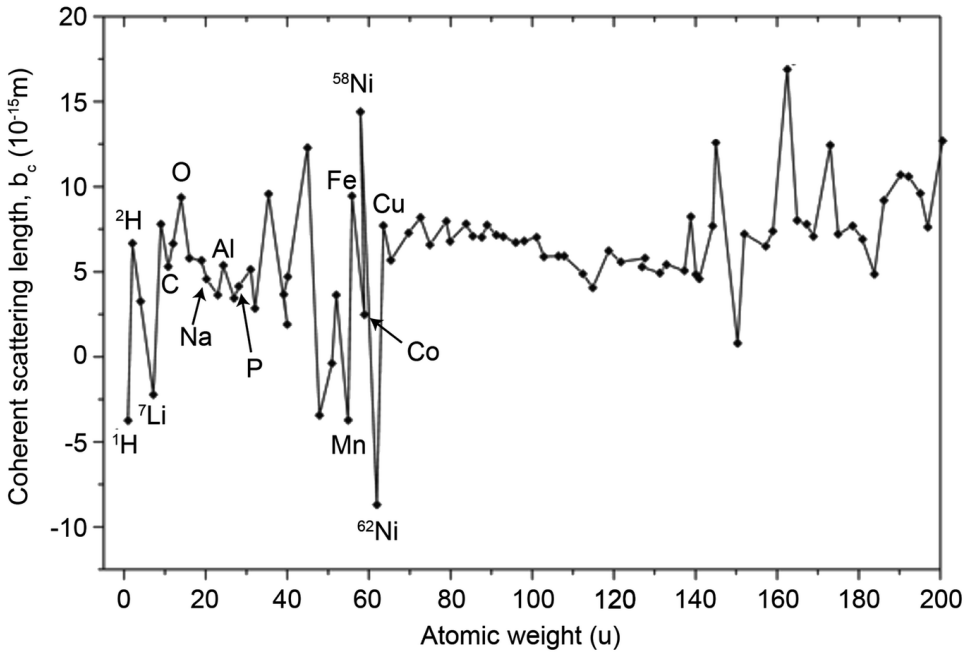

Figure 4-4 Coherent neutron scattering lengths for different atomic species as a function of the atomic mass. [adapted from ref. [205]]

unveils the magnetic moment arrangement in crystallographic systems. Moreover, in contrast to X-rays, neutrons interact with the nucleus of the atom. For this reason, a different parameter respect with to the atomic form factor f for X-rays must be considered during the scattering process, which is the neutron scattering length b. This parameter, connected to the cross-section σ of a certain atom, is independent of the transfer momentum $\vec{q}$, while it changes with the isotope because of the change in nuclear structure and may be positive or negative. Actually, b can be expressed as the combination of two distinct contributions, related with the coherent or incoherent scattering respectively, but only the former b_c is of interest in order to obtain structural information at the atomic level, as neutron diffraction, while the latter b_i primarily contributes to the background signal. Examples of coherent neutron scattering lengths are reported in Figure 4-4. In this way, neutrons constitute a complementary probe to X-rays in terms of the atomic contrasts by different scattering cross sections.

As previously mentioned, the magnetic interaction of the neutron spin with each spin of the nuclei leads to magnetic neutron scattering, in analogy to the nuclear one. Indeed, different spin states are associated with a particular magnetic form factor, which is $\vec{q}$ dependent and must be considered. However, it must be underlined that, from magnetic cross-section considerations, only the components

of the sample magnetization that are perpendicular to the neutron's momentum transfer contribute to magnetic scattering. If the interacting sample displays a magnetic spin arrangement (i.e. a long-range magnetic structure), the magnetic ions will produce a diffraction pattern constituted by magnetic reflections. By associating the magnetic peaks with the nuclear ones, it is possible to reconstruct the magnetic structure in relation to the crystallographic unit cell and symmetry. The capability of neutrons to probe both the nuclear and magnetic structure makes neutron diffraction a key technique for the characterization of crystalline magnetic compounds.

In order to perform diffraction experiments, the neutron source, which can be continuous and generated in a nuclear reactor (for instance at ILL facility, Grenoble, FR), or pulsed from a spallation process (as at ISIS facility, Didcot, UK), must be properly tuned to obtain a characteristic neutron wavelength comparable to the lattice distances. For nuclear and magnetic diffraction experiments, eventually characterized by long-range ordering, the requested λ can vary between 1 Å and 30 Å, thus with energies from 100 to 0.1 meV. This energy range corresponds to the so-called cold or thermal neutrons, that can be selected with proper moderating mediums and a monochromator if on continuous source where monochromatic beams are used.

Contrarily to more standard constant-wavelength (CW) diffractometers, many neutron diffractometers take advantage of the wave-duality De Broglie's equation which connects the neutron wavelength to its velocity, and can be expressed in terms of energy:

$$E\ (meV) = 5.227 \cdot v^2\ (km \cdot s^{-1}) \tag{15}$$

By exploiting this relation, neutrons with different wavelengths produced by a pulsed source can be discriminated by the characteristic time required for the diffracted neutron to travel from the source to the detector, which is called the time-of-flight (TOF) of neutrons. The d-spacings are thus proportional to TOF values considering the diffraction geometry (i.e. source-sample and sample detector distance) and the entire diffraction pattern is recorded in a single fixed detector. The main advantage of TOF diffractometers with respect to the CW ones is to provide

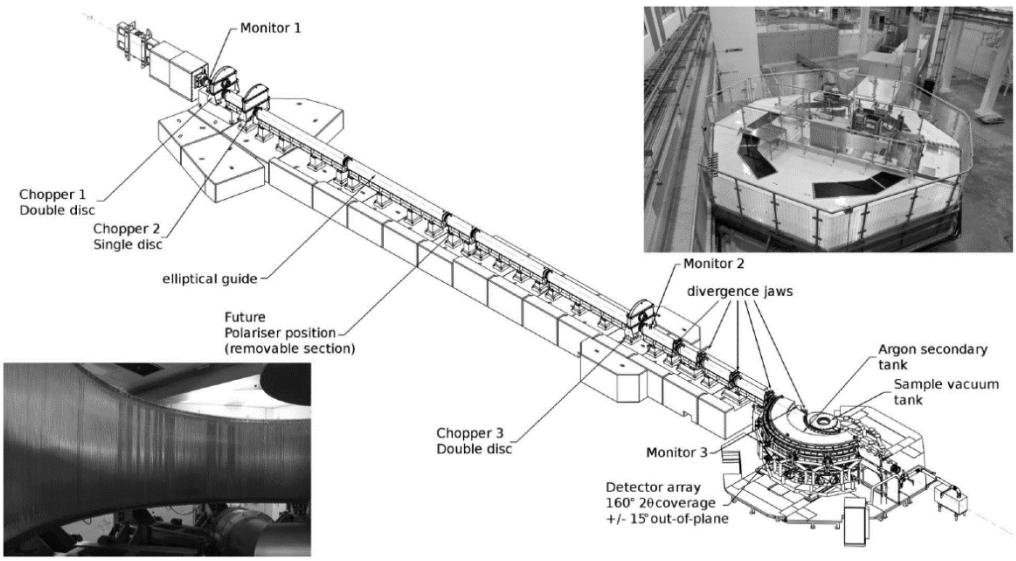

Figure 4-5 Schematic layout of WISH diffractometer, with the top view in the TS2 (right) and the ^{3}He detector array inside the blockhouse. [adapted from ref. [137]]

patterns with a nearly constant resolution (largely determined by the pulse shape, the source-sample and sample detector distances) in a wide range of d-spacing, despite an angular contribution is also present.

I have performed neutron powder diffraction experiments on the TOF diffractometer WISH [137], at the ISIS facility, Didcot, UK, via proposal acceptance (n. RB2320119). This instrument, schematically pictured in Figure 4-5, works with high-brilliance cold neutrons (λ range is 1.5 – 15 Å) tuned by a solid methane moderator, operating at 40 K. A series of choppers are used as bandwidth-selectors, avoiding possible frame-overlaps. After following a 40 m flight path, the neutrons impact the sample, which is placed at the centre of a blockhouse (Figure 4-5, right). The detector system is constituted by ^{3}He gas position-sensitive tubes (diameter of 8 mm, active length of 1 m) located on a cylinder at the same distance of 2.2 m from the sample. In this geometry, the detector array, divided into ten banks grouped two by two symmetrically, covers a broad 2θ range (from 10° to 160°) with a resolution of 0.2°, allowing the investigation of a large d-spacing region (0.7-50 Å). Moreover, the instrument is equipped with many sample environments, for instance, cryostats, furnaces, and pressure cells, in addition to a 14 T vertical magnet to perform measurements in very high magnetic field conditions. These features make WISH a very powerful instrument for magnetic and nuclear structure determination and refinement.

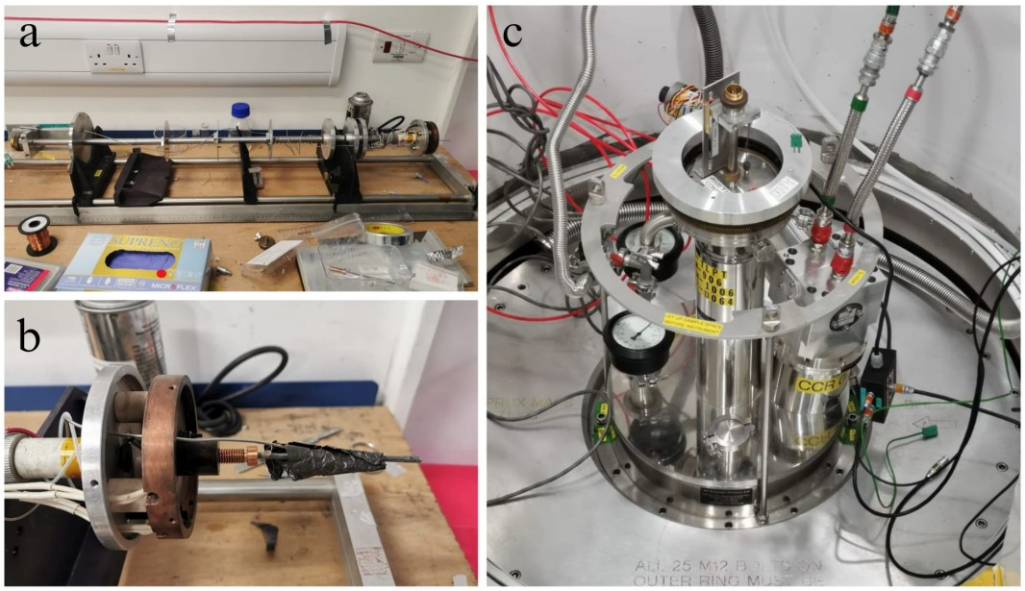

Figure 4-6 WISH sample holder, constituted by a long metallic bar (a) where at one end the sample is located (b), with the adjacent elements (i.e. thermocouple) shielded by a Gd foil. The bar is inserted in the sample environment (c).

The powder diffraction data from my HP/HT perovskites were collected varying the temperature condition, in heating with a CCR furnace while in cooling with a helium cryostat, covering a T range from 5 K to 370 K. The powdered sample is inserted in a thin vanadium can as a sample holder, since this material displays only an incoherent scattering signal. Part of the sample holder, not containing the sample, is shielded with gadolinium thin foils as a good neutron absorber, and it is mounted at the end of a long stick, which is then inserted in the desired sample environment at the centre of the instrument blockhouse, as shown in Figure 4-6.

4.4 Handling powder diffraction data: structure determination and refinement

Treating with novel compounds from HP/HT, the main advantage of combining powder diffraction experiments is the possibility of extracting all the necessary information to determine their crystal and magnetic structure. As mentioned in Paragraph 4.2, many crystallographic information can be provided by analysing the diffraction pattern, i.e. evaluating the relative intensities and angular position of each reflection. In general, it is possible to list a sequence of steps to follow in order to solve a diffraction pattern, in an analogous way for neutrons, X-rays, or in general photons probes [138] [139]. Since I personally carried out these

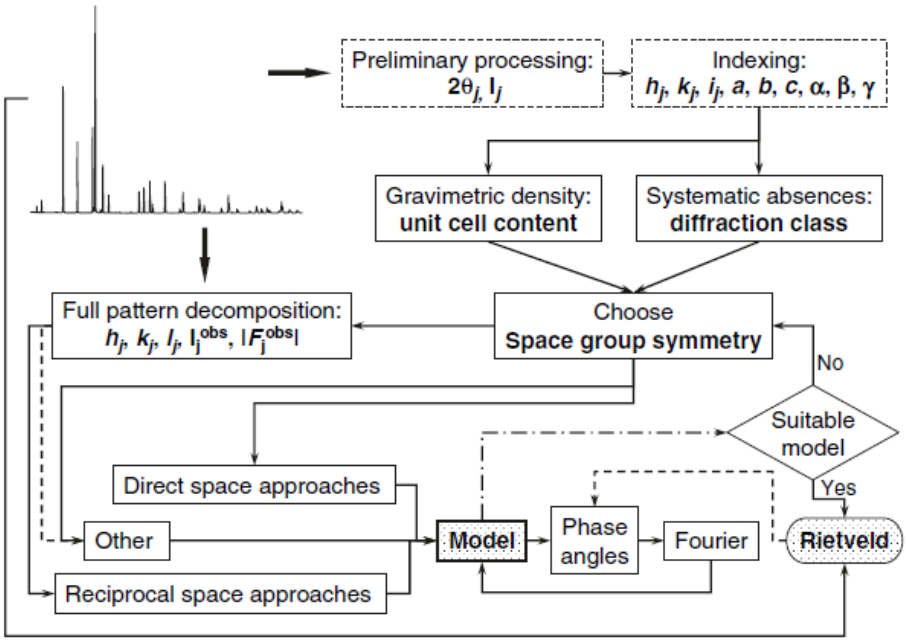

Figure 4-7 Flowchart illustrating crystal structure determination from PD data. [adapted from ref. [138]]

operations, schematically reported in Figure 4-7, I want to discuss more about how to face these steps, explicitly underline some peculiar aspects specifically related to my HP/HT samples.

1) *Peak search*

Firstly, it is necessary to carefully determine the peak 2theta-position of each reflection. Despite this process would seem quite easy, also using peak-hunting software, this is not often the case for HP/HT samples, due to the usual presence of undesired spurious phases and to pretty complex and in some cases dense set of crystallographic reflections. As a result, generally, the powder diffraction pattern includes the contribution of all the involved phases. The discrimination between the wanted and the unwanted phases is tricky since many spurious phases produced by the effects of HP/HT are not indexed in the majority of the crystallographic databases. Typically, a manual peak selection is thus more suitable for HP/HT new phases, paying particular attention to low-intensity peaks that can be addressed or not to the main expected crystal phase by considering possible kinds of impurities. Moreover, due to the low crystallinity of HP/HT samples, the diffraction peaks are usually quite broad in 2θ, making the exact estimation of the angular position

challenging. After this process, all the chosen reflections will be associated with a 2θ-position, corresponding to specific d-spacing values.

2) *Peak indexing*

Subsequently, all the reflections must be indexed with a triad of Miller indices (hkl). Namely, the indexing step enables to reconstruct the unit cell (i.e. all the lattice parameters a, b, c, α, β, γ) by the information on the d-spacing values extracted from the experimental 1D pattern. Many software allow the automatic solution for the indexing with several mathematical algorithms, by consequently returning candidates for the cell parameters. If more than one solution is proposed by the software, all the cell parameters combinations suggested are ranked according to the relative figure of merit, a marker of their reliability. Luckily, working with perovskite structures, the cell parameter of my HP/HT compounds should be approximately multiple of the simple cubic perovskite lattice parameter a_{sp}, unless structural distortions are present (see Chapter 2).

3) *Space group determination*

One of the most complex steps consists of the space group determination. Indeed, the diffraction pattern from a powdered sample suffers from peak overlap information due to the projection into the 1D space. Consequently, the evaluation of systematic extinctions, whose mathematical conditions are peculiar for each space group symmetry, is not obvious. By considering all the indexed peaks and providing information about the expected unit cell content, it is possible to manually evaluate the presence/absence of reflections by using the crystallographic tables [140], where all the space groups are listed for each crystallographic system with the relative reflection conditions on the h, k, and l indexes. To skip this time-consuming procedure, some software can be used to calculate the probability of each extinction symbol that could be compatible with the suggested crystal system. Generally, Le Bail [141] or Pawley [142] algorithms are used in this step, providing the fitting of individual reflection with the so-called full

pattern decomposition (or deconvolution), based on the non-linear least squares minimization of the differences between observed and calculated profiles. Again, particular care must be reserved for complex samples like those from HP/HT syntheses, because of the problems related to the hunting and indexing. However, good starting space groups to be tested should be those of similar perovskite compounds.

4) *Crystallographic model*

By combining all the crystallographic information previously extracted, a model for the crystal structure is created by using direct (as trial-and-error methods) or reciprocal space (as Patterson techniques) approaches, or a mixture of them. During this step, a fundamental support is again given by the information reported on the crystallographic tables [140], in which, for each space group, special symmetry positions (i.e. Wyckoff positions) are listed as preferential sites which can be occupied by the atomic species, considering the multiplicity of each site. In this way, a solution for the crystal structure is proposed, considering the pattern deconvolution with the structure factors for each atom included in the unit cell volume.

5) *Profile fitting structure refinement*

At the final step, several structural and profile parameters (i.e. atomic position, site occupancy, thermal parameters, etc.) must be refined in order to achieve the best agreement between the calculated and observed patterns, by improving the diffraction peaks fitting. Additionally, the chemical and physical information included in the structure solution, such as the interatomic distances or the coordination polyhedra, must be reasonable and consistent. Rietveld refinement [143] is the most widespread method to validate and improve the structural model, based, as Le Bail, on nonlinear least squares minimization. The quality of the refinement is quantified by several calculated parameters such as profile residual R_p, weighted profile residual R_{wp}, Bragg residual R_B, expected residual R_{exp}, and goodness of fit χ^2, which are of course affected by the initial quality of the acquired data.

The described procedure for nuclear structure resolution can be extended to determine the magnetic structure and symmetry of ordered-magnetic materials, as many HP/HT perovskites. As a good starting point, all the knowledge gathered about the crystalline space would be necessary, in order to index and evaluate the magnetic diffraction peaks. However, the magnetic structure (cell and symmetry) can significantly differ from the nuclear one. The relation between the two structures is expressed by the propagation vector $\vec{k}$. Sometimes more than one propagation vector is required to describe the magnetic-nuclear structure relation. If the components of k are rational, then the magnetic structure is commensurate, as for FM or AFM systems, while for irrational k components the structure is incommensurate, typically displaying helical, sinusoidal, or conical spin arrangements. The solution for the magnetic space group, all listed in the magnetic group tables [144] requires the knowledge of with magnetic species of the unit cell that contributes to each type of magnetism and the time inversion symmetry. Conventionally, the magnetic symmetry solution can be performed by deriving all the spin transformations on the basis of irreducible representation group theory, available via several data analysing software, such as FullProf [145].

As deducible, the structure determination and solution, especially from powder diffraction, is thus quite difficult and not immediate, so combining different probes is helpful. In this process, I have employed many software, particularly I have spent many hours (rather than days) on *Expo14* [146] (steps 1-2 and attempts for 3-4), *PowderCell* [147] (for manual steps 3-4), *GSAS-II* [148] and *Jana2020* [149] (steps 4-5). From my experience, sometimes it is more fruitful to sleep and come back a few days later with another solution attempt, tuning in to the unit cell.

4.5 Transmission Electron Microscopy

Transmission Electron Microscopy (TEM) is a very powerful instrument because of its large versatility for the investigation of electron transparent specimens, like nanometric powder samples or properly designed thin films [150], also from the crystallographic point of view. Particularly, it can provide important

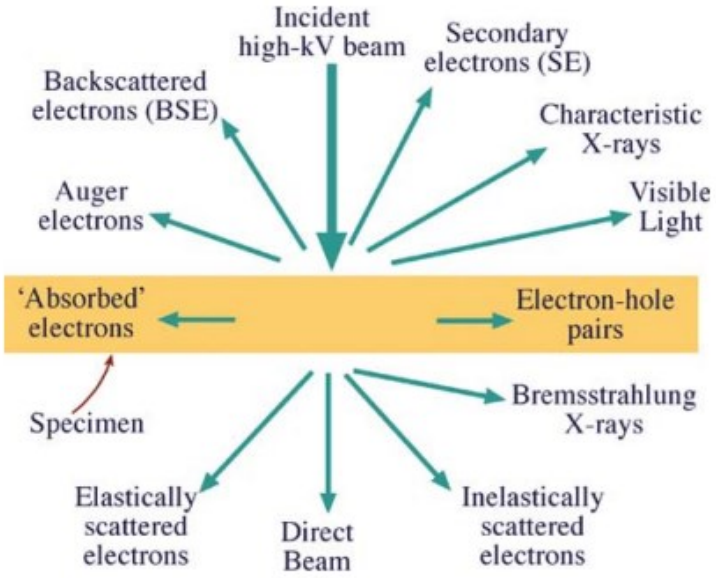

Figure 4-8 Signals generated from the electron-specimen interaction. [adapted from ref. [150]]

information when the samples are not perfect from a crystallographic point of view, as in the case of my HP/HT perovskites.

Although the TEM results related to my perovskites have been performed on a Philips TECNAI F20 TEM at the CNR-IMM UOS (Bologna, Italy), I personally practised for the entire first year of my PhD activity with JEOL JEM-2200FS TEM, having the chance to work in contact with the Structural Characterization research group of IMEM-CNR (Parma). In this standard, the probe is constituted by a high-energy electron beam generated by a Schottky field-emission tungsten gun and subsequently accelerated reaching the working voltage of 200 kV (or 80 kV for more fragile samples). A complex system of sequential electromagnetic lenses, constituted by one or two polepieces of soft iron in which a coil of copper wires is inserted, can control the electronic beam focus, position, and magnification, by tuning their magnetic field induced through an electric current. The divergence or convergence of the beam is instead managed by apertures in the lenses. The whole TEM columnar apparatus is closed into a vacuum chamber, with a peculiar refrigeration system to prevent damages due to the several currents involved in the lenses system. The combination of lenses and aperture allows it to work in different modes by focusing the electronic beam on different planes, as in a more conventional optical microscope, and investigate the several generated signals with different kinds of detectors. Indeed, one of the advantages

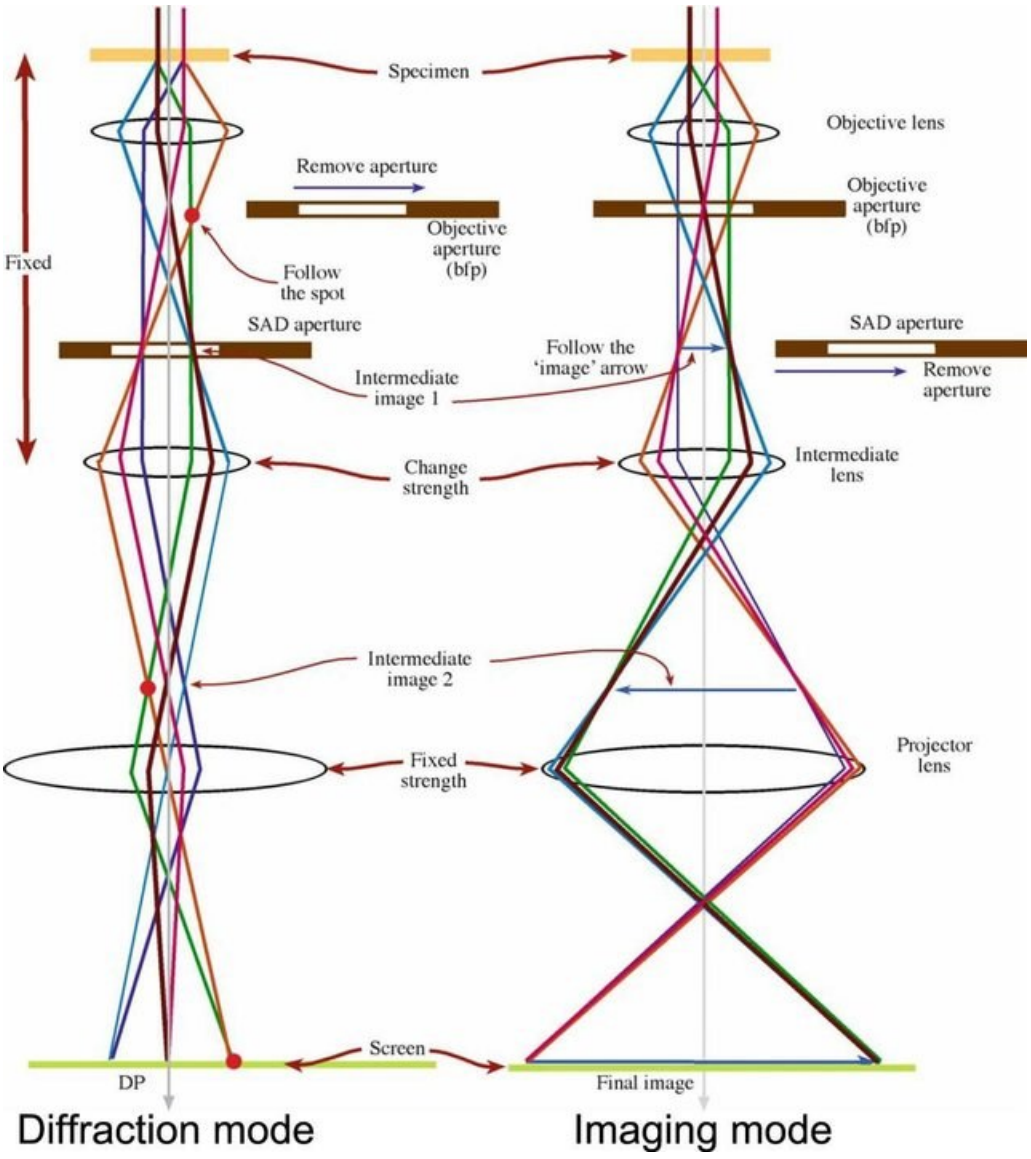

Figure 4-9 Simplified TEM scheme of lenses and apertures for the diffraction (left) or imaging (right) mode. [adapted from ref. [150]]

of using highly energetic electrons as ionizing radiation is the large number of secondary signals generated from the interaction process with the sample, as shown in Figure 4-8. Each of them constitutes a fingerprint of particular properties of the specimen.

Besides the morphological details that can be highlighted in the imaging modes of TEM, like with the scanning transmission electron microscopy (STEM) or the extremely powerful high-resolution TEM (HRTEM), essential to determine atoms' position and observe structural defects highlighting details finer than 0.2 nm, also physical and chemical information of the specimen are revealed. For the latter case, quantitative analysis of the chemical elements, their valence states on confined

areas, or even their distribution on an extended area of the specimen, are provided by energy-dispersive X-rays spectroscopy (EDXS) and electron energy-loss spectroscopy (EELS). One of the most significant TEM modes, surely for my case studies, is the Selected-area electron diffraction (SAED), by which crystallographic information can be extracted.

As previously mentioned, the lenses and apertures system allow to switch between different TEM operation modes. Particularly, in order to bring to light the inner diffraction pattern (DP) of the sample, with SAED, or its related image two basic configurations of lenses/apertures are required, by moving these elements as shown with a simplified scheme in Figure 4-9. The main role is given by the intermediate lens, which can select, by changing its strength, its object between the back focal plane and the image plane of the objective lens. Satisfying one of these two conditions, the DP or the image of the specimen, respectively, is projected at the CCD camera. In order to acquire good DP or images, the finest alignment of the whole elements (many more imaging lenses, for improving magnification and focus range, are present in real TEM respect with to the schemes of Figure 4-9) and the corrections from spherical aberration, chromatic aberration, and astigmatism, intrinsic defects of all standard lenses, is mandatory. This process constitutes a quite time-consuming step for TEM users, although a lot of work has been done in recent years in order to automatize this process by using machine learning methods [151] [152].

In the SAED mode, specifically for small particles investigation, electron diffraction occurs by illuminating with the accelerated electrons beam a portion of the crystallite, and it can be described in the context of Fraunhofer diffraction. Additionally, thanks to the wave-particle duality, the electron wavelength is around 2.5 pm (considering an accelerating voltage of 200 kV), thus able to probe interatomic distances in the crystal lattice, which acts as a diffraction grating. Particularly, the geometrical construction of the Ewald sphere, which represents the Laue condition, can be considered flat in the case of electron diffraction, as its radius is inversely proportional to λ, and many more points of the reciprocal lattice can be intersected. This is why the DP in TEM consists of many spots- when the sample is oriented along a high-symmetry axis -as a result a two-dimensional

section of the reciprocal crystal lattice perpendicular to the direction of the incident electrons. Consequently, the DP can be very useful to extract lattice constants, by evaluating the relative angles and distances between crystallographic planes (i.e. between the bright spots). In this analysis, it is fundamental to refer the acquired DP to a specific zone axis [u k w], which corresponds to the direction lying in all the planes visible in the DP (i.e. parallel to the beam).

Indeed, I have specifically employed SAED-TEM as an additional technique for the evaluation of crystal lattice parameters of my HP/HT perovskites, besides also morphological and quantitative measurements have been carried out in HRTEM and EDXS modes. The sample preparation for such measurements consists of depositing a few drops of a nano- or micrometric powder of the ground sample, suspended in isopropyl alcohol and sonicated for several hours, on a standard copper or gold mesh grid of diameter around 3 mm, coated with a plastic layer of formvar and a thin film of amorphous carbon, that is then mounted on a customised sample holder. The analysis of DP patterns has been carried out with diffraction packages on the software *Gatan Digital Micrograph* [153].

4.6 Morphology, magnetism, and electrical properties

Further investigations of the physical/chemical properties of the HP/HT novel perovskites have been carried out. Since the behaviour of such compounds is not known in advance, the choice of each characterization technique has been made in progress, by considering previous results, always starting from the structural investigations extensively described before. Herein, I will briefly summarize all the methods employed in the study of my compounds.

- *Scanning Electron Microscopy* (SEM) has been employed to investigate the morphology and composition of the samples, both in polycrystalline bulk and powder form. Two analogous instruments have been used. The first one, available at IMEM-CNR Institute of Parma, is a Zeiss Auriga Compact Field-Emission SEM equipped with an Oxford Xplore 30 Energy Dispersive Spectroscopy (EDS) system. SEM images were acquired by using 20 kV acceleration voltage of the primary electron beam. EDS analyses were conducted by exciting the powdered samples

with a 20 kV accelerated electron beam. The second microscope, available at the Chemistry Department of University of Parma, is the ESEM Quanta 250 FEG by FEI part of Thermo Fischer Scientific, with relative EDS system by Bruker XFlash 6/30 and Esprit 1.9 software.

- *Magnetic measurements* were performed with a Quantum Design MPMS 3 SQUID magnetometer located at the material characterization laboratory at the ISIS facility (UK) in the 2-400K temperature range. A small fragment of the sample pellet (m=36.87(5) mg) was used for the measurements. The sample holder was a plastic straw, and the pellet was kept in a gelatine capsule and fixed in place using Teflon tape. DC ZFC (zero-field cooling), FCC (field cooling), and FCW (field cooling-warming), measurements were performed with selected applied field values in the range 0.001-1 T. Magnetization versus field measurements were performed with the same sample set up at different temperatures in the field range ±5 T. AC measurements were performed at selected frequencies and amplitude of 1Oe. Further AC magnetization measurements have been performed in a Quantum Design Physical Property Measurement System-9 (PPMS) in the 10-350K temperature range at fixed frequencies of 1 and 10kHz and various field amplitudes in the range 1 to 10 Oe. In order to complete some missing characterizations, especially for powdered samples, additional magnetization measurements have been carried out on a Quantum Design MPMS-XL 5 T SQUID magnetometer in DC mode (at the Physics Department, University of Parma (IT)), investigating the magnetic field-dependence of the magnetization from 6 up to −6 T after a field cooling in low magnetic field.

- *Solid-state Nuclear Magnetic Resonance (NMR) spectroscopy* has been extensively used to detect local magnetic order and to clarify the electronic configuration of the NMR active species, specifically ^{55}Mn. In ZF ^{55}Mn NMR, it is possible to follow as a function of temperature the NMR signal of the ^{55}Mn nucleus, that resonates in a hyperfine field proportional to the thermal average of its electronic moment. The experiments, both in ZF mode or by applying a perturbative external magnetic field (up to 2 T), were performed by means of a home-built phase-coherent spectrometer, the 'HyReSpect' [154], at Physics Department, University of Parma. It allows T-dependent measurements thanks to a heater for

temperatures higher than RT. For low T, a helium flow allows to cover the thermal range of 2–70 K, while a nitrogen-flow cryostat has been used above 70 K. Powdered samples of about 20 mg were placed in an untuned probe-head consisting of a small coil, as described in ref. [155]. The spectra were recorded point by point by exciting spin echoes at discrete frequencies by means of a standard P–τ–P pulse sequence. The digitized echo signals were analysed by the fast Fourier transform (FFT).

- *Electrical transport measurements* were performed at IMEM-CNR using a Keithley 2182A nanovoltmeter and a Keithley 2400 sourcemeter. The measured sample was an as-synthesized pellet disk (with radius around r=2 mm, thinned down to thickness around t=0.3 mm), double-side polished to reduce the surface roughness below a few μm. Two different configurations have been employed for resistivity measurements: two-contact and van der Pauw four-contacts. In the two-contact configuration, platinum contacts (thickness ~100 nm) have been sputtered on both faces of a planar-plate disk, and resistivity was calculated by the Ohm's law. In the four-contact configuration, four silver paste contacts have been deposited manually on one disk side and van der Pauw technique has been applied with an injected DC current of 2 mA, measuring all the permutations of contact pairs and current polarity in order to cancel possible instrumental bias.

- *Dielectric measurements* have been carried out on the same metallized samples prepared for the above mentioned two-contacts resistivity measurements. In this case, an Agilent 4824A LCR meter has been used to measure impedance in four-contacts configuration. A frequency of 1 MHz has been selected with a signal amplitude of 100 mV.

- *Magnetoresistance measurements* have been carried out by exploiting the magnet and the cryostat of a commercial Quantum Design superconducting quantum interference device (SQUID) magnetometer at IMEM-CNR (IT). The bulk sample was brought to a selected temperature condition applying both ZFC and FC protocols starting from RT, the latter in an applied field of ±40 kOe. Once the set-point temperature had been reached, the electrical resistance was measured as a function of the external magnetic field spanning from –40 kOe to +40 kOe.

5 Experimental results and discussion

5.1 My novel perovskites: the starting idea

As extensively discussed in Chapter 2, single ($AB'_{0.5}B''_{0.5}O_3$) or double perovskites ($A_2B'B''O_6$) display a wide tolerance to chemical substitutions and structural distortions, induced by the broad range of their possible tolerance factors. In this context, the high pressure/high temperature synthesis techniques represent a useful tool to stabilize metastable phases at ambient conditions, amplifying the ensemble of possible cationic combinations. In particular, it has been shown that is possible to explore the versatility of such perovskites by playing with the chemistry of this crystal structure, with the potential lowering of crystallographic symmetries by introducing different ions on the A and the B sites. These substitutions lead to the occurrence and tuning of many different functionalities, eventually the superposition of multiple ferroic orders, thus multiferroism. The coexistence of usually competing phenomena, like magnetism and ferroelectricity, in a single crystalline phase is quite difficult to obtain [156], but distortion mechanisms which occur in perovskites (described in Paragraph 2.3) could be helpful to merge these functionalities.

My experimental research activity starts here. Indeed, I have considered already known families of perovskites, extensively characterized in literature, with physical properties, displaying intriguing magnetic, electrical or even multiferroic behaviours. Specifically, I have considered already studied systems of Bi-based or Pb-based perovskites, in which the ferroelectricity is mostly associated with the stereochemical effect of such cations (see Paragraph 2.3.1). The aim of my work has been to tune their physical properties by trying partial or complete chemical substitutions on the A or B site of their perovskite structure. Considerable work has

been done in order to find the right synthesis conditions for high-purity level compounds, a mandatory step before any physical properties' characterization.

The first compound that I have synthesized in pure phase is the novel $BiCu_{0.5}Mn_{0.5}O_3$ perovskite. I have studied its synthesis stability diagram, structural, magnetic, and electrical properties, thus covering a quite complete spectrum of characterizations. Moreover, I have already explored the $BiCu_{1-x}Mn_xO_3$ solid-solution with different synthesis attempts by varying the stoichiometry ratio between copper and manganese. Despite the optimal synthesis conditions having not yet been found, preventing high-purity perovskite samples preparation, preliminary results have verified that playing with the Cu/Mn amount increases the tunability of, at least, the magnetic properties.

Secondly, I have focused my attention on Pb_2FeMoO_6 double perovskite, already known in the literature, extending its characterization by deeply investigating its magnetoelectric behaviour in relation to the cationic order at the B site. Starting from this Pb-based perovskite, I have tried to tune its electric/dielectric properties by the partial substitution of lead cation at the A site with potassium, ending with the successful synthesis of the novel $KPbFeMoO_6$. As you will see, further investigations are needed to fully characterize this compound, but I think that the obtained results constitute a quite good starting point for future related research.

The following paragraphs deal with all the results and discussion about these compounds.

5.2 $BiCu_{0.5}Mn_{0.5}O_3$ (BCMO)

Bi-based double perovskites ($Bi_2B'B''O_6$) constitute a large group of studied systems showing exotic properties. Specifically, the insertion of Bi^{3+} ion on the A site, owing to its stereochemical effect, can induce local distortions/lone pairs, and in some cases promote the formation of a net electric dipole in the structure [31] [157], as reported for instance in $BiCr_{0.95}Fe_{0.05}O_3$ [158]. On the contrary, the B' or B'' sites are usually occupied by different transition metals with an incomplete

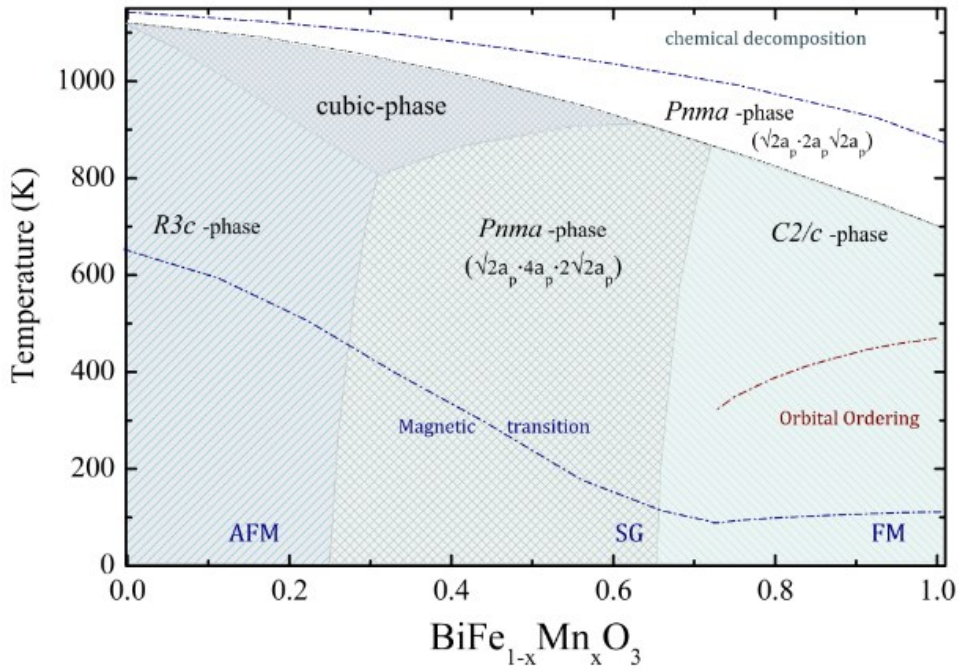

Figure 5-1 Structural and magnetic phase diagram of the solid solution $BiMnO_3$-$BiFeO_3$ depending on temperature and chemical composition. [adapted from ref. [159]]

d-shell (belonging to the III, IV, or V period) giving rise to various exchange interaction mechanisms, thus inducing different types of magnetic orderings in according to Goodenough-Kanamori-Anderson (GKA) rules for super-exchange coupling (see Paragraph 2.5). A great example of this magnetic properties interplay is constituted by the highly distorted double perovskite Bi_2NiMnO_6, in which Ni^{2+} and Mn^{4+} ions are ordered in a rock-salt configuration and the Ni^{2+}-O-Mn^{4+}-O-Ni^{2+} magnetic path leads to a ferromagnetism with Tc=140 K [126]. In this way, by properly tailoring the ions on both B' and B'' sites, it is possible to merge and control multiple functionalities, opening a wide variety of new applications, like in spintronic or energy storage devices. However, the potential effective use of many promising multifunctional perovskites is significantly limited by the low ordering thermal threshold of coexistence of a functional state.

$BiFe_{1-x}Mn_xO_3$ solid-solution represents a double perovskite family displaying many different and tuneable properties by varying the stoichiometry ratio between Fe and Mn [159]. Namely, the endmember with iron, $BiFeO_3$, is the most studied multiferroic perovskite, with several intriguing properties [160] [161] [162] [163]. This compound crystallizes in a rhombohedral non-centrosymmetric R3c space symmetry, and it shows both magnetic and ferroelectric long-range order well above room temperature. Specifically, the system undergoes a transition to a

polar state close to 1100 K and becomes antiferromagnetic, with a G-type spin configuration and a superimposed incommensurate cycloid spin structure, in a reported range between 595 K and 650 K. On the other hand, $BiMnO_3$ displays a ferromagnetic state with an ordering temperature of around 100 K. A ferroelectric behaviour has been observed in some thin films, but this effect in bulk form is forbidden by the centrosymmetric space group C2/c. Further studies pointed out a possible relationship between the oxygen content, with possible space group modification, and consequently a change of the properties of such perovskite. However, the presence of ferroelectricity is still debated [29] [134] [164]. Instead, the x=0.5 member, $BiFe_{0.5}Mn_{0.5}O_3$ crystallizes in an orthorhombic structure, described with Pnam space group symmetry and characterized by a high octahedral distortion and tilting, which lead to an antiferroelectric arrangement. Although the system does not usually exhibit cationic ordering at the B site, the magnetic properties are linked to inhomogeneity in the concentration of Mn or Fe ions, which determines clusters highly rich in one of the two species, with different magnetic arrangements and critical temperatures. Particularly, it displays a weak ferromagnetic state at 420 K ascribable to a second-order mechanism allowed by the low symmetry of the system and producing spin canting [66], while the main magnetic transition is described with a G-type AFM structure with T_N=288 K. Additionally, this mixed Fe/Mn system, similarly to the solid-solution members with x=0.3 or x=0.4, displays magnetization reversal phenomena at lower temperatures and poling induced ferroelectricity [66] [165] [166] [167] [168].

Starting from $BiFe_{0.5}Mn_{0.5}O_3$ (BFMO), I will present, for the first time to the best of my knowledge, the effective synthesis of a novel compound, specifically $BiCu_{0.5}Mn_{0.5}O_3$ (BCMO), characterized by the successful substitution of Fe^{3+} ion with Cu^{2+} ion at the B' site of the already studied perovskite BFMO. Indeed, the choice of Cu^{2+} is not accidental and requires some argumentation by comparing BFMO and BCMO systems.

Specifically, it is not surprising that all the strong competing super exchange interactions between Fe^{3+} (d^5) and Mn^{3+} (d^4) (i.e Fe-O-Mn, Fe-O-Fe, and Mn-O-Mn), both in an approximately half-filled d-shell configuration, lead to complex AFM in BFMO, coherently with the previously reported GKA rules to predict the

	BCMO	BFMO
Tolerance factor t	0.8360	0.8464
Octahedral factor μ	0.4500	0.4321

Table 5-1 Calculated tolerance and octahedra factors for BCMO and BFMO perovskites.

magnetism occurring between two magnetic species in perovskite systems. Noteworthy, standing to GKA rules for the 180° interaction between cations in octahedral site, the ion Cu^{2+} has a d^9 configuration, thus an almost complete shell which can, in principle, be helpful in the formation of a FM state by interacting with the Mn^{4+} cation in d^3 configuration of BCMO perovskite. In this way, the insertion of copper ion instead of iron should promote the ferromagnetism of BFMO, by enhancing this ordered magnetic state with a spontaneous magnetization at room temperature, an essential feature for technological perspectives, while hopefully retaining its ferroelectric behaviour.

However, as carefully remarked in Paragraph 2.2, the perovskite system must fulfil geometrical constraints, such as the tolerance factor or the octahedral factor, in order to ensure structural stability. By comparing the two considered ions in six-fold coordination at the B' site of the perovskite, Cu^{2+} is characterized by a tabulated ionic radius of 0.73 Å, while Fe^{3+} ionic radius value slightly varies between 0.55 Å and 0.645 Å, depending on its low or high spin configuration, respectively [169]. The values tolerance factor t and octahedral factor μ for BCMO and BFMO are reported in Table 5-1. The reported values have been calculated by evaluating the Shannon tables of ionic radii for all the species involved (also Bi, Mn^{4+} or Mn^{3+}, and O) by Shannon [169], with a mean value for r_B by taking into account the chemical substitutions at B' and B'' sites and, eventually, a mean value of the ionic radii depending on the possible low/high spin configurations. As noticeable, the calculated values for t and μ are quite similar in the two considered perovskites and consistent with the estimated stability ranges reported in Paragraph 2.2. From this consideration, a similar crystal symmetry and an orthorhombic unit cell should be in principle predictable also for the BCMO perovskite. Moreover, since the oxidation state of Cu^{2+} is lower respect with Fe^{3+} one, the insertion of

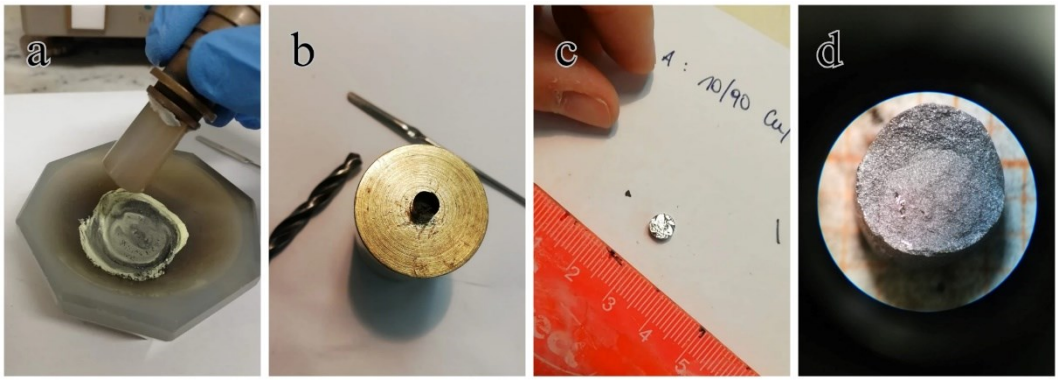

Figure 5-2 BCMO synthesis: reagents mixing (a), tools for the hand-made preparation (b) of the reagents' capsule (c) and the final sample at the optical microscope, on a graph paper as size reference (d).

copper cation inside the octahedral cavity of BCMO perovskite motif should require a slightly lower pressure compared to BFMO, which has been synthesized at 6 GPa [66].

In the following paragraph, I will discuss about the effective synthesis of this new compound, BCMO, whose stability and purity level have revealed a crucial and unconventional dependency on the synthesis conditions, particularly on the duration time of the solid-state reaction.

5.2.1 Synthesis conditions

The solid-state reactions for the synthesis of BCMO have been carried out in the Walker-type multi anvil press (see Paragraph 3.2). The starting powder of the binary oxides of each element, specifically Bi_2O_3 (99.999 %, Alfa Aesar Puratronic), CuO (99.99 %, Fluka), and MnO_2 (99.9 %, Alfa Aesar), has been mixed and ground together in agate mortar (Figure 5-2a). The resulting powder has been closed in a Pt thin foil capsule for the attempts with a temperature set-point higher than 1000°C, otherwise Au capsules have been preferred (Figure 5-2b,c). The cylindrical bulk polycrystalline sample of BCMO obtained in each synthesis, of weight around 600 mg, is pictured in Figure 5-2d observed with the optical microscope. Indeed, several pressure, thermal, and reaction time conditions have been explored, mainly between 3-5 GPa and 800-1000°C respectively, keeping these conditions for various duration times (from 10 minutes to 2 hours). All these attempts are reported in Table 5-2. The best synthesis conditions observed for BCMO solid-state reaction have been determined to be 4 GPa of pressure and 1000°C of temperature. The duration time of the synthesis plays a crucial role in

Pressure (GPa)	*Temperature (°C)*	*Reaction time (hours)*
3	650	2
3	900	2
3	975	2
3	1250	1.6
4	885	0.25
4	975	0.5
4	1000	0.2
4	**1000**	**0.5**
4	1000	0.75
4	1000	2
5	990	0.5
5	1000	0.25

Table 5-2 Tested BCMO synthesis conditions. The best conditions are highlighted in red.

obtaining a high purity level of this compound. Particularly, the purer sample has been obtained keeping the P and T conditions during the reaction for half an hour, and it seems that longer durations lead to the degradation of this metastable phase, contrarily to the conventional protocol in which longer reaction times should support the formation of bigger crystals. In Figure 5-3 different PXRD patterns of

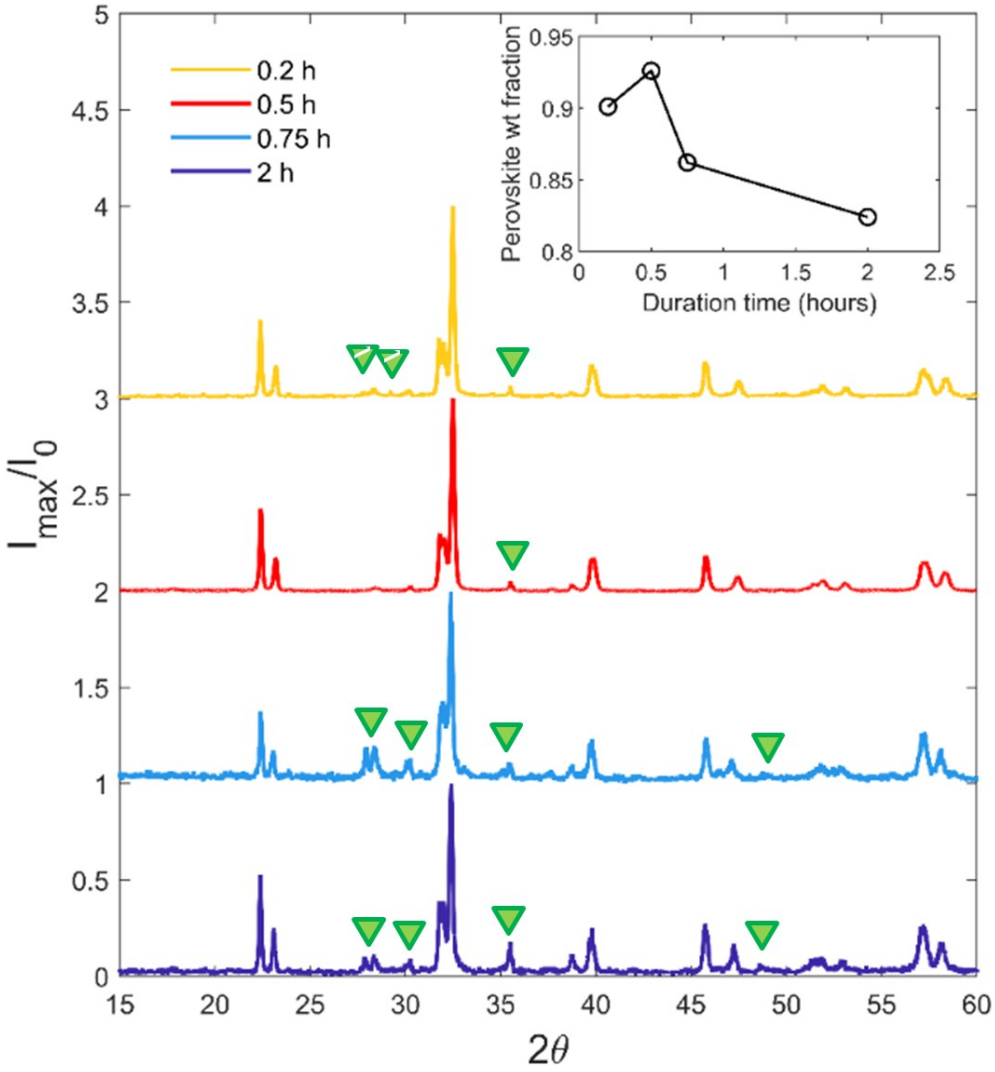

Figure 5-3 Normalized PXRD patterns for BCMO samples synthesized at 4 GPa, 1000°C, at various reaction times. Identified spurious phases are highlighted with green triangles. Inset: Estimated weight fraction of the perovskite phase in each sample from Rietveld refinement (despite high average R_{wp} ≈19).

ground BCMO samples synthesized with various reaction times (i.e. from 0.1 hours to 2 hours) at the same P-T synthesis conditions (4 GPa, 1000°C), are compared. In the normalized patterns, the reflections related to identified spurious phases (mainly copper and manganese oxide compounds) are labelled with green triangles, while the more intense peaks are associated with a desired perovskite phase. Despite the non-ideal signal-to-noise ratio of such spectra, a quantitative estimation for the weight fraction values of the perovskite phase has been evaluated by performing a Rietveld refinement of each dataset (considering the structural model of the purer BCMO that will be presented in the following paragraph). The results, reported in the inset of Figure 5-3, confirmed that the majority of the product mass is constituted by a perovskite phase with values close to 95 % for the sample

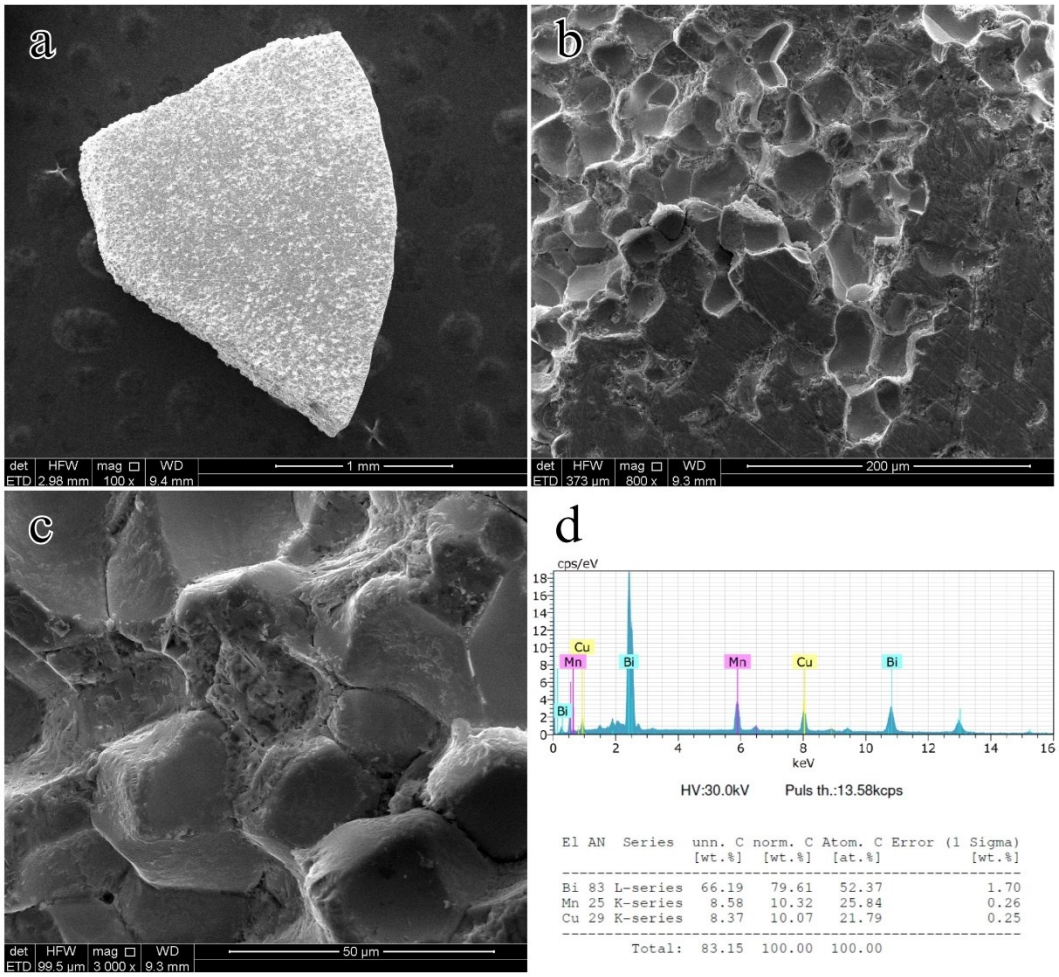

Figure 5-4 SEM images at various magnifications (a, b, c) and EDX microanalysis (d) on bulk BCMO.

synthesized with a reaction time of 0.5 hours. By varying the reaction time, spurious phases arise. Probably, for shorter durations, unwanted reaction intermediates are still present, while for durations longer than 0.5 hours, degradation effects of the perovskite system occur.

Considering this crucial aspect of the synthesis condition for BCMO, P-T conditions could be tuned in order to increase the reaction yield and obtain a purer sample. However, since performing each HP/HT synthesis requires a discrete amount of time, I did not explore further the stability diagram of BCMO. Indeed, a purity level of around 95 % is good enough to allow an effective characterization of the structural, magnetic, and electrical properties of the samples synthesized under the best synthesis conditions, i.e. at 4 GPa, 1000°C for 0.5 hours.

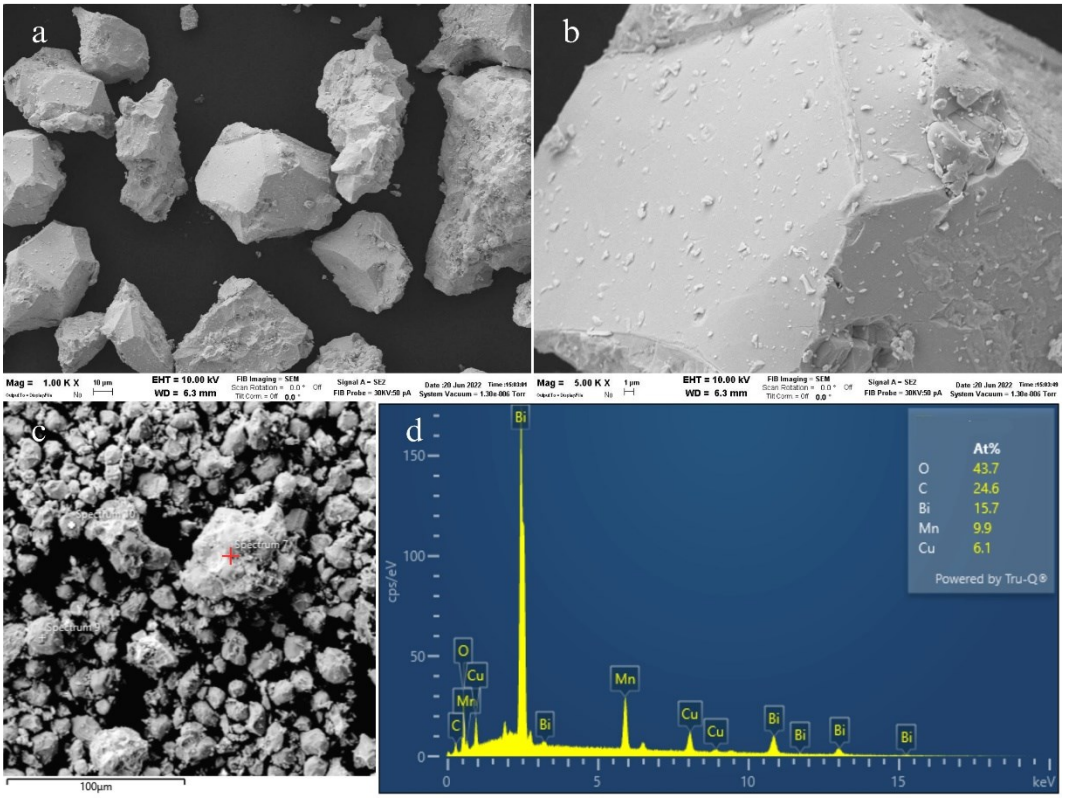

Figure 5-5 SEM images (a-b) and EDXS analysis with image (c) and spectrum (d) of a powder of BCMO.

5.2.2 Preliminary structural investigation and morphology

In order to investigate the morphology and the stoichiometry of the BCMO obtained via HP/HT synthesis, preliminary SEM investigations, in imaging and qualitative EDX analysis modes, have been conducted, both on bulk (Figure 5-4) and powdered samples (Figure 5-5). From the bulk analyses, the polycrystallinity of BCMO is clearly visible for different magnifications (Figure 5-4a, b, c), with small grains of size around 30 µm. By performing EDXS microanalysis on several grains, atomic percentages relative to the heavy elements contained in BCMO have been calculated from the spectra analysis, as reported in Figure 5-4d. The estimated stoichiometry ratio between Cu and Mn of around 0.84:1 slightly differs from the 1:1 expected, but it could be coherent with the presence of possible intra-grains inhomogeneities, where different and more rough morphologies seem to be present (Figure 5-4c), or more reasonably for the presence of CuO as spurious phase. The SEM analyses on the powdered samples are in agreement with those on the bulk, as reported in Figure 5-5. Quite big multi-faceted grains are visible (Figure 5-5a, b), while on the surface of the larger crystallites small sub-micrometric components are present, probably of the same nature as the intra-grains inhomogeneities

reported also for the bulk form (Figure 5-4c). Punctual EDX measurements pointed out a higher discrepancy between the calculated Cu/Mn stoichiometry ratio and the predicted one, confirming the hypothesis of impurities mainly attributed to copper compounds. The reported carbon content is due to the SEM vacuum-chamber contamination.

Subsequently, TEM analyses on BCMO powders have been performed and the related results are reported in Figure 5-6. Crystalline sub-micrometric grains are visible in STEM (Figure 5-6 a) and STEM-High-angle annular dark-field (Figure 5-6b) imaging modes. The single fragments contain more than one phase, detected as a high contrast displayed in specific zones inside a single grain, not attributed to different thicknesses of the sample. Coherently with SEM-EDXS analyses, impurities, again probably related to bismuth and/or copper oxide compounds, are thus present also at the micrometric level. Focusing on the homogeneous areas (Figure 5-6f), EDS microanalyses have been performed (Figure 5-6g), and the stoichiometry ratio of Bi:Cu:Mn has been verified to be in agreement with the one expected 2:1:1. Here, SAED patterns have been collected from different zone axes of small grains and reported in Figure 5-6c and d. All the observed spot reflections can be indexed with an orthorhombic cell with lattice parameters a = 5.58 Å, b = 11.23 Å, c = 7.66 Å. These values can be considered as a result of a distortion from the ideal simple cubic perovskite lattice parameter $a_{sp} \approx 3.8$ Å, particularly with $a \approx \sqrt{2}a_{sp}$, $b \approx 2\sqrt{2}a_{sp}$, $c \approx 2a_{sp}$. By performing the Fourier-transform of HRTEM image reported in Figure 5-6e, in which single atomic layers are clearly visible, a simulated electron diffraction pattern is obtained, which confirms the lattice parameters previously estimated via SAED.

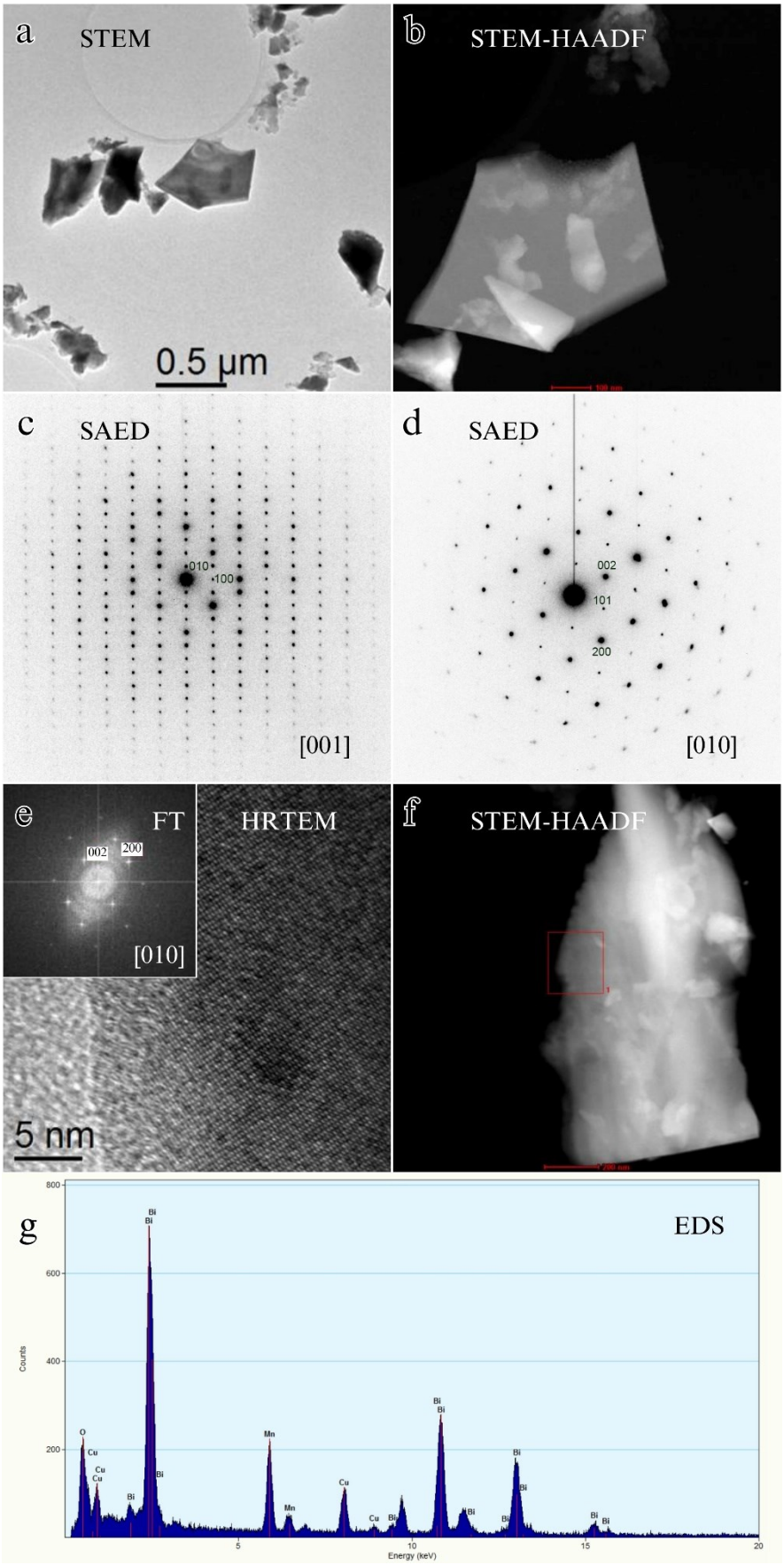

Figure 5-6 TEM analysis on BCMO in different modes: STEM (a), HAADF (b), SAED (c-d), HRTEM and relative FT (e), HAADF (f) and relative EDS (g).

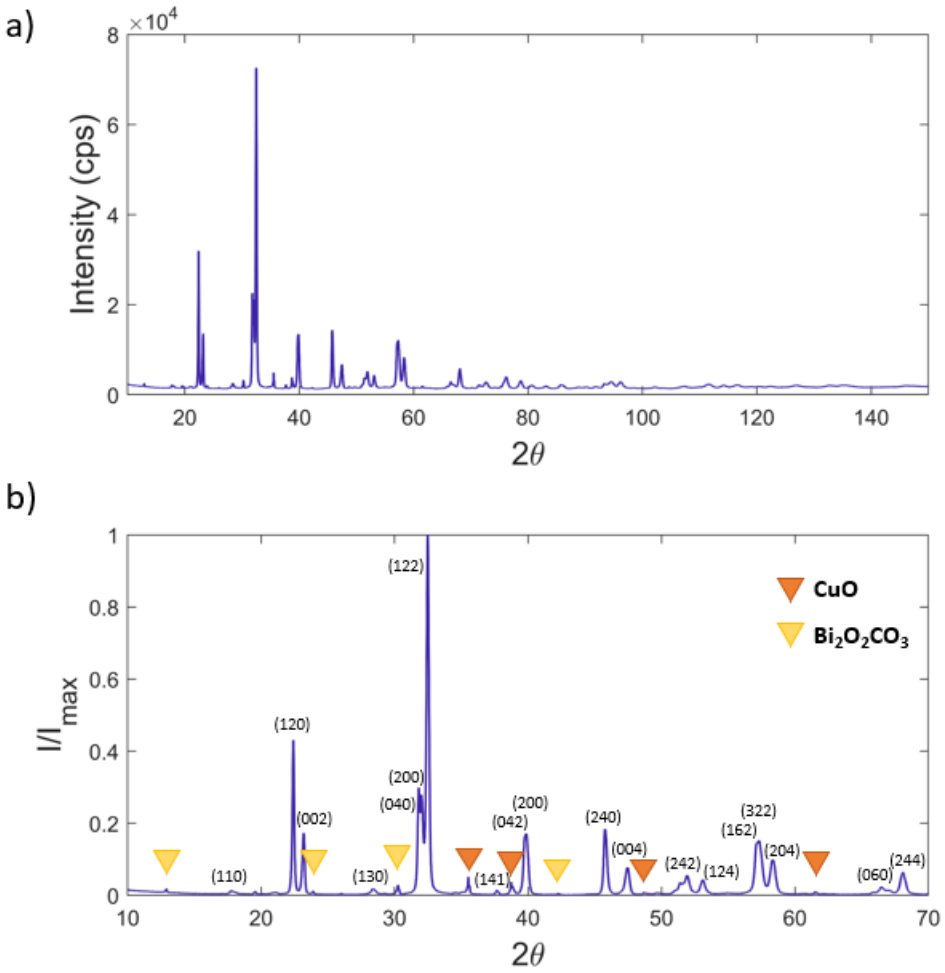

Figure 5-7 (a) Powder X-ray diffraction of BCMO. (b) Zoom on main indexed reflections, considering as spurious phases CuO and $Bi_2O_2CO_3$, whose intense reflections are marked with orange and yellow triangles, respectively.

5.2.3 Room temperature nuclear structural resolution

The first steps toward the structural resolution of BCMO have been carried out by performing PXRD. The diffraction pattern acquired at ambient conditions from 10° to 150° is reported in Figure 5-7a. The collected reflections are characterized by a quite large profile shape, with a FWHM of around 0.22° for the most intense reflection, a feature related to the polycrystalline defective nature of the sample, often observed in HP/HT samples. Considering the crystallographic information on the cell parameters obtained with SAED-TEM previously presented, I have analysed the diffraction patterns following the structure determination and refinement process schematically listed in Paragraph 4.4. Specifically, I have started my analysis by considering the simple cubic perovskite structure. By comparing its

reflections with those observed in BCMO diffraction pattern, I have been able to evaluate if, for instance, by doubling certain crystallographic lattice parameters, the visible diffraction peaks were better indexed. The cell parameters obtained from TEM-SAED were coherent with the superstructure reflections observed in the diffraction pattern. In principle, more than one space group is compatible with this proposed unit cell. To find a suitable starting model for the refinement perovskite compounds with similar unit cell parameters were considered. One of them is the $PbZrO_3$ perovskite, which crystallizes in an orthorhombic cell with a = 5.884(1), b = 11.787(3), and c = 8.231(2), and space group Pbam [170]. The latter space group is consistent with the systematic extinction rules and possible spurious phases observed in the diffraction pattern. Figure 5-7b shows the indexation of the powder pattern with the Pbam (n. 55) space group. As said before, this solution takes into account two main spurious phases, related to the bismuth carbonate oxide $Bi_2O_2CO_3$ (ICSD cod. 202767) and copper oxide CuO (ICSD cod. 16025), whose major peaks are marked in Figure 5-7b. The latter impurity derives directly from the incorrect stoichiometry of one reagent, while the former spurious phase could be present due to bismuth oxide reagent's contamination with carbon coming from the close graphite heater of the assembly, or a possible pre-existing contamination of the starting reagent. One very small reflection, at around 28° in the XRD pattern, has not been indexed by taking into account the results from crystallographic databases, but probably unknown mixed oxides can be found under these extreme conditions of HP/HT. However, the relative intensity with respect to the main peak of BCMO perovskite phase suggests that the impurities level is reasonably low, allowing a feasible refinement process.

A key aspect related to the structural refinement of perovskite systems is the fine determination of all the atomic positions, especially those of the oxygens, an essential feature to determine the octahedra distortions, which strongly affect the resulting physical properties of this class of compounds (see Paragraph 2.3.1). To highlight more the contribution of oxygens, hidden below the XRD signal of heavy elements of BCMO, neutron diffraction experiments at room temperature have been performed. The refinement of the previously built crystallographic file has been carried out with the Rietveld approach in Jana2020 considering both XRD and ND patterns. Figure 5-8 shows the Rietveld plot of the XRD and ND data, while the

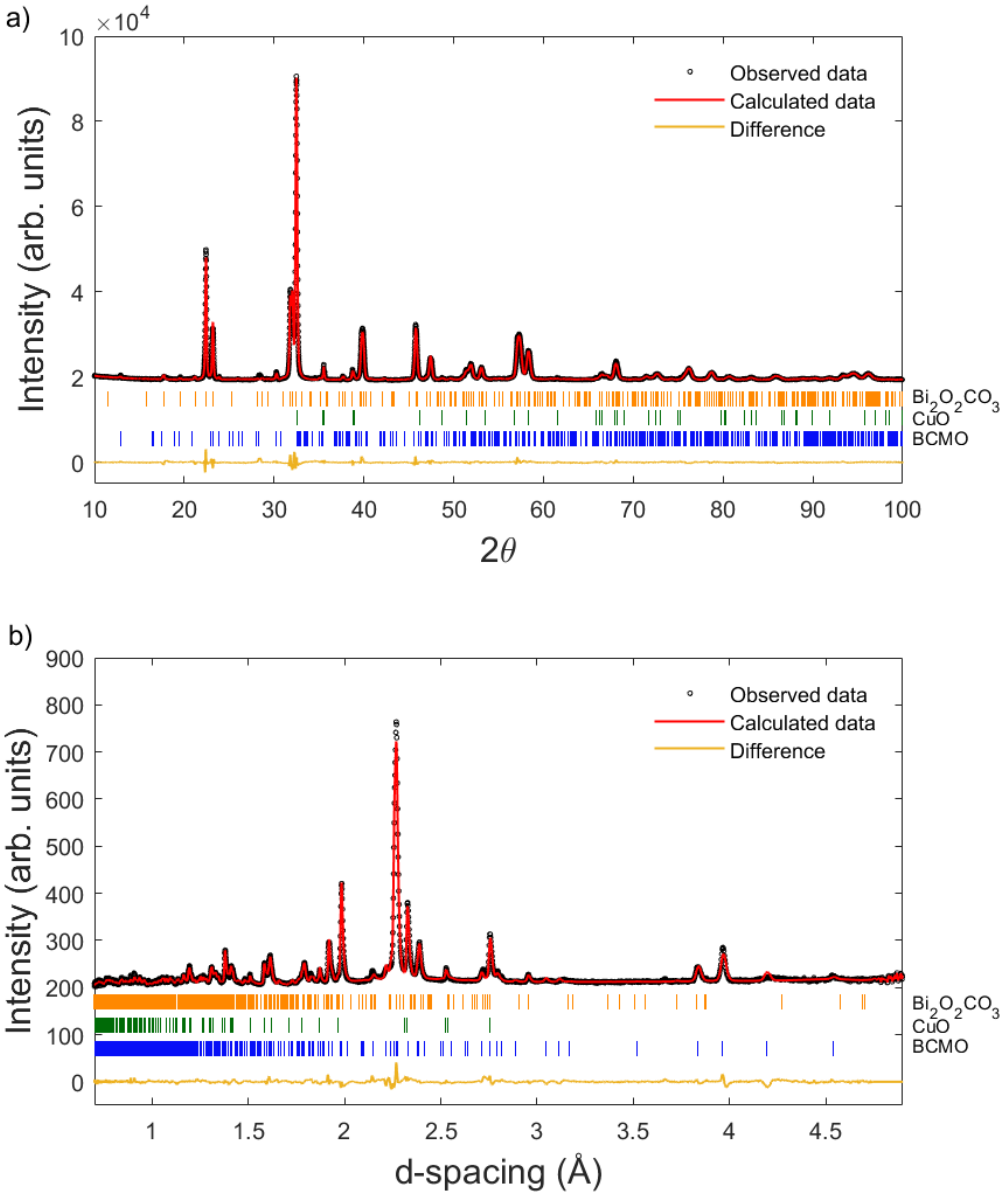

Figure 5-8 Rietveld refinement of BCMO nuclear structure from XRD (a) and ND (b). The Rwp=5.22. Rp=3.61 and GOF=2.42 values for XRD, while for ND are Rwp=5.14. Rp=3.81 and GOF=3.03.

obtained structural parameters for BCMO are reported in Table 5-3. Figure 5-9 shows the obtained crystal structure.

Comparing the lattice parameters of BCMO, refined to be a=5.5796(2) Å, b=11.2374(4) Å, c=7.6603(2) Å, with those of the parent compound BFMO, in the latter case the primitive cell is doubled along the c axis, with c≈4ap, with Pnam (62) as space group. Unfortunately, the presence of ferroelectricity is excluded by the centrosymmetric nature of the BCMO space group. The nuclear structure of BCMO possesses a Lead Zirconate-type distortion with the bismuth shifted along the 111

Atoms	x	y	z	Occ.	U_{iso}	Site
Bi_1	0.7487(3)	0.6194(2)	0	1	0.01870(18)	4g
Bi_2	0.7741(3)	0.6283(2)	0.5	1	0.01870(18)	4h
Mn	0.2317(7)	0.6325(5)	0.2482(13)	0.6162(14)	0.0077(6)	8i
Cu	0.2317(7)	0.6325(5)	0.2482(13)	0.3838(14)	0.0077(6)	8i
O_1	0	0.5	0.2005(12)	1	0.066(9)	4f
O_2	0	0	0.2131(14)	1	0.066(9)	4e
O_3	0.4352(7)	0.7594(3)	0.2904(8)	1	0.066(9)	8i
O_4	0.2386(14)	0.6683(9)	0	1	0.066(9)	4g
O_5	0.1805(11)	0.5897(6)	0.5	1	0.066(9)	4h

Table 5-3 Structure parameters for BCMO from Rietveld refinement analysis of both PXRD and ND data.

pseudocubic direction in an up-up-down-down fashion with a a-a-c^0 tilting in Glazer notation. From the Rietveld refinement, no cation ordering on the B site between manganese and copper has been observed, coherently with the selected space group in which only one independent B site is allowed. However, a notable deficiency of Cu has been pointed out (see Table 5-3), which is compatible with the detected CuO impurity. The octahedral arrangement of the oxygens surrounding the transition metals (TM) at the B sites is highly distorted, as shown in Figure 5-9. This feature is coherent with the presence of disorder at the B site. The purity level of the perovskite phase has been calculated from the refinement at around 94% of phase volume fraction, with an estimated content of the previously mentioned bismuth oxycarbonate and copper oxide impurities of about 1% and 5%, respectively.

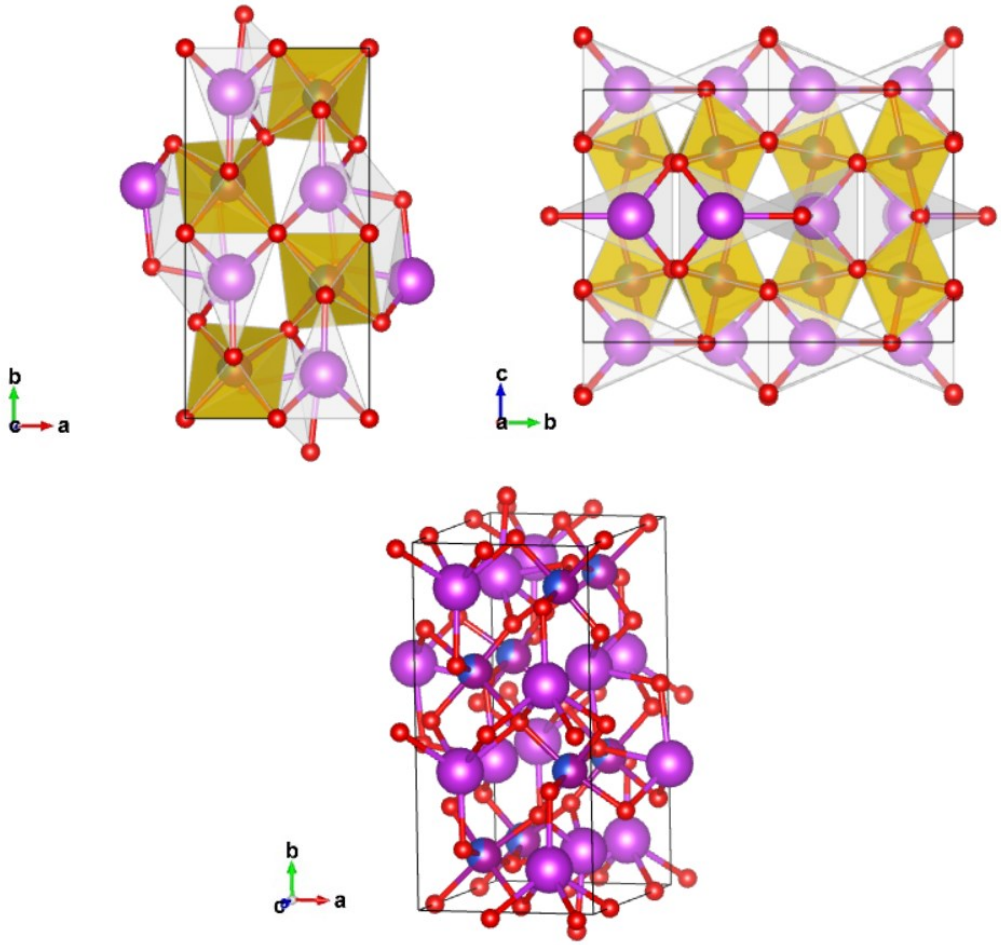

Figure 5-9 BCMO crystal unit cell from different crystallographic orientations.

To reduce the number of free parameters during the refinement process, some constraints have been considered. Specifically, the occupancy of both the bismuth and oxygen species have been fixed to 1, as the sum between the relative occupancy of the transition metals at the B site. Moreover, an isotropic thermal displacement U_{iso} has been considered for all the atomic species, and fixed to be identical for Bi, O and TM atoms respectively. The value for the R_{wp} parameter, around 5, confirms a reliable model obtained for BCMO.

5.2.4 Thermal stability of BCMO phase

The thermal stability of BCMO perovskite has been evaluated by performing PXRD measurements as a function of temperature, covering the whole temperature range between 85 K and 870 K. To optimize the measurement time, the 2θ-range explored for the measurement between 85 K and 300 K (cooling mode)

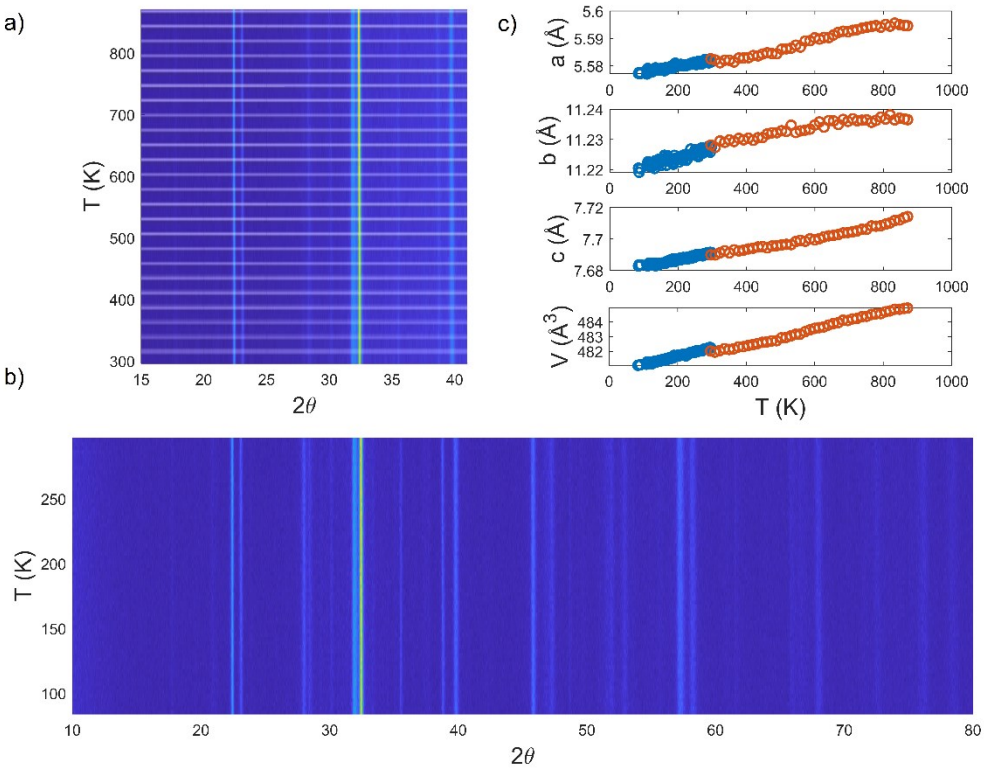

Figure 5-10 Waterfall plot of BCMO PXRD pattern collected in the high temperature (a) and in the low temperature (b) range. Lattice parameters' evolution with temperature in the low (blue) and high (red) temperature range. (c)

has been set to 10° to 80°, while for the 300 K-870 K range (heating mode) it has been reduced to 15°-41°. Based on the results shown in the "waterfall" plots of Figure 5-10a (heating) and Figure 5-10b (cooling), the BCMO PXRD reflection pattern does not display any significant changes in the explored temperature range. Consequently, it is possible to exclude the occurrence of nuclear phase transitions in this temperature range. This observation is also confirmed by the evolution of the lattice parameters reported in Figure 5-10c. However, it should be stressed that the cell parameters have been evaluated with a Rietveld refinement of the low statistic data, thus their estimated values are affected by a not negligible error bar. This is clearly visible in the small artefact gap of all the lattice parameters displayed at room temperature, due to the different set-up and sample holder employed in the two distinct thermal ranges. Despite improved temperature-dependent PXRD measurements could be performed to better evaluate the lattice constants, it is possible to state that BCMO perovskite phase is stable at least up to the maximum temperature set, a feature not so common for similar metastable compounds from HP/HT synthesis and extremely important for technological applications.

5.2.5 Magnetization

The magnetic properties of BCMO were investigated firstly by performing SQUID magnetometry measurements as a function of the temperature or the external DC magnetic field. In Figure 5-11 the ZFC-FC magnetization vs temperature curves are shown at 100 Oe (a), 1000 Oe (b), and 10000 Oe (c). Two magnetic transitions are visible in the explored thermal range, which vary their relative intensity with the magnitude of the magnetic field applied. Specifically, at high temperatures the system sharply switches from the paramagnetic state to an ordered magnetic state with an onset temperature of about 330 K (Figure 5-11a), which is completely overlapped with ZFC and FC, suggesting the ferromagnetic-like nature of such transition. As the temperature is decreased the compound undergoes a stabilization of the magnetic resultant below 250 K. At lower temperatures, below 100 K the magnetization starts to increase again with different trends for ZFC and FC, displaying around T_N=50 K the feature of an AFM cusp in ZFC mode, which is flattened during the FC protocol. This behaviour is typical of weak FM canting of AFM states, in which the domains can be oriented along the magnetic field applied in FC mode [171]. This AFM is an independent character with respect to the high-T ferromagnetic-like ordering. As the field is increased, two main features must be underlined: (1) the high-T ferromagnetic-like state is less visible respect with to the AFM one, underling the weak and/or local character of such magnetic order (Figure 5-11c); (2) the high polarizability of the AFM state as detected by the significant reduction of the fork between FC and ZFC, in which the domains are completely oriented with the H applied as it becomes greater than the coercive field (Figure 5-11b).

The characterization of the paramagnetic state was performed by analysing the Curie-Weiss plot reported in Figure 5-12, in which the inverse of susceptibility χ^{-1} has been calculated from SQUID M(T) data collected in ZFC mode with an applied magnetic field of 10 Oe. In the paramagnetic region, the plot returns a linear trend of the $1/\chi$ that has been modelled with the Curie law:

$$1/\chi(T) = (1/C) \cdot T + \theta_{CW}/C \quad (16)$$

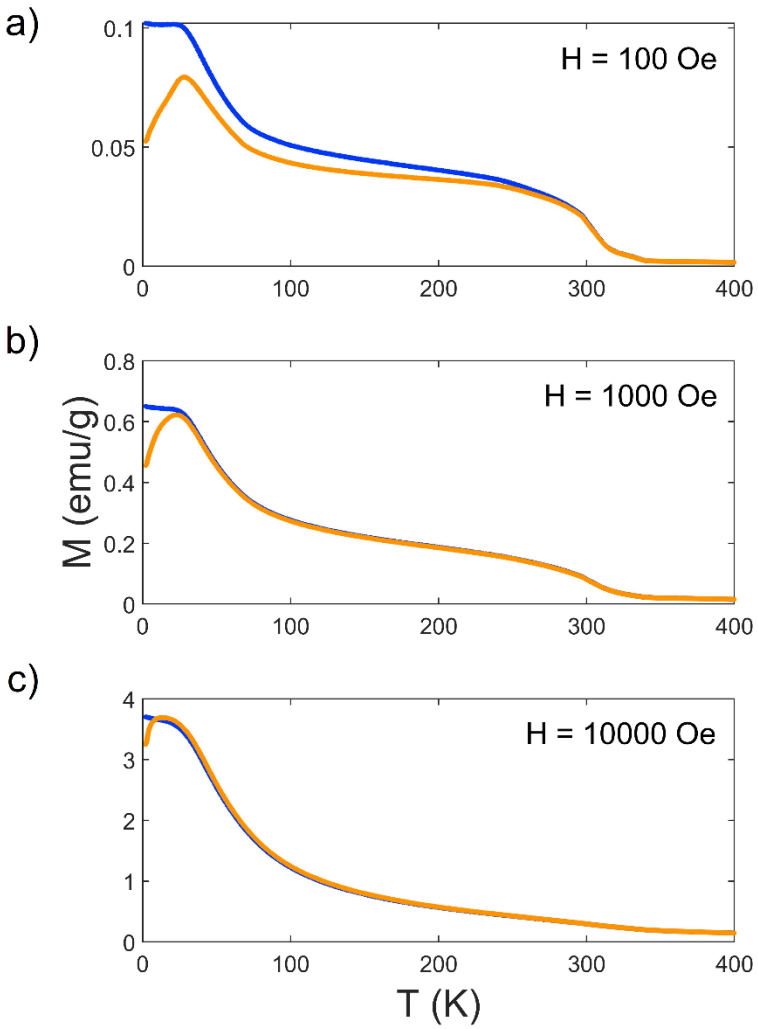

Figure 5-11 ZFC (orange) and FC (blue) magnetization of BCMO as a function of temperature measured at 100 Oe (a), 1000 Oe (b), and 10000 Oe (c).

where C and θ_{CW} are the Curie and the Weiss constant, respectively. From the linear regression, considering data collected at temperatures higher than 360 K, the parameters have been estimated to be C = (1.95±0.07)·10^{-3} emu·K/(g·Oe) and θ_{CW} = (260±10) K. The reliability of the linear fit is confirmed by the R^2 value equal to 0.9979.

The effective Bohr magnetons per formula unit value can be estimated considering the C constant previously obtained with the following equation:

$$\mu_{eff} = \sqrt{\frac{3000 \cdot k_B}{\mu_B^2 \cdot N_A} \cdot MW \cdot C} \qquad (17)$$

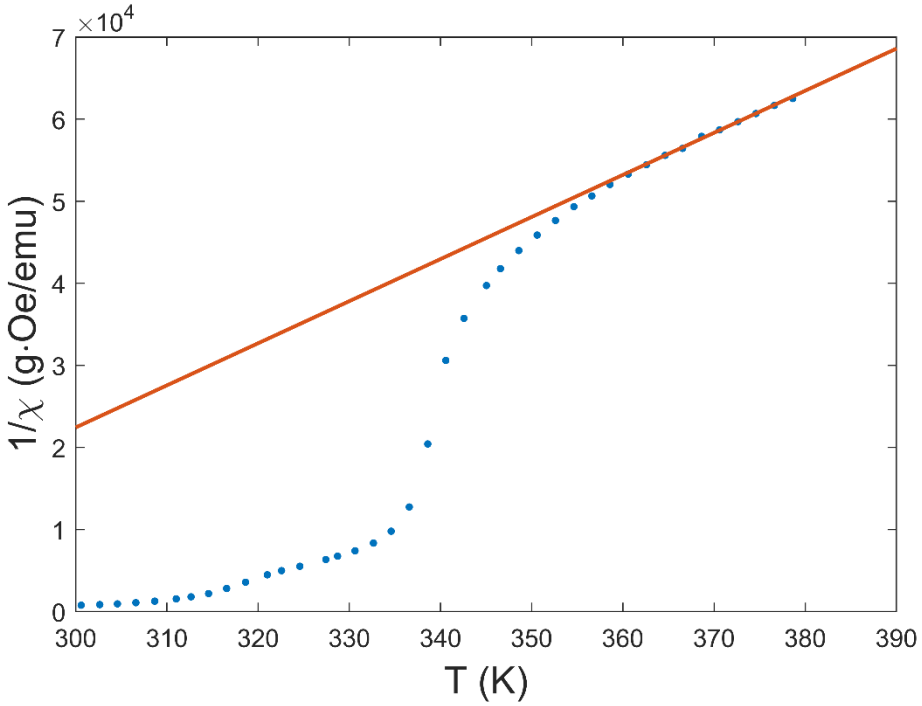

Figure 5-12 Curie-Weiss plot of data collected for BCMO in ZFC mode at 10 Oe applied.

where k_B is the Boltzmann's constant, N_A is the Avogadro's number, μ_B is the Bohr magneton value, and MW is the molecular weight of BCMO. The value for θ_{CW} suggests that the mean sign of the interaction is positive (ferro-type), while the observed magnetic moment per f.u. as μ_{obs} = (3.17±0.06) μB. This calculated value is well consistent with the theoretical value of Bohr magnetons in the high spin configuration, which for the unit cell is equal to 3.21 μB. In this evaluation I have considered a perovskite with a compositional Mn^{4+} and Cu^{2+} ratio species in the atomic ratio of 61 % to 39 % respectively, as experimentally evaluated from Rietveld refinement of PXRD-NPD patterns, and their relative mean value for the magnetic moment. Despite also the small spurious phase related to CuO can partially affect the observed magnetic moment, this contribution has been considered as negligible with respect to the major BCMO one, and this is reasonable since CuO is paramagnetic in this thermal region [172] [173].

M(H) measurements have been carried out at specific temperatures in order to better analyse the magnetic regimes identified in BCMO by the previously reported M(T) curves. The results are reported in Figure 5-13. The paramagnetic state was confirmed by the linear trend of the M(H) curve recorded at 370 K. As the system is brought down to the hypothesized AFM thermal threshold at 50 K, a non-hysteretic magnetic loop forms even though its intrinsic character sets clearly up

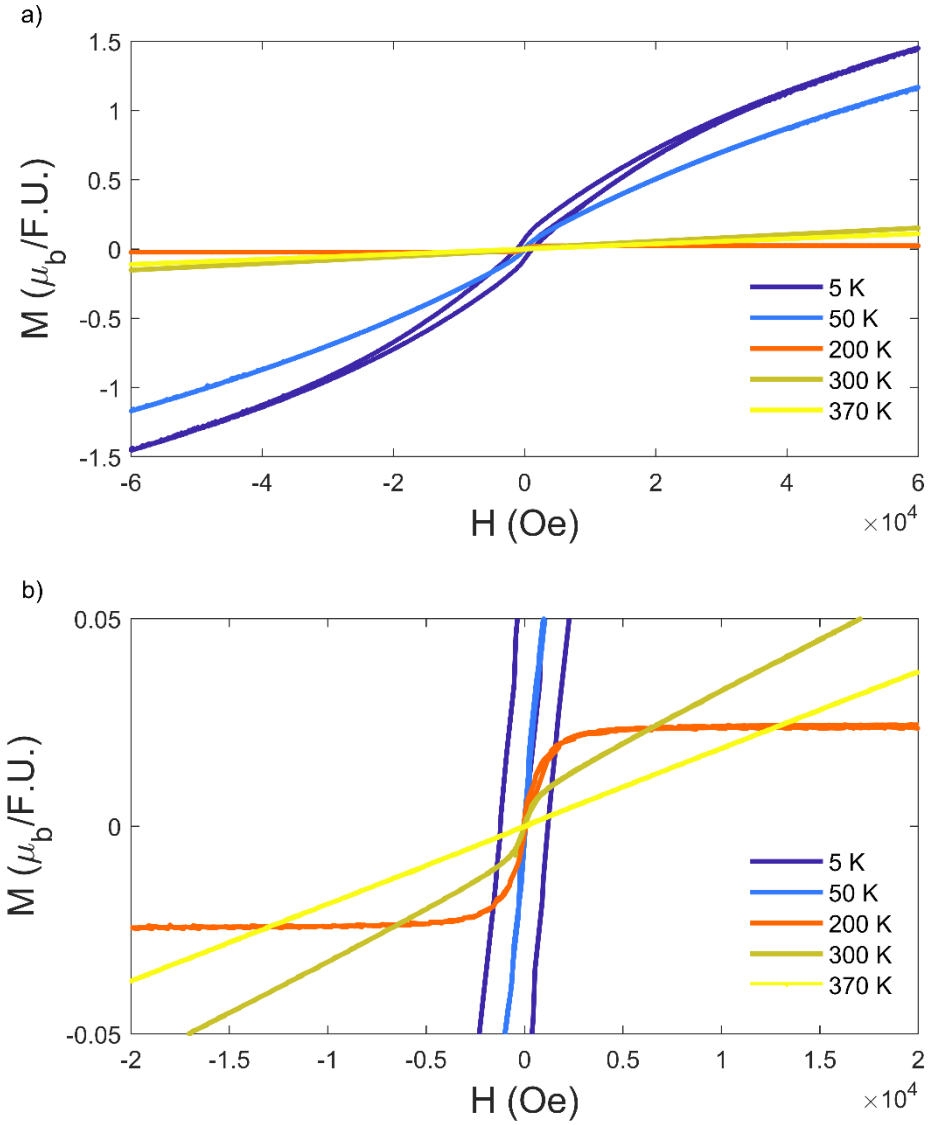

Figure 5-13 Magnetization vs. applied magnetic field measurement acquired in ZFC at different temperatures (a). Zoom of the data at low H (b).

only at 5 K with the completion of the AFM order, showing a complex-shaped hysteresis loop, with H_c about 1200 Oe and non-saturated trend of the magnetization in the high field regime. The presence of such complexity in the loop suggests the superposition of different magnetic arrangements or, at least, a magnetic disordered system, while the non-saturated loop marks the predominance of the AFM components with respect to the high temperature FM-like components. Moreover, the detection of a considerable number of Bohr magnetons, around over 1 μB in the regime in which the branches of the loop are superimposed, seems to enforce the thesis of the presence of a weak FM signal (underlined by subtracting the linear background of the M(H) curve recorded at 200 K, where the FM state saturates)

coming from a giant spin canting effect probably in the AFM order, as highlighted by the M(H) shape in Figure 5-13b.

Magnetic features related to the presence of compositional inhomogeneities and, mainly, cationic disorder, are not new in perovskite systems. Similar behaviours have been observed in the parent compound BFMO, where the hypothesized presence of different clusters with a concentration of more iron or manganese ions has been pointed out to induce competing exchange interaction mechanisms [66]. Similarly, in BCMO the hypothetical presence of clusters with more copper or manganese, or with different concentrations of various oxidation states of copper and manganese at the B site of the perovskite, could contribute to the overall magnetization with different magnetic resultants, according to GKA rules, and ordering temperatures due to the competition of Cu-O-Cu, Mn-O-Mn, and Mn-O-Cu super exchange interaction mechanisms.

5.2.6 Nuclear Magnetic Resonance

To verify the possible presence of different oxidation states of the magnetic cations at the local level, several NMR characterizations have been carried out in a wide range of temperatures, namely from 260 K to 1.4 K.

In the low temperature regime, ZF ^{55}Mn spectra have been acquired at 1.4 K, 8.4 K, and 77 K and reported in Figure 5-14, where the NMR peaks of different species, analysed with the deconvolution in Gaussian signals, are clearly visible. Considering at first the 1.4 K spectrum, the two main narrow peaks around 305-340 MHz are ascribable to Mn^{4+} ion, in accordance with its isotropic character. The splitting in two distinct lines is due to a different magnetic environment with nearest-neighbours ions. On the contrary, a larger peak with low intensity around 360 MHz is related to the anisotropic Mn^{3+} ion. The arising of Mn in two distinct valency states is reasonable when using HP synthesis techniques. At lower frequencies, the resonance emerging around 100 MHz is compatible with ^{209}Bi, despite the experimental conditions are not optimized to observe its spectrum. The fingerprint of ^{209}Bi species has been already measured in similar perovskites such as $BiMnO_3$ from HP/HT. However, the broad peak centred at 200 MHz is more cryptic and not easily ascribable to a particular ion. The partial change of the

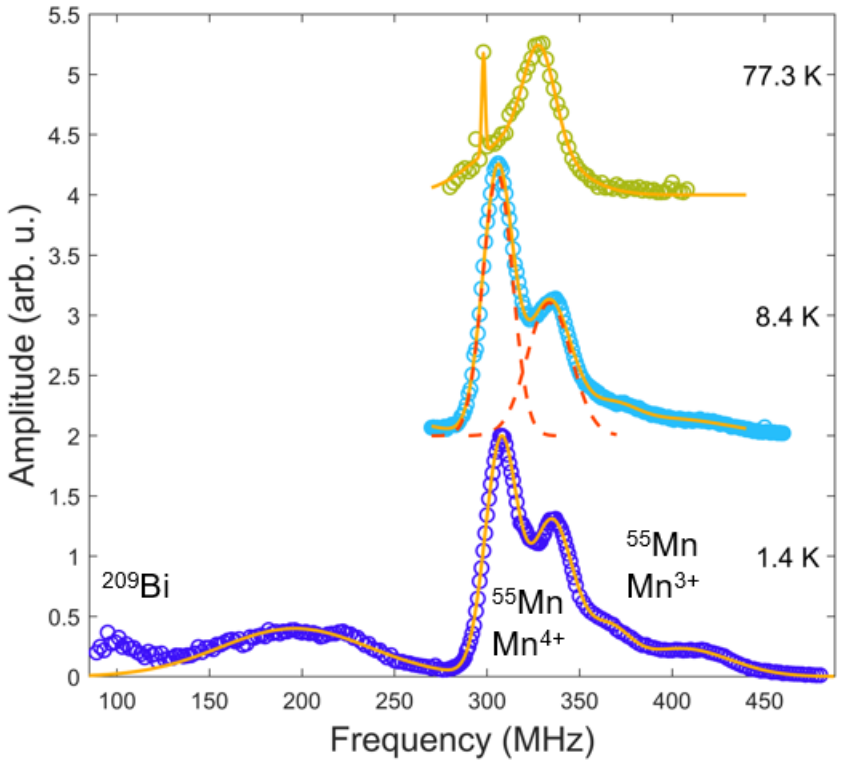

Figure 5-14 NMR spectroscopy of BCMO in the low temperature regime, with Gaussian fit of the resonance peaks.

oxidation state of Mn from 4+ to 3+ can also suggest the presence of Cu in both the 2+ and the unusual 3+ valency states. Nevertheless, the stoichiometric amount of around 40% for copper to around 60% for manganese cations pointed out from SEM-EDX and XRD/ND refinement ensure the charge neutrality of the system by just considering Cu^{2+}, Mn^{4+}, and Mn^{3+} populations. In this framework, this broad peak could be related to this variation of Cu oxidation state, sometimes observed in Bi-based perovskites but, to my knowledge, never investigated before in literature through solid-state NMR.

The spectrum recorded at 1.4 K evolves significantly by increasing the temperature. The only detectable NMR signal is related to the ^{55}Mn, but with considerable deviations in the spectra acquired at 8.4 K and at 77 K (Figure 5-14). Specifically, the resonance peak attributed to Mn^{3+} population lowers its intensity by increasing T, and completely disappears at 77 K. On the other hand, the relative intensity of the two NMR peaks related to Mn^{4+} species evolves. Namely, the one at around 340 MHz, the smaller at 1.4 K, increases its intensity till 77 K, where the originally highest resonance peak at 305 Hz almost totally relaxes, losing the

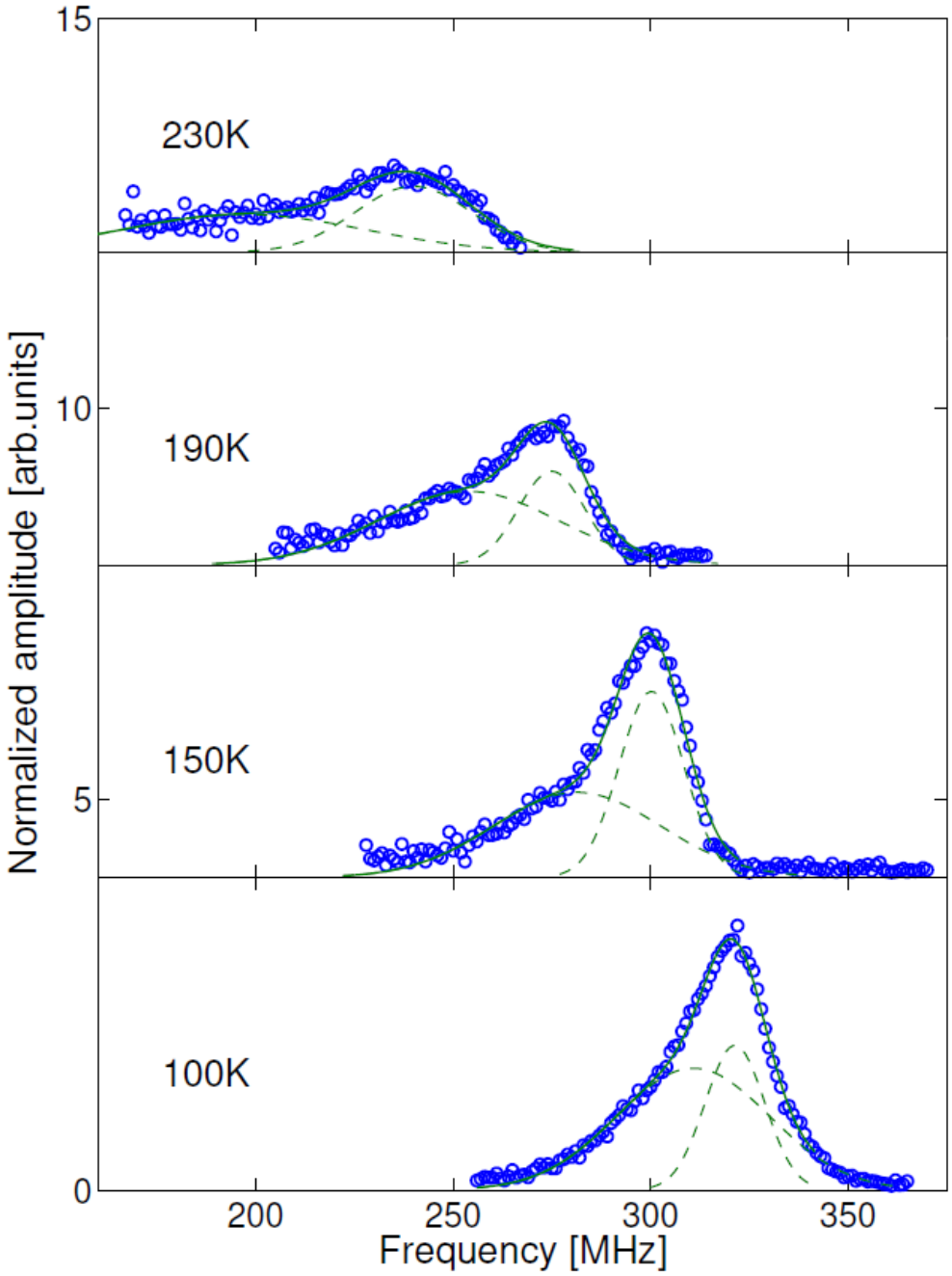

Figure 5-15 ZF ^{55}Mn spectra of BCMO at different high temperatures.

Gaussian shape towards a narrow lower peak at the liquid nitrogen. The temperature evolution of BCMO NMR spectra suggests that, while at low temperatures both Mn^{3+} and Mn^{4+} species are present, the latter with different coordination and hyperfine interaction with the nearest neighbours, the electron localization on Mn sites decreasing by increasing T and the Mn^{4+}, the only surviving manganese population, almost loses one atomic coordination with the surrounding environment. This behaviour could be related to the AFM ordering, arising at

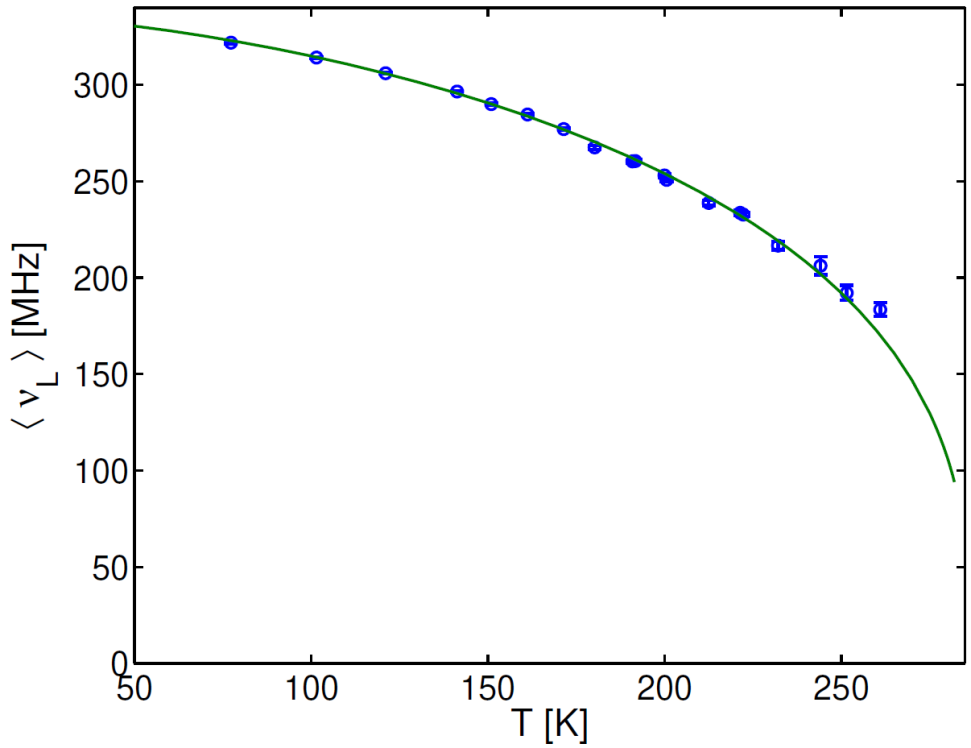

Figure 5-16 Mean resonance frequency of Mn NMR signal as a function of temperature, with exponential fitting.

around 50 K, detected with SQUID magnetometry (Figure 5-11), as mainly related to the presence of Mn^{3+} in the system.

To better evaluate the populations' thermal evolution in BCMO, ZF ^{55}Mn spectra have been acquired also in the high temperature regime, from liquid nitrogen to 260 K. In Figure 5-15 some NMR signals recorded at specific temperatures in this range are reported as an example. The resonance peak mainly visible is the highest frequency one of Mn^{4+}, occurring around 325 MHz at 100 K. However, the asymmetric peak shape is due to a bimodal ascription in two Gaussians, despite the progressive loss of the lower frequency Mn^{4+} coordination, in analogy to the low temperature behaviour, which contribution can be fitted by considering a very bread Gaussian function (see Figure 5-15, 100 K). The bimodal Mn^{4+} peak evolves raising the temperature by lowering its resonance frequency and of course its intensity, up to 240 MHz at 230 K. Despite the NMR signal being ever more suppressed at high temperatures, in Figure 5-16 the mean resonance frequency of Mn NMR contribution has been evaluated as a function of temperature. The data seems to reproduce quite well the trend of a conventional order parameter, and the curve can be exponentially fitted with a resulting T_C* of around 285 K, not too far

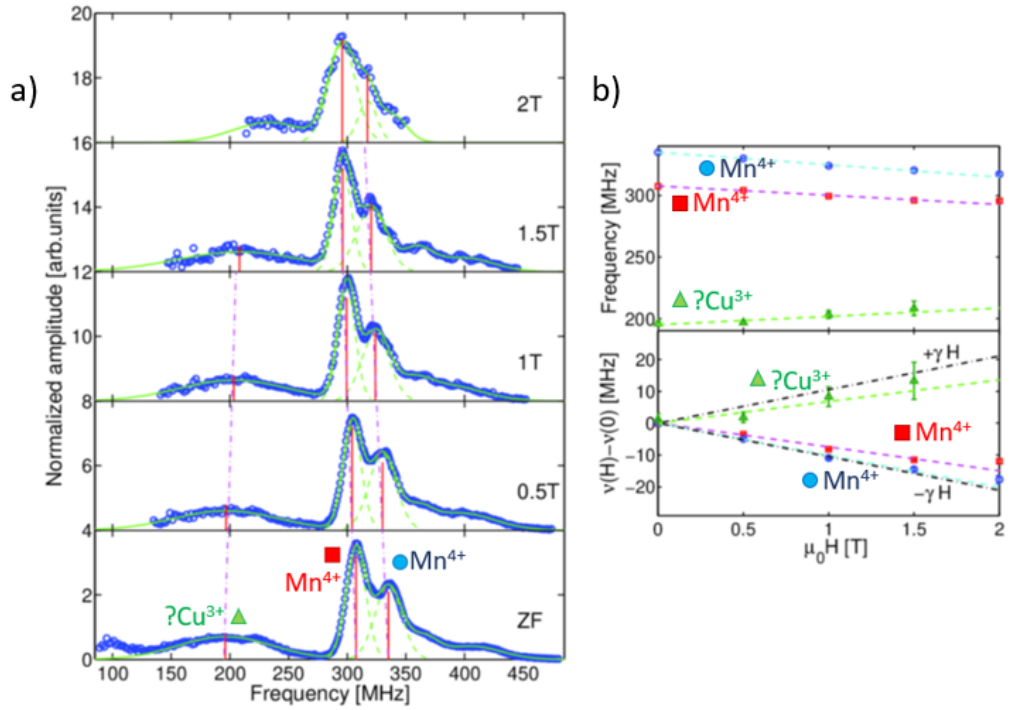

Figure 5-17 NMR spectra of BCMO with different applied magnetic fields at 1.4 K (a). Evolution of marked resonance peaks (blue circle and red square for Mn^{4+}, green triangle for possible Cu^{3+}) with respect to the classic FM or AFM arrangement (black dashed lines) (b).

from the thermal threshold detected by magnetometry measurements at low magnetic field previously reported. Indeed, T_C* is smaller than the macroscopic T_C of the ferromagnetic-like high temperature state of BCMO, supporting the hypothesis of a second order character of this magnetic transition, since it arises from a very weak NMR signal involving Mn^{4+}. The results obtained by solid-state NMR analysis of BCMO at high temperatures suggest that the high temperature ordered state of this novel perovskite is mainly due to the interaction between Mn^{4+} cations, probably mediated by the presence of Cu^{2+}.

Further NMR measurements have been performed at 1.4 K by perturbating the system with an applied magnetic field up to 2 T, whose results are reported in Figure 5-17a. The consequence of this perturbation is to induce a shift of the resonance peaks due to the hyperfine coupling. In this case, it is possible to evaluate for each ion the magnetic moment alignment with respect to the external magnetic field. Starting from the stronger NMR signals, the Mn^{4+} peaks frequency (305-340 MHz) evolves vs. field intensity with a negative slope, but with a different rate (blue and red slope of Figure 5-17b). This means that, by increasing the magnitude of the magnetic field, the two peaks get closer and closer in frequency. Since the hyperfine

field is negative due to the sign of this trend (Figure 5-17b), this feature suggests that all the Mn^{4+} at 1.4 K are interacting in concordance with the field (ferro-like interaction). Moreover, the observation of two different trends of the frequency as a function of the field behaviour seems to indicate that two different magnetic populations of Mn^{4+} are present. Specifically, the Mn^{4+} site at the high frequency resonance has a parallel alignment of its magnetic moment with respect to the applied magnetic field, close to the theoretical value of $-\gamma/2\pi$=-10.5 MHz/T for ^{55}Mn, with the trend of a ferromagnetic-like order (black dashed line in Figure 5-17b). On the other side the Mn^{4+} site, corresponding to a lower frequency resonance peak, follows a trend with a reduced slope rate compatible with a non-collinear ordering of the moments. Finally, considering the peak at 200 MHz, which is not clearly attributed to a particular species but can be addressed to an increasing population of Cu^{3+} as hypnotized from the ZF ^{55}Mn NMR investigations, its resonance shifts with the external perturbative field to slightly higher frequencies, showing an opposite behaviour with respect to the previous cases as a non collinear antiparallel system.

All the observations highlighted by solid-state NMR confirm a very complex magnetism in BCMO, in which probably the nature of competing magnetic interactions between copper and manganese, in their different oxidation states, evolves with temperature leading to the macroscopic magnetic transitions detected with SQUID.

5.2.7 Temperature-dependent analysis of nuclear and magnetic structure

To clarify the tricky magnetism of BCMO underlined via the combined approach of SQUID magnetometry and NMR characterizations, PND experiments have been performed at different temperatures, namely at 370 K, 300 K, 200 K, 75 K, and 7K, investigating the key thermal regimes in which BCMO macroscopically displays magnetic ordering variations. Each diffraction pattern has been acquired for around 3 hours on a 103 mg sample.

From these measurements, the nuclear structure modelled for BCMO and shown in Paragraph 5.2.3 has been confirmed, without any structural transition in the explored thermal range.

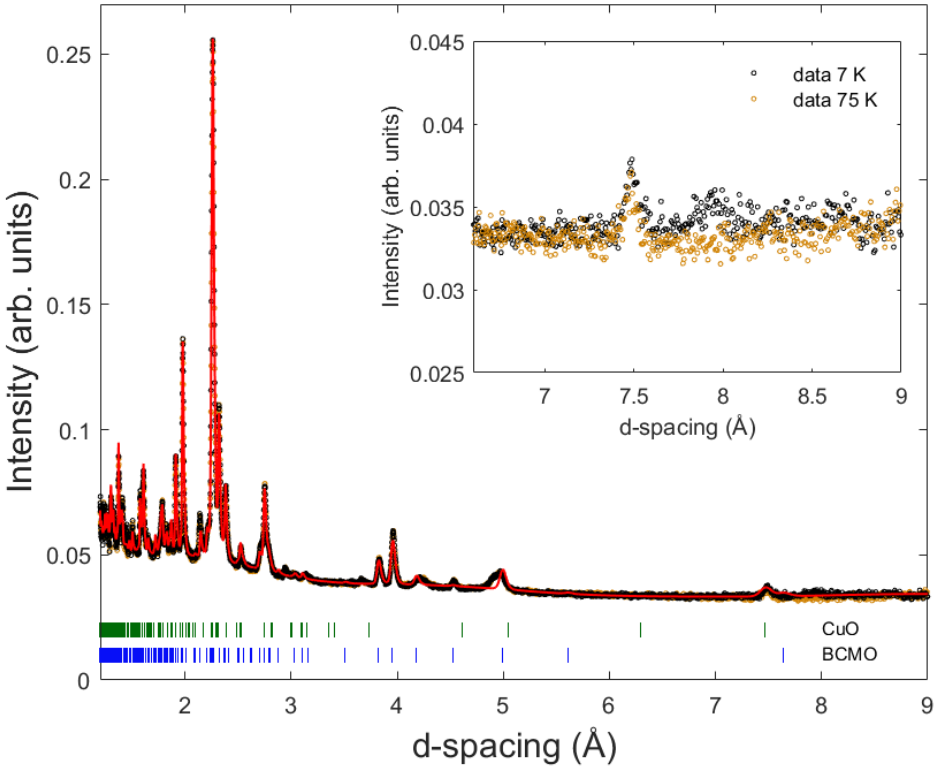

Figure 5-18 Neutron powder diffraction data of BCMO acquired at 7 K (black dots) and 75 K (orange dots). In red the calculated intensities for the dataset at 7 K are reported. For CuO both magnetic and nuclear reflections are reported in green. Inset: A small magnetic peak arises at low temperatures at around 7.9 Å, ascribable to BMCO magnetic structure, visible by comparing 75 K and 7 K datasets.

Regarding the possibility of magnetic long-range ordering, no magnetic diffraction peaks have been revealed in correspondence with the FM-like state ordering at high temperatures. This absence can be associated with a possible spin-glass phase of BCMO or, at least, with a short or local-ranged magnetic ordering, coherent with the detected disorder at the B site of the perovskite and the hypothesized presence of clusters with different concentrations of copper and manganese cations.

On the contrary, crossing the AFM transition at around T_N=50 K, in the low-temperature regime, only a small broad peak arises at a d-spacing of ~7.9 Å of d-spacing, as highlighted in the inset of Figure 5-18. The presence of just one magnetic reflection, with a very small intensity and a broad shape in the d-range, suggests that the AFM state is characterized by a very small magnetic moment, or that not all the sample contributes to the ordering. Nevertheless, this visible magnetic peak is compatible with the propagation vector $\vec{k}$=(0.5, 0, 0). Considering

P[c]2/m - type IV P2/m [#10]
P[c]2/c - type IV P2/c [#13]
P[a]ca21 (type IV) Pca21 [#29]

Table 5-4 List of possible magnetic space groups compatible with the detected magnetic peak of BCMO.

such propagation vector as reliable for the description of BCMO AFM commensurate state, symmetry analysis has been performed with the ISOTROPY software [174] to investigate possible magnetic space groups compatible with the observed magnetic peak. It is worth stressing that a refinement of the magnetic model is not possible due to the observation of a single magnetic peak, but this exercise can give a small number of candidates for which the observed peak is the expected most intense reflection. Indeed, considering the magnetic moment on manganese/copper site, only the magnetic space groups compatible with the major magnetic peak displayed at 7.9 Å have been selected and listed in Table 5-4, as suitable for the magnetic description of BCMO. In the whole analysis, the magnetic contribution of CuO phase has been considered, whose magnetic peaks arise from a AFM commensurate state characterized by the propagation vector $\vec{k}$=(0.5, 0, -0.5), around T_N~213 K, when the system undergoes an incommensurate-to-commensurate AFM transition, and thus contributes to the acquired neutron diffraction patterns at 200 K, 75 K, and 7 K [175].

The results shown by neutron diffraction experiments suggest the lack of a large long-range magnetic ordered component in BCMO. Indeed, the local magnetic ordering of the magnetic species verified with NMR measurements (see Paragraph 5.2.6) is not extended on the structure as a long-range magnetic ordering. The only fingerprint of weak long range magnetic ordering is constituted by the small broad magnetic peak at 7.9 Å.

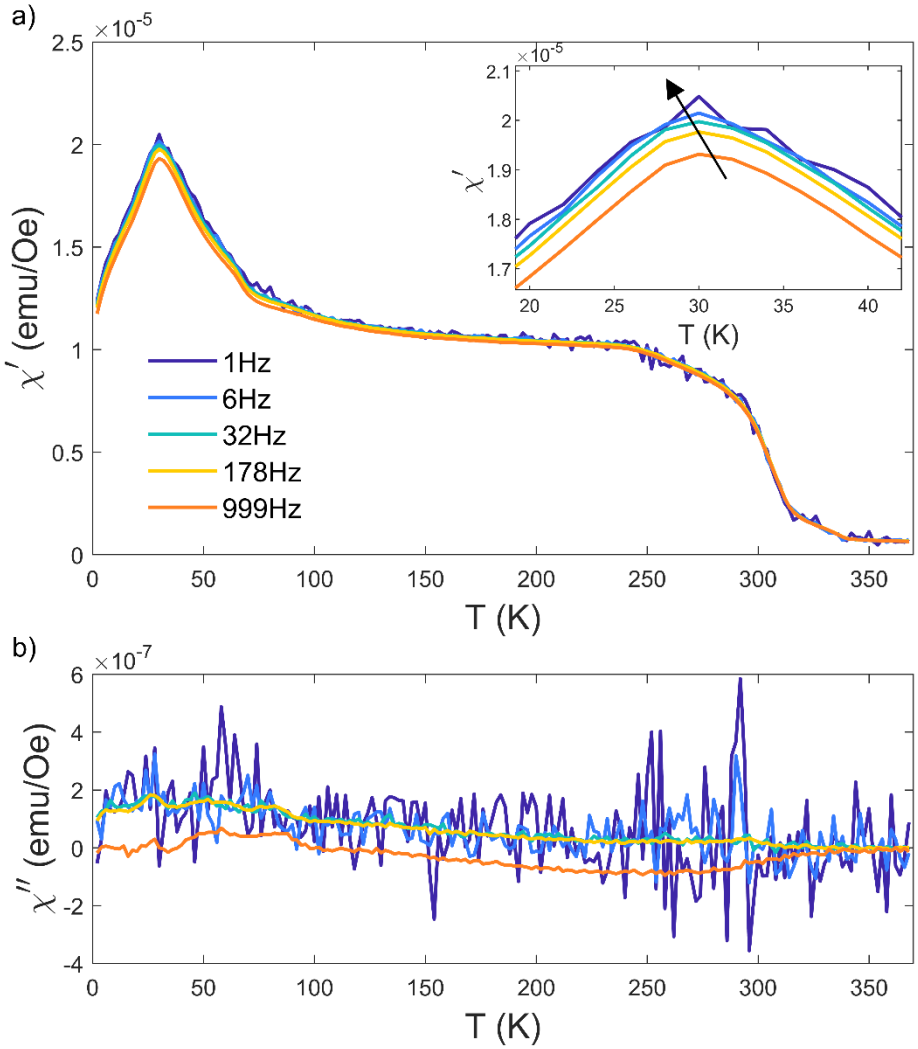

Figure 5-19 Real (a) and imaginary (b) part of susceptibility vs T of BCMO measured at 1 Oe and various AC frequencies. Inset of (a): zoom on the AFM transition with the slight deviation in T and magnitude.

5.2.8 Local magnetic ordering in BCMO

As pointed out with ND, the magnetism of BCMO is not characterized by a long-range ordering. To better understand this feature, AC SQUID magnetometry measurements have been carried out, and the real and imaginary components of the susceptibility curves, acquired with an applied magnetic field of 1 Oe with different frequencies, are reported in Figure 5-19 a and b, respectively.

The in-phase χ' part shape reproduces in temperature the M(T) trend of BCMO previously reported (see Paragraph 5.2.5), with the two detected magnetic transitions at around 320 K and 30 K. By varying the frequency of the applied magnetic field, the AFM transition slightly varies in T and magnitude, proper feature of spin-glass systems in which the freezing temperature is frequency-

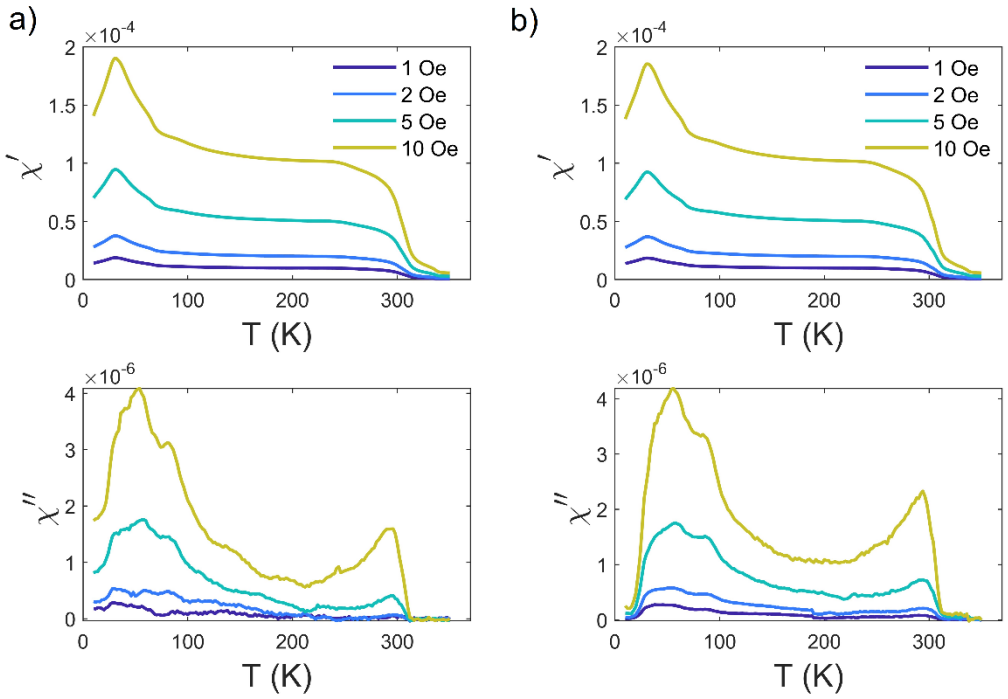

Figure 5-20 AC SQUID measurements on BCMO at 999 Hz (a) and 9999 Hz (b).

dependent, as for instance it has been detected in $Cu_{1-x}Mn_x$ alloys [176]. However, this effect is very small, as highlighted in the inset of Figure 5-19a. On the contrary, the out-of-phase component χ'', which indicates dissipative processes in the sample, displays non-zero values below the freezing temperature (Figure 5-19b), indicating a possible spin-glass behaviour. Moreover, an anomaly seems to occur at 999 Hz, when the χ'' component assumes negative values in correspondence with the arising of the FM-like state (Figure 5-19b, orange curve). This phenomenology has already been detected in $Nd_{0.5}Sr_{0.5}MnO_3$ perovskite, in which this anomaly has been explained from considerations about the magnetic free energy and thermodynamic potentials of metastable phases near its magnetic first order transition [177]. Indeed, by looking carefully at the M(T) curves, BCMO FM-like transition seems to be a "two-steps" transition, in which a minor phase orders at around 320 K, while the major magnetic phase is responsible for the following stronger increase in magnetization with an inflection point at around 310 K. However, since the recorded values display a quite high uncertainty error around the zero values, additional AC measurements, using a PPMS (see Paragraph 4.6) have been performed by varying the applied magnetic field at 999 Hz and 9999 Hz, shown in Figure 5-20a and b, respectively. χ'' vs T assumes clearly different values

above zero, thus losing the negative χ'' at high frequencies detected in the previous measurement configuration and confirmed the spin-glass tendency of BCMO.

5.2.9 Electrical transport characterization

After the extensive characterization of BCMO structural and magnetic properties, and after having established that ferroelectricity is forbidden by its crystal symmetry, I have investigated the electronic transport of BCMO. The resistivity behaviour, measured in planar-plate configuration (two contacts), as a function of temperature is reported in Figure 5-21. During the measurements, two different currents have been applied, i.e.500 μA (yellow dots) and 20 μA (blue dots), in order to properly investigate the electrical resistance in a quite extended values regime. Indeed, the system displays a semiconductive-like character with a conductive RT-state characterized by a resistivity of 10^3 Ω·cm, which rapidly evolves vs. T up to $3 \cdot 10^7$ Ω·cm at around 150 K.

Namely, two distinct electrical regimes are present. Firstly, at high temperature the ρ curve follows the thermally activated trend expected for an ideal semiconductor. A fitting of these resistivity data, recorded with a high induced current, ideal condition to probe a high conductivity state, with the Arrhenius model, reported in Paragraph 2.4.2, allows the estimation of an activation energy E_A = (0.263±0.007) eV, confirmed by a good coefficient of determination of R^2=0.9998. On the contrary, a clear deviation from the thermal-activated electrical transport mechanism is detected around 240 K, exactly in the thermal regime in which the high-temperature ferromagnetic-like order completely stabilizes and concurrently the second AFM order starts to arise. These datasets have been analysed with different models for hopping mechanisms applied for disordered or partially ordered semiconductive/ bad dielectrics systems (see Paragraph 2.4.2). By comparing the relative R^2 values, it has been proven that in this thermal range the resistivity behaviour is more properly described by a 3D Mott's Variable Range Hopping model, as reported in the inset b of Figure 5-21, with R^2=0.9998 (slightly higher than the values related to the other models at R^2=0.9990). As said before, this electric transport mechanism is common in perovskites, especially when cationic disorder occurs [84]. Such characteristics are owned also by BCMO, which displays a cationic disorder at the B site between Mn and Cu, as verified in the

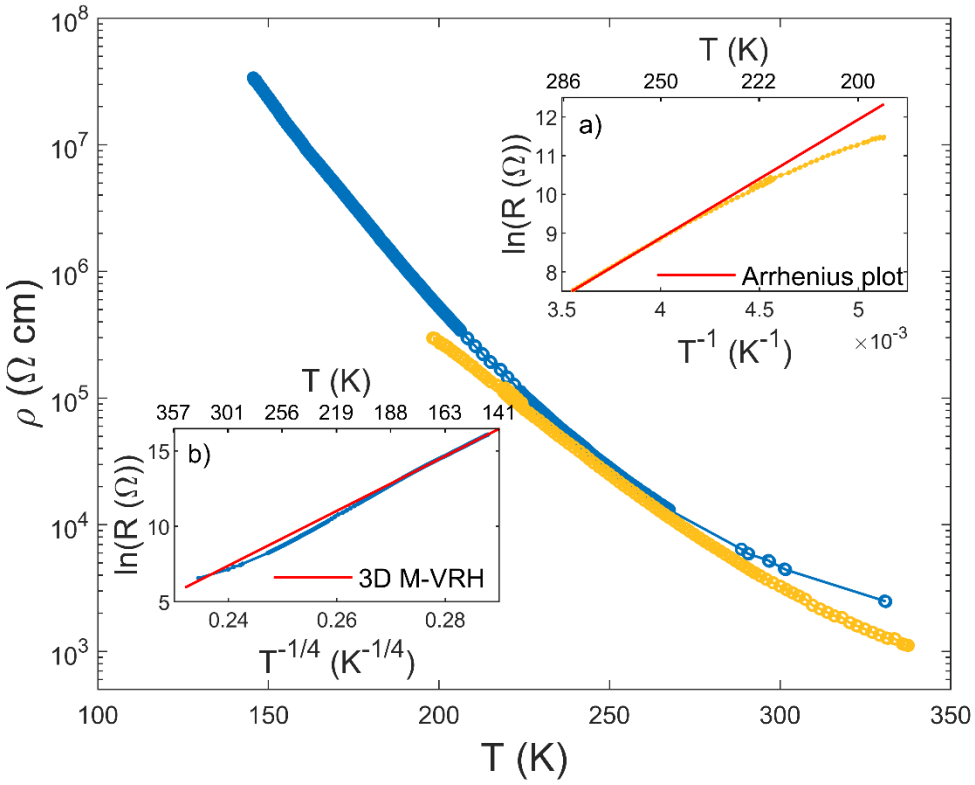

Figure 5-21 Resistivity vs temperature of BCMO with high and low range modelled in insets. The yellow curve corresponds to the HT dataset acquired with an applied current of 500μA (fit in the upper inset), while the blue curve reports the LT dataset recorded with an applied current of 20 μA (fit in the lower inset).

previous paragraphs. This result supports the hypothesis of different electronic transport paths along the three directions driven by the Mott's hopping mechanism.

This behaviour at low temperatures suggests a possible correlation between magnetism and electrical properties of the material. Indeed, it can be explained as a consequence of the partial localization of the electrons, which at high temperatures are delocalized and contribute to the conductivity while in the low field regime they become gradually involved in the incoming low T magnetism.

5.2.10 $BiCu_{1-x}Mn_xO_3$ solid solution: an additional degree of tunability

The physical characterizations of BCMO reported so far have revealed interesting features and a possible great potential of this novel perovskite, at least at the fundamental level. Indeed, the most promising peculiarity of BCMO is undoubtedly the existence of a FM-like state at considerably high temperatures, with an onset temperature of around 320 K and spontaneous magnetization two times greater concerning the parent compound BFMO. The enhancement of the HT

ordered state magnitude represents a very important goal, making this compound possibly suitable for spintronic and energy applications at room temperature. However, the possibility to induce ferroelectricity, as for BFMO by a proper external electric bias forcing the breaking of its antiferroelectric structure, has been completely lost, avoided by the centrosymmetric space group Pbam which describes BCMO crystallographic structure.

Within this framework, I have explored the possibility of balancing the benefits of introducing Cu^{2+} at the B' site of the perovskite, which seems to guide the enhancement of the HT FM-like ordered state, with the retention of a low crystallographic symmetry (i.e. non-centrosymmetric space group). For this aim, I have investigated the $BiCu_{1-x}Mn_xO_3$ solid solution, varying the relative stoichiometric ratio between copper and manganese. This job, as always concerning HP/HT syntheses attempts, turned out to be very tricky also for the lack of any information about the end member x=0 perovskite with only copper at the B site, $BiCuO_3$, which has not yet been synthesized so far. This makes it more difficult to obtain a sufficiently pure phase with low x values (i.e. larger amount of Cu). I have tried anyway to explore the Mn-rich stoichiometries by synthesizing, additionally to the x=0.5 case, the solid-solution members with x=0.75 and x=0.9. Unfortunately, I have not yet found the best pressure, temperature, and reaction time conditions for these two additional compositions, ending up with not so pure samples with a roughly estimated 70% only of perovskite content volume, preventing any possibility of proposing any model for the crystal structure. The relative PXRD results for the Cu/Mn stoichiometries probed are reported in Figure 5-22a, where the reflection peaks attributed to impurities are marked with black triangles. Nevertheless, I have already performed preliminary magnetization measurements which have revealed promising results that I want to share as a preview in Figure 5-22b, where the behaviour of the magnetization as a function of temperature is reported for all the three explored Cu/Mn stoichiometric variations. The three datasets, acquired between 5 K and 400 K in FC mode with an externally applied field of 10 Oe, display strong deviations both regarding the onset temperature of the high temperature ferromagnetic-like state and its magnitude. With respect to the BCMO, characterized by a broad magnetic transition temperature T_C around 320 K as previously shown, in the x=0.75 composition the

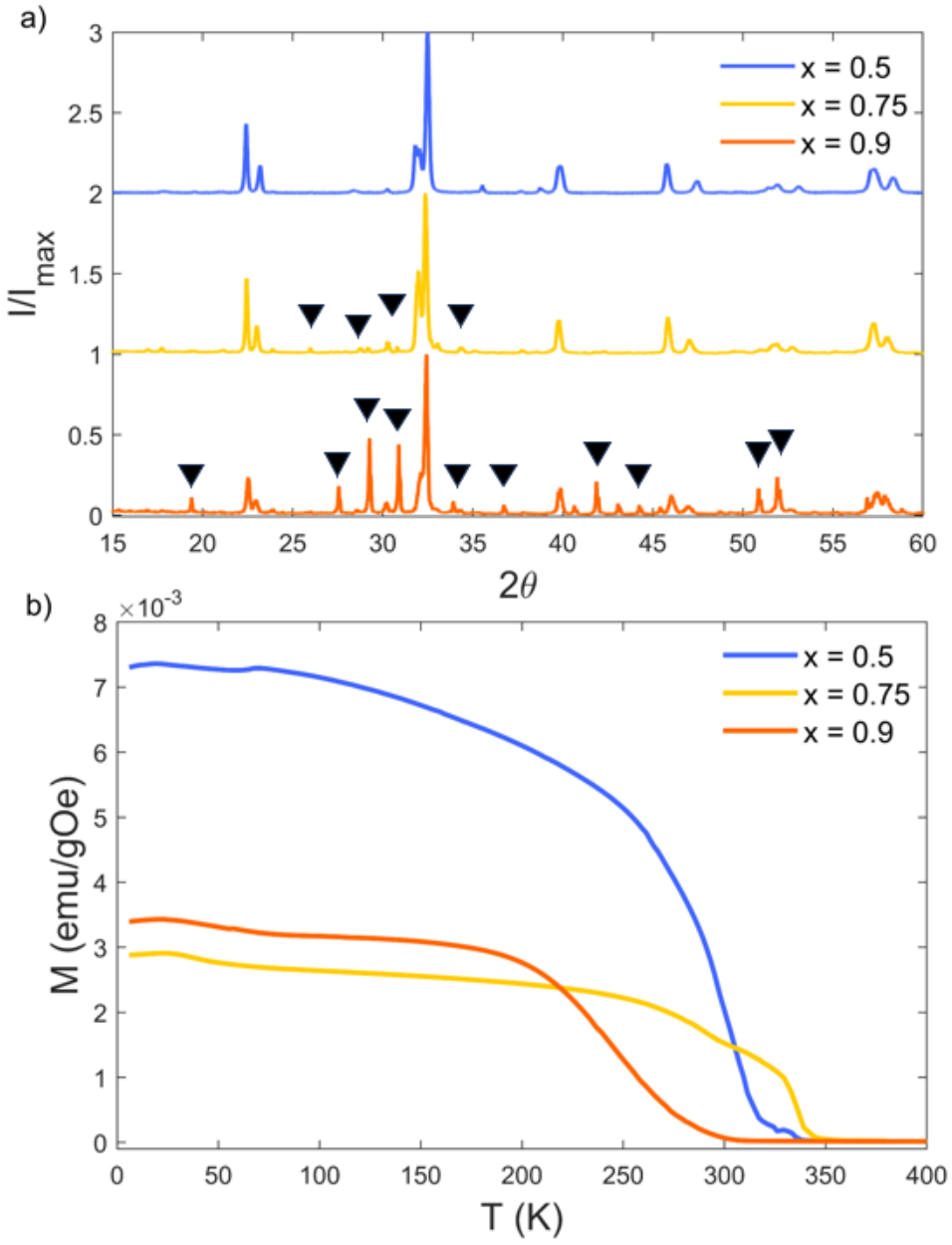

Figure 5-22 PXRD of different $BiCu_{1-x}Mn_xO_3$ compositions, with impurities marked in black (a) and the relative magnetization vs T measurements at 10 Oe (b).

magnetization curve displays a broad "two-step" jump at the high-T magnetic phase transition, with a major onset temperature increased at around 340 K and a more than halved magnetization intensity. On the contrary, for x=0.9, i.e. by introducing even more manganese at the B'' site, the magnetization value at the saturation of the broad FM-like state is slightly reduced with respect to the case of $BiCu_{0.25}Mn_{0.75}O_3$, while its onset temperature is significantly decreased at about 250 K. In spite of experimental evidence coming out from the magnetic measurements this constitutes just the first step in the investigation of

$BiCu_{1-x}Mn_xO_3$ solid solution, and considering that the synthesis of further compositions of the solid solution are mandatory. Some tentative considerations can be already hypothesized in order to describe the trend of M(T) curves in terms of the Cu/Mn relative content. Firstly, the composition with the highest selected x value, x=0.9, reduces its temperature onset probably collapsing towards a $BiMnO_3$ character, in which, however, an AFM state arises at around 100 K, induced by Mn^{3+}-Mn^{3+} interaction investigation [29] [134] [164]. On the contrary, in BCMO (x=0.5) it seems that the HT FM-like order is mainly driven by Mn^{4+}-Mn^{4+} interactions, probably mediated by Cu^{2+}, as suggested by NMR analyses (see Paragraph 5.2.6), which favour the enhancement of the FM-like onset temperature and the magnetization intensity. The intermediate studied composition with x=0.75 seems to disadvantage the Mn^{4+}-Mn^{4+} interactions by introducing more manganese in the 3+ valency state for a charge balance, thus reducing the saturation magnetization. However, the onset T value is in this case increased, but in this framework any hypothesis at this stage could be just speculative.

In conclusion, the exploration of $BiCu_{1-x}Mn_xO_3$ solid solution can be effectively useful in order to maximize the degree of tunability of Bi-based perovskite families, opening a large set of novel perovskites to be studied.

5.2.11 Conclusions on BCMO

After having presented all the physical characterizations carried out in BCMO during my PhD, I would like to sum up the main results of this novel perovskite.

$BiCu_{0.5}Mn_{0.5}O_3$ is a B-site disordered perovskite, synthesized and meta-stabilized for the first time to my knowledge in bulk form under HP/HT conditions. It crystallizes in an orthorhombic structure with Pbam centrosymmetric space group, with high distortion of the octahedral scheme probably due to the stereochemical effect of Bi^{3+} cations at the A site. The cationic disorder at the B site, and probably the presence of clusters with different concentrations of Cu^{2+} or Mn^{4+} species, leads to the absence of strong long-range magnetic orderings, while a spin-glassy AFM behaviour and a weak magnetism are the predominant observed characteristics.

The reported experimental data underlined a correlation between the magnetic and electrical properties of BCMO, which can be explained by considering distinct thermal regimes. Specifically:

1) For T > 330 K, the system is paramagnetic, with a bad-conductive behaviour characterised by resistivity values around 10^3 Ω·cm and a thermally activated transport mechanism defined by an activation energy E_A around 0.26 eV.
2) For 250 K < T < 330 K, the system undergoes a weak FM-like transition with T_C=320 K, driven by Mn^{4+}-Mn^{4+} interactions and probably mediated by Cu^{2+}, whose ordering is very soft and confined at the local scale. The thermal-activated electronic transport is here retained with the same parameters.
3) Lowering T<250 K, a partial localization of the electrons on the manganese site leads to the increase of Mn^{3+} population, concomitantly to a switching of the electronic transport mechanism to a 3D variable range hopping model, feasible with the cationic disorder.
4) In the low-temperature regime, for T < 50 K, the complete electron localization is associated with the arising of an AFM order confined at the mesoscale, compatible with a propagation vector $\vec{k}$=(0.5,0,0). The system here possibly behaves as a dielectric.

In conclusion, the idea to chemically substitute Cu^{2+} in place of Fe^{3+} cation has led to significant modifications in structural, magnetic, and electrical properties in BCMO. Despite the dielectric (and poling written ferroelectricity) feature of BFMO has been lost, resulting in an overall more conductive behaviour, in BCMO the magnitude of the FM-like state observed at high T has been increased and the transition onset has been moved. Particularly this result gives in my opinion more emphasis to this compound, and thus to all the possible members of the solid solution series $BiCu_{1-x}Mn_xO_3$, for further improvements aimed at a future possible application.

5.3 $KPbFeMoO_6$ (KPFMO): tuning of electrical properties by playing with the A site

Among the functional double perovskites, Sr_2FeMoO_6 (SFMO) is an interesting case, accurately studied due to its high ferrimagnetic transition temperature (T_C = 420 K) together with room-temperature magnetoresistance, which makes it an interesting candidate for spintronic applications [16] [178] [179]. Specifically, the presence of both the Fe^{3+} ($3d^5$) and Mo^{5+} ($4d^1$) ions confers to the material half metallicity [180], which is strongly affected by the possible presence of anti-site defects [181]. The synthesis conditions of such compounds are known to play a central role in determining the degree of cation order, and consequently the properties of the system, particularly the application of high pressure during the solid-state reaction process is reported to decrease the amount of anti-site defects [182] [183].

Pb_2FeMoO_6 (PFMO) is a similar double perovskite with the substitution of Sr^{2+} for the isovalent ion Pb^{2+} which can be stabilized in a pure bulk phase under HP/HT reaction conditions. In analogy to SFMO, PFMO crystallizes in the Fm-3m space group with lattice parameter a=7.9609Å, and it is characterized by a rock-salt ordering of the transition metal cations at the B site. [41]. This compound is characterized by low RT resistivity (considering that this is an oxide compound) and by the retention of a low field magnetoresistive character, while the electronic conduction process has been associated with the variable-range hopping of the carriers in samples characterized by a high degree disorder between iron and molybdenum at the B site [184]. In addition, the high symmetry of the structure excludes the possible existence of spontaneous electrical polarization, avoiding a possible coexistence of magnetism and ferroelectricity, which is also physically ruled out by the non-dielectric nature of the material. Previous works describe the magnetism of the compound in terms of a high-temperature ferrimagnetic ordering process (T_N = 272 K) arising from the Fe^{3+}-O-Mo^{5+} super exchange interaction, resulting in a significant saturation magnetization (1.75 μB) and in a very soft (quasi superparamagnetic) character of the hysteresis loop [41]. Additionally, PFMO shows low-field magnetoresistance, ascribed to field-induced suppression of spin fluctuations.

In this framework, I have decided to try the tuning of PFMO properties, as in the case of BCMO, by playing with the chemistry of this perovskite. Namely, I have stabilized a novel compound $KPbFeMoO_6$ (KPFMO), in which Pb^{2+} cation is partially substituted with the alkali ion K^{+1} in a fifty-fifty stoichiometry ratio. By a partial replacement of lead with potassium, it is possible to decrease the number of free electrons in PFMO. Indeed, consequently to this replacement, the electric charge is reduced at the A site, which is mainly responsible for the overall electronic properties, and, additionally, the presence of potassium decreases the density of possible free carriers thanks to its highly bonded valence shell. The partial retainment of Pb in the structure could be useful to induce ferroelectricity thanks to the stereochemical tendency of this cation. The charge balance should be in principle possible by the consequently enhancement of Mo oxidation state from 5+ to 6+, which should slightly reduce the strong magnetic interaction occurring between Mo and Fe in PFMO, but again increase the dielectric character through the emptying of molybdenum d-shell. To help the stabilization of K^{+1} cation at the A site, whose ionic radius in coordination 12 around 1.64 Å is bigger than the one of Pb^{2+} (around 1.49 Å) [169], the use of HP/HT synthesis techniques is mandatory.

Before presenting my work on the synthesis and the preliminary characterizations related to the novel KPFMO perovskite, I have deeply investigated the electric properties of PFMO samples, synthesized in HP/HT conditions as reported in ref. [41], in order to correlate the discovered results with those of my KPFMO.

5.3.1 Electrical characterization of the parent compound Pb_2FeMoO_6

The investigations of electrical properties of PFMO, particularly resistivity and magnetoresistivity, have been performed by considering a high purity (>95%) polycrystalline bulk sample of this perovskite which was crystallized under HP/HT conditions (5 GPa, 900°C for 1.5 hours) in a Walker-type multi-anvil press by solid-state reaction, starting from stoichiometric amounts of PbO, FeO, and MoO_3 powders. The crystalline structure displays partial cation ordering at the B site involving iron 3+ (ionic radius of 0.55 Å or 0.645 Å considering low or high spin configuration, respectively) and molybdenum 5+ (ionic radius around 0.61 Å),

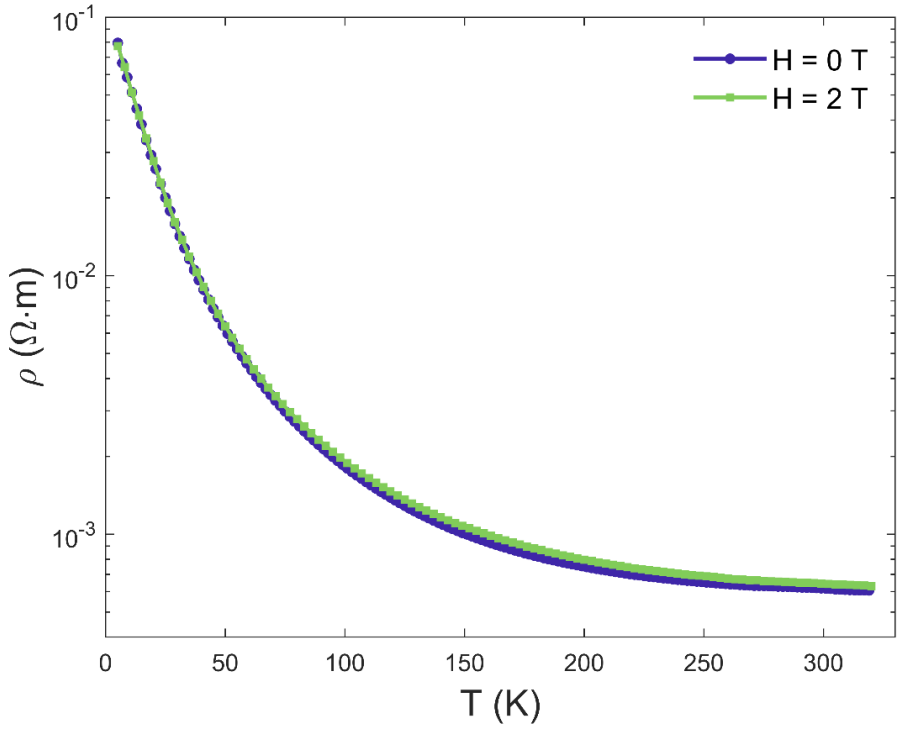

Figure 5-23 Resistivity vs T of PFMO acquired with or without the magnetic field applied (2 T).

demonstrated by selected-area electron diffraction (SAED), synchrotron and neutron diffraction experiments [41].

The resistivity behaviour of PFMO measured as a function of temperature in both the cases of no external magnetic field and under a static field of H = 2 T is reported in Figure 5-23. The two curves appear very similar and show a continuous enhancement of ρ by decreasing temperature. Noteworthy, such a thermal decrease of the resistivity is not describable as a semiconductor thermally activated transport or by any hopping model, as presented in Figure 5-24 and Figure 5-25. The ρ ranges between 10^{-3} Ω·m above RT and 10^{-1} Ω·m at around 5 K, highlighting the overall good conductivity character of the material.

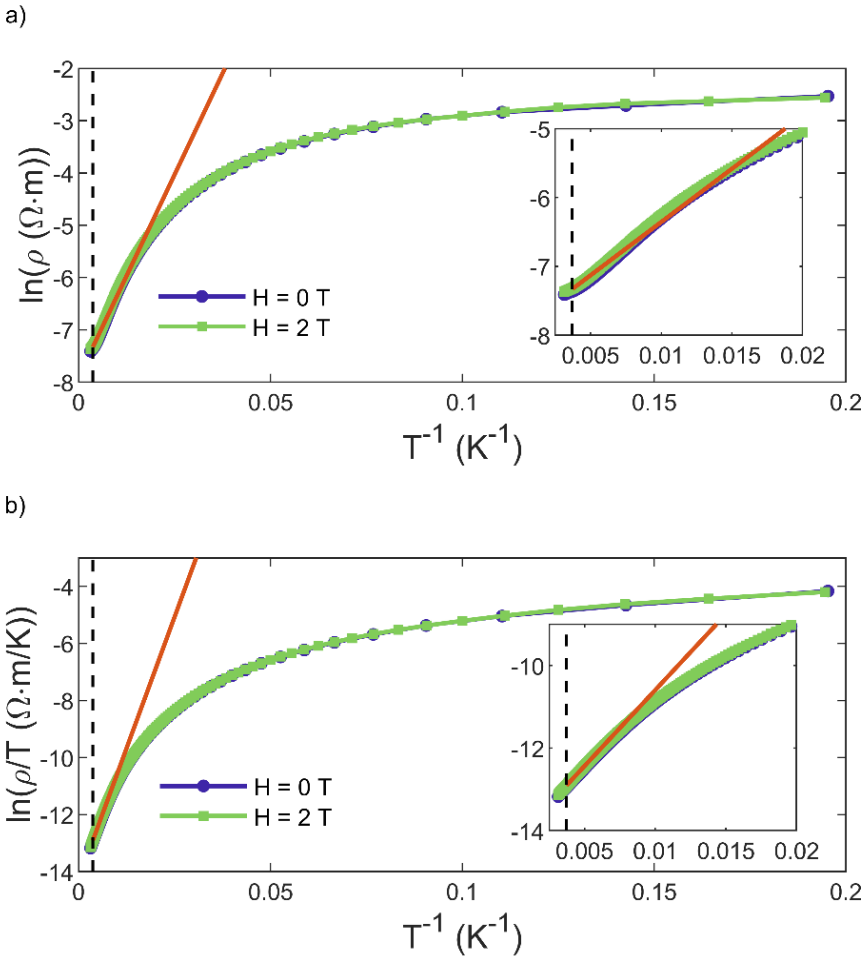

Figure 5-24 Thermally activated model (a) and ANSPH model (b) fit of BCMO resistivity data. The dashed black line indicates the T_N=272 K value.

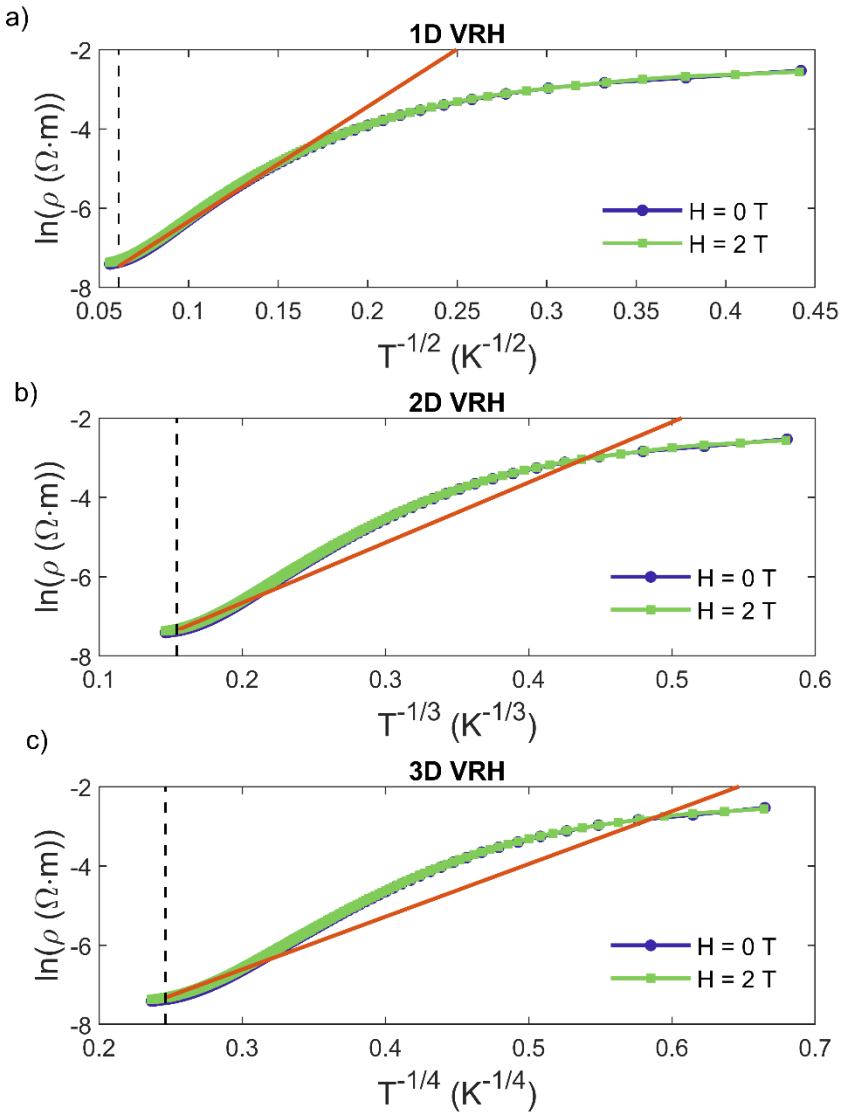

Figure 5-25 Resistivity as a function of temperature considering (a) 1D, (b) 2D or (c) 3D Variable range Hopping mechanism.

In order to further investigate the electrical behavior of PFMO, the incremental ratio of the resistivity $\Delta\rho/\Delta T$ vs. temperature has been calculated (Figure 5-26a). Both the curves, collected with and without the magnetic field applied, display an almost constant and superimposed trend of $\Delta\rho/\Delta T$ in the high temperature regime, above the Néel temperature of PFMO T_N around 275 K (Figure 5-26b). Constant $\Delta\rho/\Delta T$ values (rather if close to zero) imply a linear (or rather almost flat) trend of the main function and the observed mismatch with all the

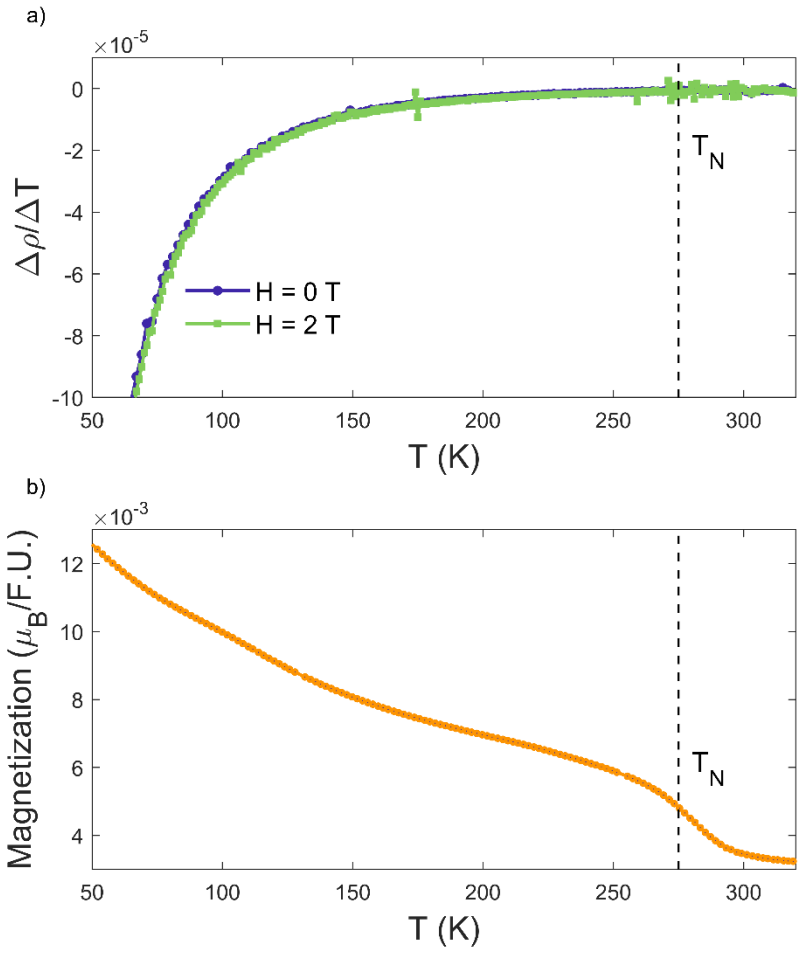

Figure 5-26 a) Incremental ratio Δρ/ΔT as a function of temperature under the application of 0 T (blue dots) and 2 T (green squares); b) Magnetization as a function of temperature measured with an applied field of 10 Oe (Field-Cooling mode).

investigated transport mechanisms suggest a possible semi-metallic behavior of the material [185] [186].

This hypothesis is supported by the anomaly recorded in the resistance trend of PFMO when the sample is heated over the long-range magnetic ordering transition T_N, as reported in Figure 5-27. This change in the transport property at the onset of the magnetic order has been already reported in Heusler compounds as a fingerprint of the possible semi-metallicity [187].

Noteworthy, it should be underlined that when the system transforms into a ferrimagnetic material, the magnetization gradually starts to increase displaying an inflection point towards a positive second derivative when the temperature is lowered below 200 K (Figure 5-26b). Concomitantly, when this inflection point in magnetization is detected, the $\Delta\rho/\Delta T$ starts to continuously increase with

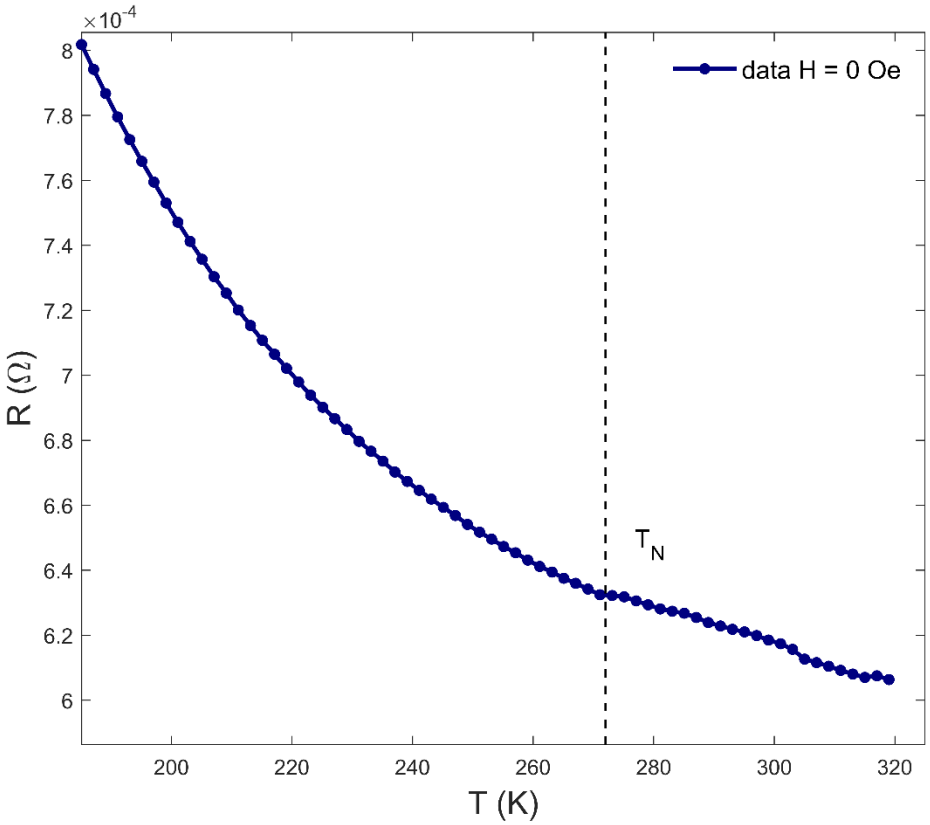

Figure 5-27 Zoom of the resistance values in the high temperature regime, displaying an anomaly in its trend crossing the ferrimagnetic ordering temperature.

comparable T dependence for the measurement with and without positive applied magnetic field, even though with a mild trend not ascribable to any semiconductor transport models (Figure 5-26a). Hence, it seems that the magnetic order can arise only after a partial localization of a minority of electrons on the valence band of the cations at the B site, probably mainly at the Mo site, conferring to the ion a magnetic character (from Mo^{6+} (d^0) to Mo^{5+} (d^1)) and consequently activating the super-exchange interaction with Fe^{3+} along the Fe^{3+}-O-Mo^{5+} straight bond. This consideration agrees with previous neutron diffraction analyses [41], where it was reported the Mo-O bond continuously evolves until the saturation of the ferrimagnetic resultant. Hence, it can be pointed out that magnetic order is the main responsible for the increase of the resistivity below T_N, leaving thermal effects on the resistivity as a second-order phenomenon.

To deeply investigate the correlation between magnetic order and transport properties in the material, magnetoresistance measurements were performed on the same sample keeping the same orientation of the pellet with respect to the external

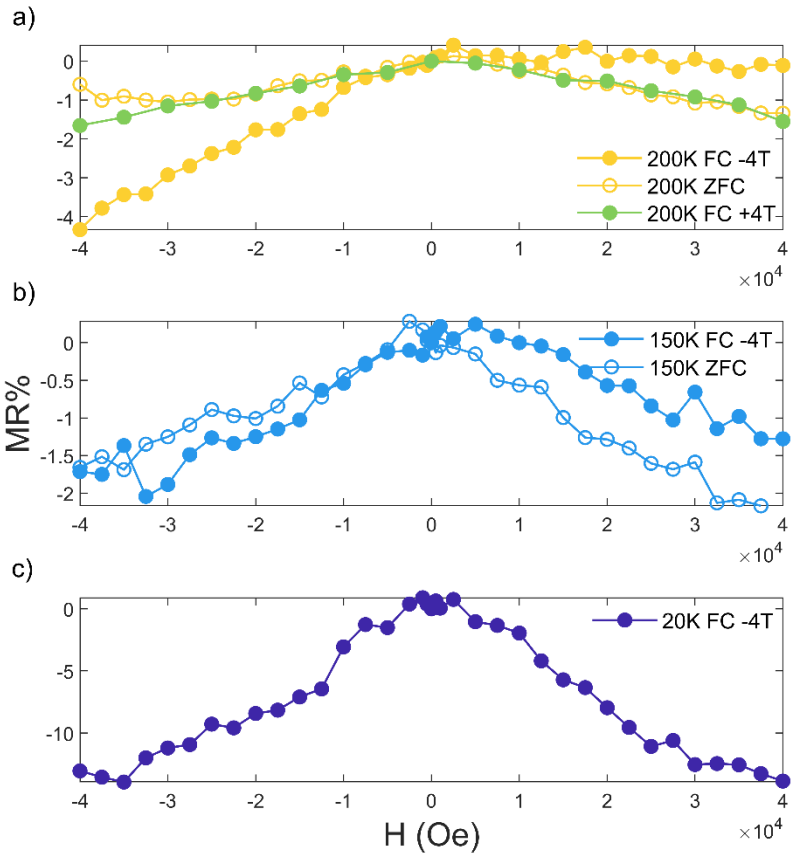

Figure 5-28 Magnetoresistance measurements collected between –40 kOe and 40 kOe in different thermal conditions and different field cooling protocols: a) at 200 K: after ZFC (empty dots), –40 kOe after FC (filled dots), +40 kOe after FC (filled green dots); b) at 150 K after ZFC (empty dots) and –40 kOe FC (filled dots); c) at 20 K after –40 kOe FC.

field. The magnetoresistance MR%, reported in Figure 5-28, has been calculated in percentage values as follows:

$$MR\%(H,T) = 100 \cdot \frac{\rho(H,T)-\rho(0,T)}{\rho(0,T)} \qquad (18)$$

where ρ(H,T) is the resistivity measured at temperature T in the applied magnetic field H, while ρ(0,T) is the value recorded without the applied field at the same T.

Magnetoresistance measurements have been performed by reaching the temperature setpoints with ZFC and FC protocols starting from RT, carrying out the FC branch with both positive and negative magnetic field ±40 kOe on cooling, then scanning the applied field from -40 kOe to +40 kOe during the measurement. While no effect is detected at RT, magnetoresistivity develops at temperatures below T_N. It is remarkable that the results also depend on the sign of the field applied on cooling. Specifically, at 200 K, ZFC-MR shows small MR effects with values

around 1.5% with almost symmetric branches at negative and positive scan fields. On the contrary, the FC-MR with –4T displays a large asymmetric MR effect with an increased loss of around 4.2% in magnitude at –40 kOe, around three times more intense than the ZFC-MR and, vice versa a quench of the MR for positive fields (Figure 5-28a). On the contrary, no effect of FC-MR at 4T with respect to the ZFC MR is detected (see Figure 5-28a, green dots). The same effects, even if much less intense, are detected also at 150 K (Figure 5-28b). Below the completion of the magnetic order process, no asymmetry is observed in the curves while the intensity of the MR effect is maximized, reaching 14% at ±40 kOe after FC at –40 kOe at 20 K (Figure 5-28c), a considerably high value with respect to other polycrystalline magnetoresistive perovskites [121].

These measurements pointed out that in isothermal conditions, across the stabilization of the magnetic order of the material between T_N and 150 K, the system responds differently with respect to the applied field sign, promoting carriers in the conduction band for negative fields and vice versa confining a minority portion of them in the valence band for positive fields. This evidence suggests a half-metallic nature of the compound with a transport mechanism driven by polarized carriers as it is observed for similar half-metallic materials [188]. Consequently, it can be argued that these polarized carriers may be characterized by a spin resultant prevalently oriented in the negative field direction. Moreover, because of this effect vanishes lowering T, the partial localization driven by the magnetic order and connected to the gradual stabilization of Mo-O bond length, acting in re-symmetrizing the conduction band by trapping the negatively polarized electrons at the B-site. As a result, in the very low field regime, below 150 K, the MR effect has a conventional behavior but with an increased intensity due to the larger confinement of the carriers, which is very sensitive to the application of a magnetic field which acts in promoting conductivity with enhanced yield, independently from its sign. Since magnetoresistance has already been investigated in PFMO samples with disorder on B site, but in that case, no asymmetric response with the sign of the magnetic field has been observed [184], the current observations point out the role of the cation order at the B site of the double perovskite (which means ordered distribution of Fe-O-Mo chains) as the driving force of the spin-polarized carriers half-metallicity of the material. In addition, even the intensity of the

magnetoresistance seems to depend on the cation order too as, particularly, at 20 K in B-ordered PFMO the absolute MR% is around 50% larger than B-disordered PFMO [184].

At this point, I want to sum up all the results for PFMO. The electrical properties of this double perovskite have been investigated as a function of temperature and external magnetic field. At RT PFMO is semi-metallic, with very low resistivity. Below T_N, the localization of a minority fraction of electrons at the Mo site is mainly driven by the long-range magnetic order process and determines an increase of the resistivity around 150 K. In this thermal regime, the system behaves as a half-metal, displaying asymmetric magneto-resistivity with polarized carriers promoted by negative magnetic fields and, vice versa, quenched MR for positive magnetic fields. Asymmetric magnetoresistance and half-metallicity are in PFMO cation-order related phenomena as they disappear once the Mo-O bond length stabilizes at lower temperatures, determining the completion of the ferrimagnetic resultant and the conclusion of the partial localization mechanism. Below this threshold, asymmetric magnetoresistivity is suppressed but record values of MR have been collected in the cation-ordered phase of PFMO with MR loss of 14% at 20 K, about 50% larger than in the disordered phase and an overall increase of the standard electrical resistivity. The interconnection between its magnetic and electrical properties allows to define PFMO as a proper multifunctional material while its spin-polarized carriers-half metallicity makes it a possible candidate for spintronic application.

The idea of a partial chemical substitution of lead with potassium in the novel KPFMO, to reduce the high conductivity of PFMO and hopefully switch to a dielectric character, will be discussed here below starting from its HP/HT synthesis.

5.3.2 Synthesis of KPFMO

KPFMO samples have been synthesised through solid-state reaction under HP/HT conditions by using the previously described Walker-type multi-anvil apparatus. Stoichiometric amounts of K_2CO_3 (99%, Carlo Erba Reagents), PbO (99%, Merck), Fe_2O_3 (99%, Merck), and MoO_3 (99.5%, Aldrich Chemicals) were

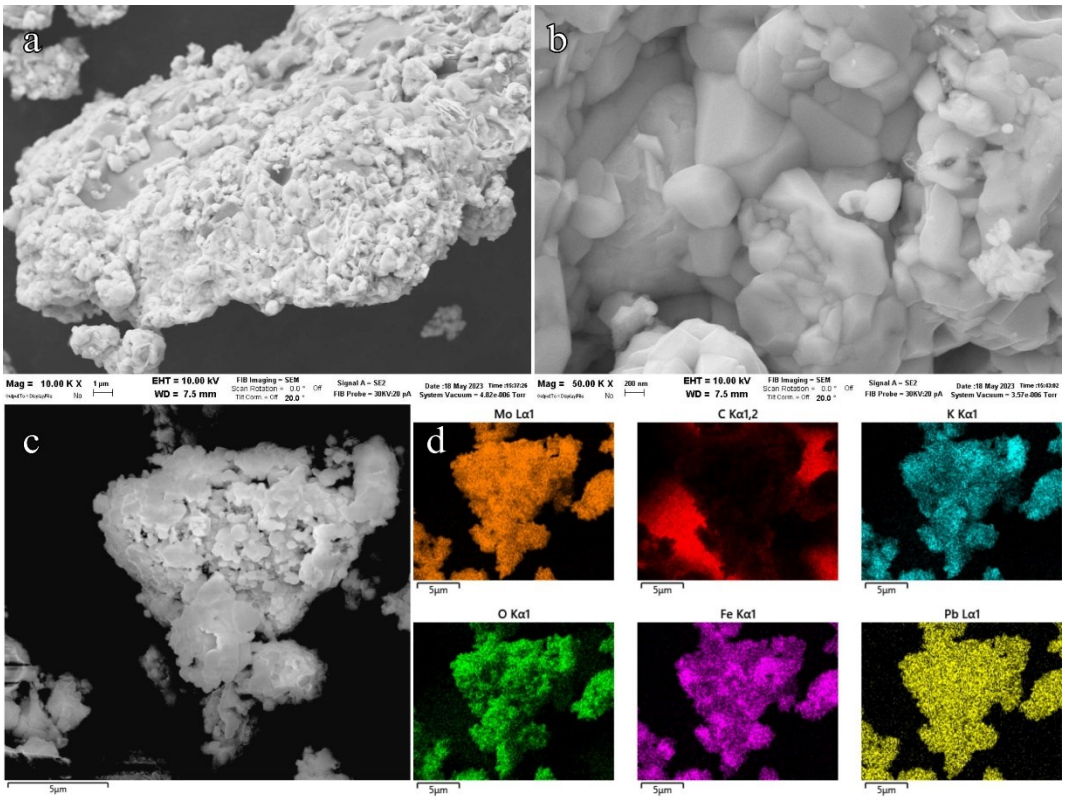

Figure 5-29 SEM analysis on KPFMO. Imaging mode at different magnifications (a-b) and EDX map (d) of (c).

ground and encapsulated into a platinum thin foil. Due to the hydrate tendency of K_2CO_3, it has been heated at 200°C for one hour before the reagents' preparation.

Taking PFMO as a reference, I have started to explore several pressure regimes for KPFMO synthesis, in order to stabilize the K^{+1} cation at the A site and obtain a pure perovskite phase. Contrary to PFMO, which completely crystallizes in the cubic perovskite structure at 5 GPa, KPFMO requires considerably higher pressure to be stabilized in a highly pure single crystallographic phase, close to 9.5 GPa. Despite some improvements that can be for sure done in reaching greater synthesis conditions, I will show you my results of a quite pure phase of KPFMO which I have synthesised at 1200°C and 9.5 GPa for 1 hour of reaction, with the conventional HP/HT synthesis protocol of Walker-type multianvil press.

5.3.3 Morphology

Firstly, the morphology and chemical composition analysis of this sample has been evaluated via SEM-EDX investigations, reported in Figure 5-29. KPFMO powdered samples seem to display a non-homogeneous morphology, as visible in

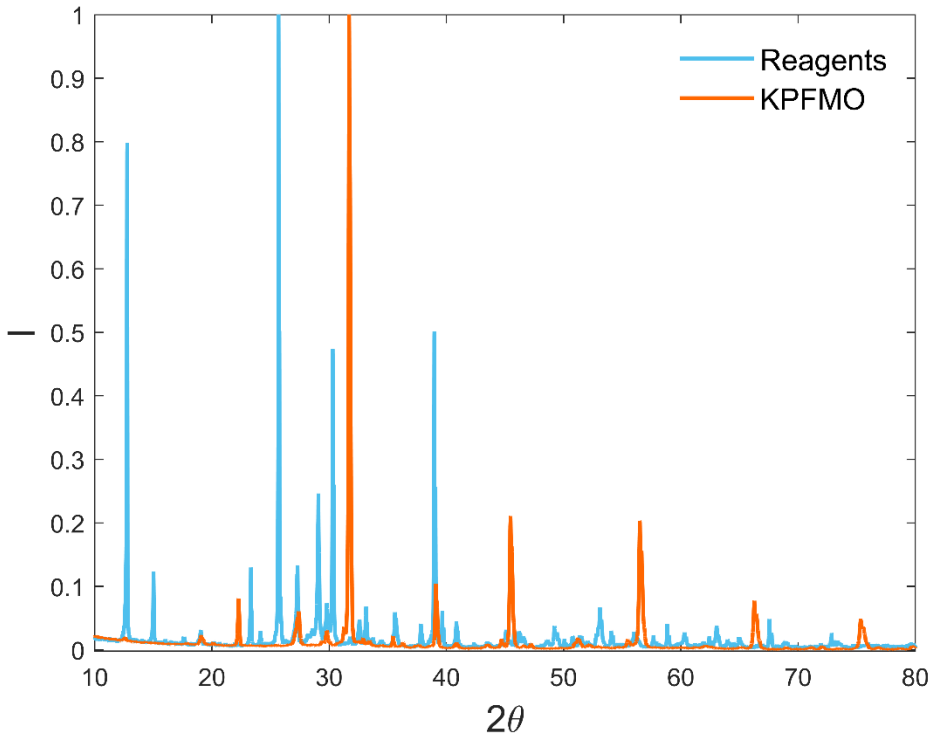

Figure 5-30 PXRD pattern of KPFMO (orange) and of the starting reagents (light blue).

Figure 5-29a and b. Namely, a particular texture of micrometric-shaped crystals is present on the surface of KPFMO grains, while a different smoother and quite uniform morphology is identified by looking at the larger grains. Unfortunately, EDX cannot be used to investigate the chemical composition related to these two different contributions, since the electron-matter interaction in such measurements comes from a quite deep volume of material and not only from the surface. However, EDX maps pointed out a quite good uniform distribution of all the atomic species, with a relative atomic percentage of K 11.1%, Pb 13.7%, Fe 9.2%, Mo 11.6%, and O 54.1%, showing some little but significant deviations from the expected 1:1:1:1:6 stoichiometric ratio. In particular, the obtained value for oxygen deficiency could be associated with a measurement artefact, due to the low capability of EDS to quantitatively evaluate low Z elements. Additionally, a reduced iron content could be associated with iron oxide impurities. Nevertheless, further investigations are mandatory to discriminate the contribution from surface and bulk to the chemical composition, for instance with TEM-EDX.

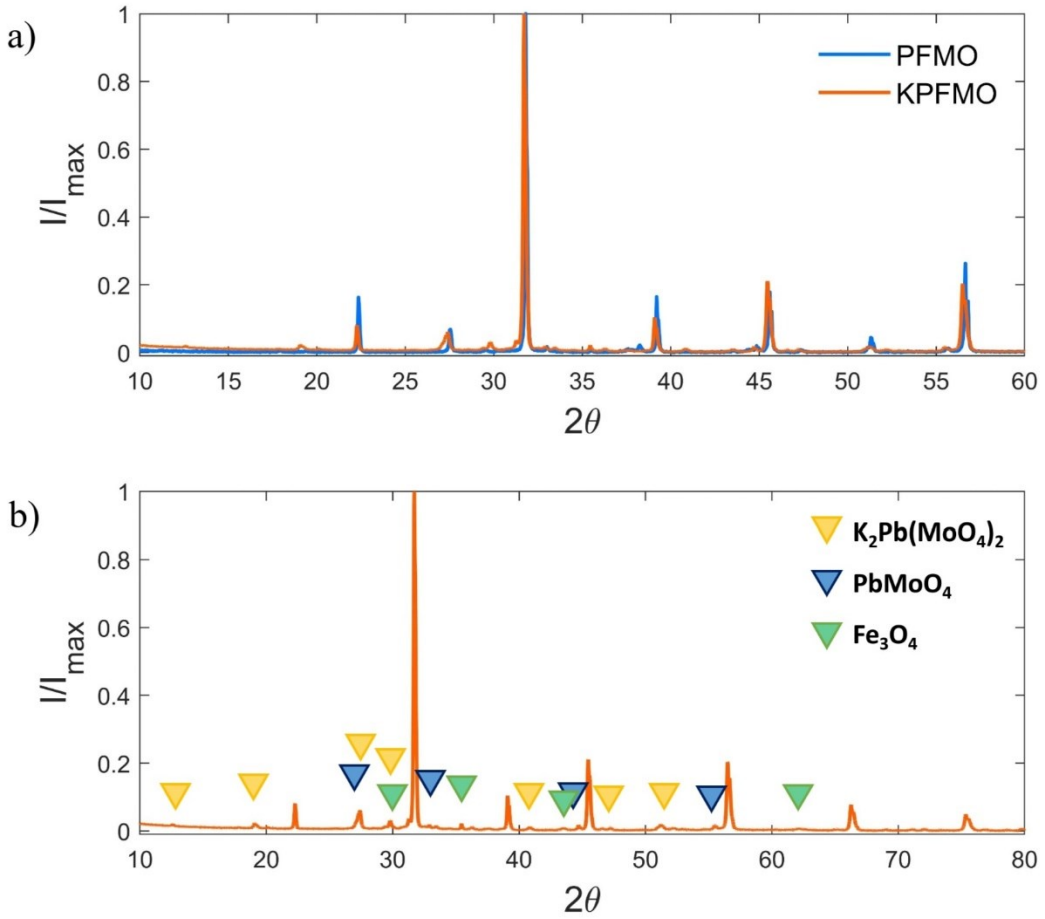

Figure 5-31 PXRD patterns of KPFMO (orange) superimposed to the one of PFMO (blue) (a). PXRD of KPFMO, highlighting the small reflections related to the identified spurious phases of $K_2Pb(MoO_4)_2$, $PbMoO_4$, and Fe_3O_4 (b).

5.3.4 Structural properties and first resolution attempts

In Figure 5-30 the PXRD acquired for the as-obtained KPFMO is shown, superimposed with the diffraction pattern of the powdered reagents in the stoichiometric amount before performing the reaction. The starting reagents mix has been indexed by considering the starting PbO (ICSD cod. 60135), Fe_2O_3 (ICSD cod. 40142), MoO_3 (ICSD cod.35076), and K_2CO_3 (ICSD cod. 662). However, impurities related to some hydrated potassium carbonate could be present in KPFMO phase but not easily detectable and associable to database references. A good crystallinity of the perovskite has been obtained, confirmed by a value of FWHM around 0.1 at the main reflection, and the contribution of both Cu-Kα1 and Cu-Kα2 clearly visible as a characteristic double-peak shape of the major reflections.

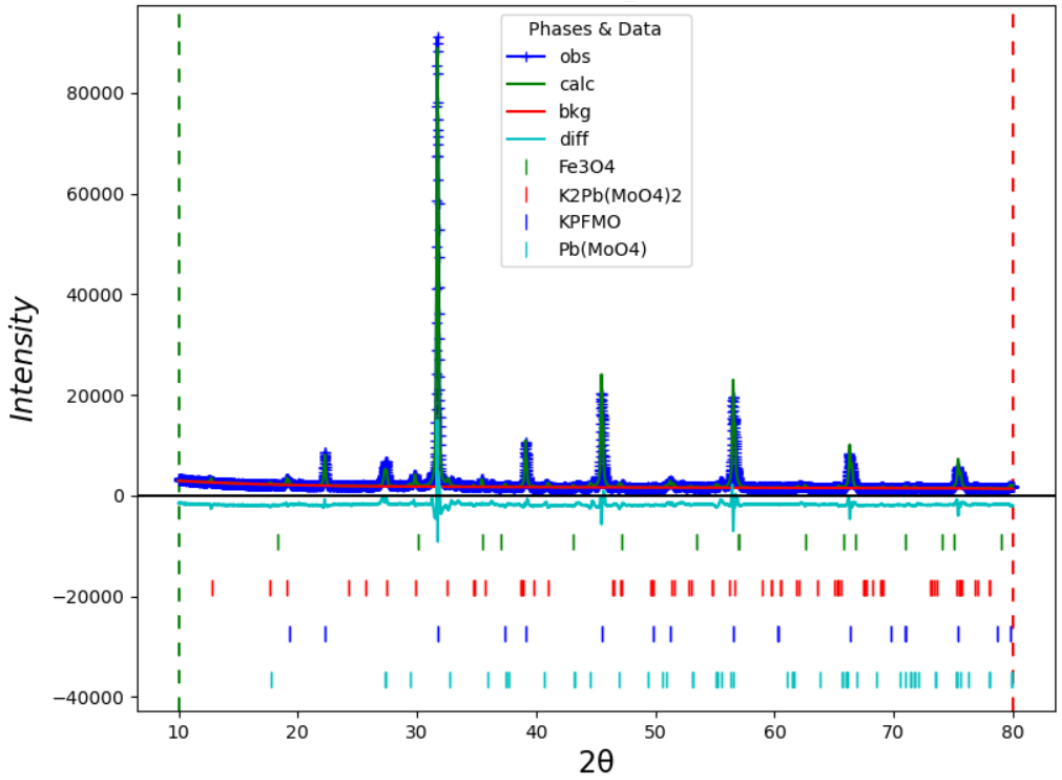

Figure 5-32 Rietveld refinement of KPFMO data, with the considered spurious phases.

In Figure 5-31a the comparison of recorded PXRD for PFMO and KPFMO samples is shown. Despite a modulation of some peak intensity, the two phases' reflections are quite well superimposed, suggesting that KPFMO could be isostructural to its parent compound with sole lead at the A site. Analyzing in-depth the diffraction pattern, I have identified the presence of spurious phases in the synthesized KPFMO, namely $Pb(MoO_4)$ (ICSD cod. 39137), $K_2Pb(MoO_4)_2$ (ICSD cod. 138657), and Fe_3O_4 (ICSD cod. 75627), as highlighted in Figure 5-31b, in which their principal reflections are reported. The presence of iron oxide is in agreement with the Fe deficiency revealed from SEM-EDS microanalysis.

Although further structural characterizations, such as TEM-SAED or NPD, are mandatory to properly solve the crystal structure of KPFMO, a tentative crystallographic model for this novel compound has been proposed. I have considered as a starting model the PFMO crystallographic information file previously published by my research group in ref. [41], by assuming it to be isostructural to my KPFMO, guided by the fact the two compounds seem to share the same diffraction peaks (see Figure 5-31a). Since any information about a possible cationic ordering at the A site is missing, I have considered K and Pb

species to occupy the same crystallographic site, as a reliable guess in case of disorder, neglecting potential non-equivalent sites. This assumption is reasonable comparing the two ionic radii of K^{+1} around 1.64 Å and Pb^{2+} around 1.49 Å. A preliminary Rietveld refinement has been performed on GSAS-II, in order to estimate the perovskite content with respect to the previously identified spurious phases. The atomic positions of each species, as well as the thermal parameters, have not been refined, as a preliminary process at this stage of structural analysis. The calculated pattern, overlapped with the experimental data, is reported in Figure 5-32. For the perovskite phase, the PFMO Fm-3m space group (225) has been retained for KPFMO, with a slight deviation for the lattice parameter, refined to be a = 7.9668 Å, instead of a = 7.9609 Å refined for PFMO [41]. No preferential orientation effects have been detected, trustworthy considering the cubic crystal system. Instead, as a term of intensity modulation, an equation constraint has been fixed for the total A site occupancy, equal to 0.25 for this specific crystallographic site, but with not necessarily equal occupancy between K and Pb. Indeed, the refined occupancy fractions values for the two species have been calculated to be 0.0787 and 0.1713, respectively. The stoichiometric ratio between K and Pb is thus estimated to be around 1:2, quite far away from the expected 1:1 proportion, but coherent with the other spurious phases considered in the refinement. Nevertheless, this calculation can be caused by artifacts depending on the fact that the crystallographic model is not completely definitive, and it is based on very strong assumptions.

Despite the fitting being quite good, the weighted residual profile and goodness of fit values are pretty high, namely R_{wp} = 11.8 and GOF = 5.82. However, again, it is only a starting point for a KPFMO crystal structure modelling and for this aim further investigations are needed, but a reliable indication of the perovskite content has been effectively estimated. Thus, the calculated weight fractions of all the spurious phases involved in the pattern indexing are 2.5%, 3.5%, and 4.5% for Fe_3O_4, $Pb(MoO_4)$, and $K_2Pb(MoO_4)_2$. Consequently, the estimation for the perovskite KPFMO phase content is around 89.5% wt, confirming that investigating further synthesis conditions can improve the sample quality, although good results have already been obtained.

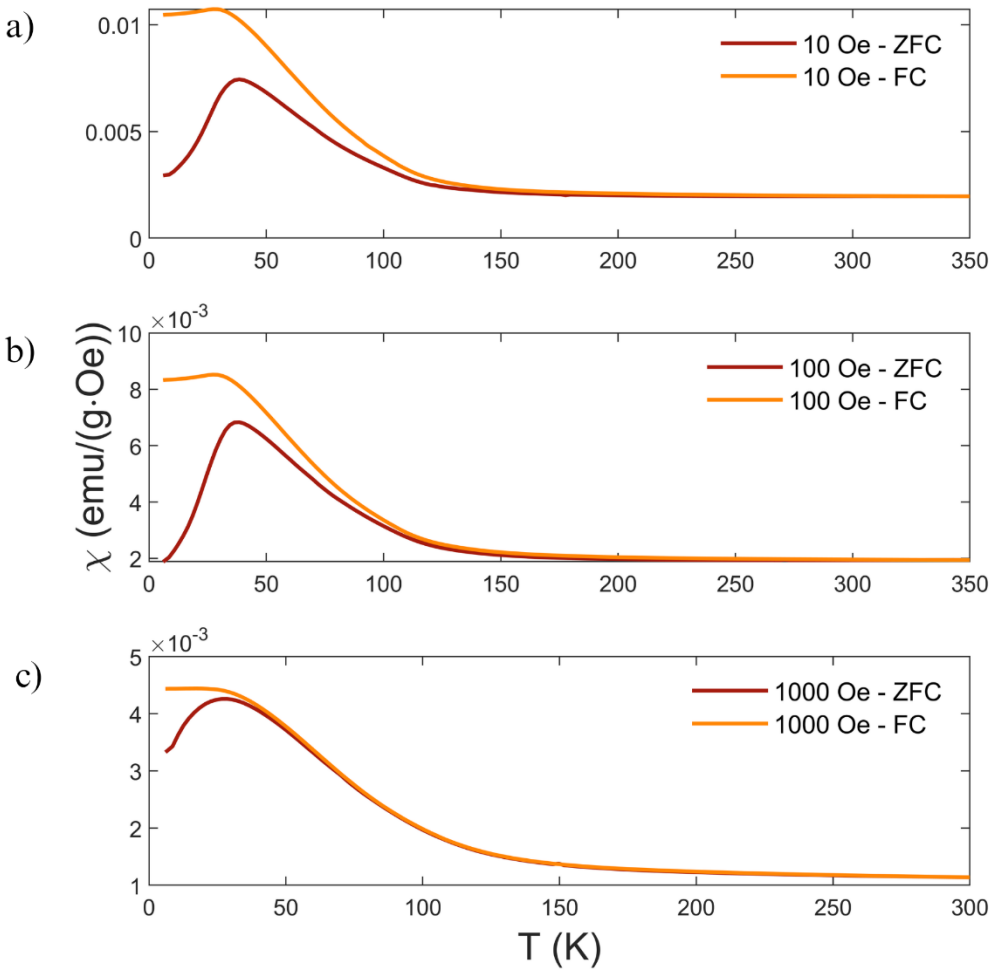

Figure 5-33 Susceptibility curves vs temperature of KPFMO sample acquired in FC and ZFC modes at 10 Oe (a), 100 Oe (b), and 1000 Oe (c).

5.3.5 Magnetic properties

The magnetism of KPFMO has been probed with SQUID magnetometry. In Figure 5-33 the susceptibility values recorded in ZFC and FC modes as a function of temperature are shown at various magnetic fields applied. Only one broad main magnetic transition is detected around 100 K, displaying a cuspid shape, notably in the ZFC acquisition mode and with a maximum magnetization value around 35 K, characteristic of AFM ordering. The discrepancy between ZFC and FC recorded data could be associated with a spin-glassy behaviour. Compared to the case of PFMO, the partial substitution of Pb^{+2} with K^{+1} has significantly changed the magnetic properties of the perovskite. However, from M(H) loops, recorded at 5 K, 60 K, and 300 K and reported in Figure 5-34 the presence of an FM-type phase already ordered at room temperature is clearly visible. This fingerprint can be

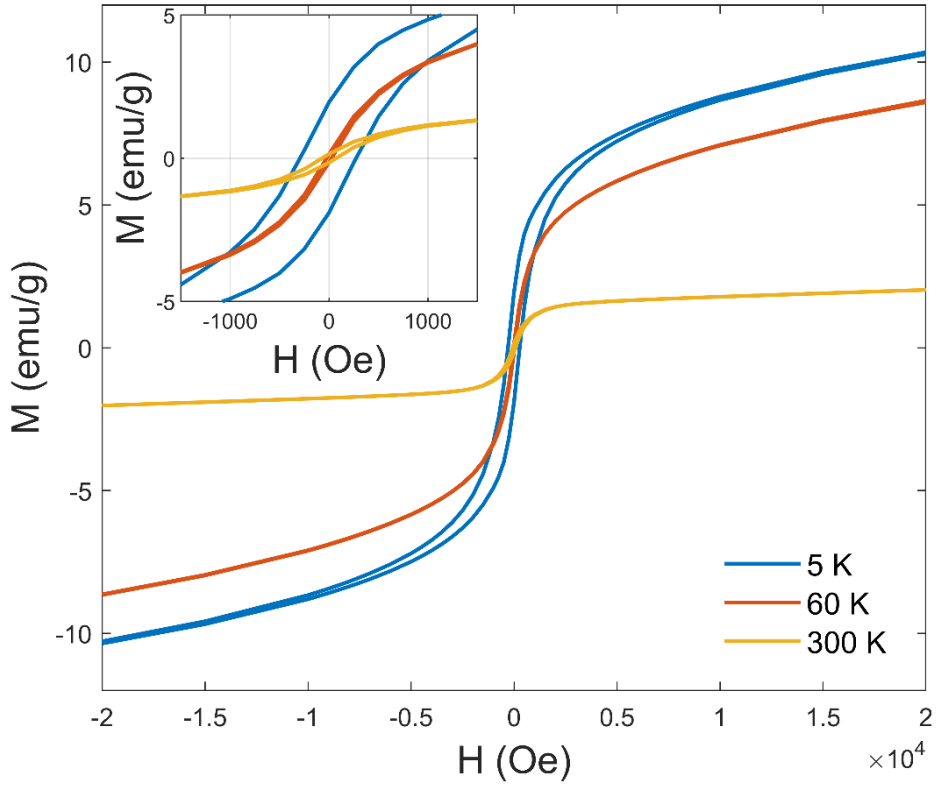

Figure 5-34 M(H) loops of KPFMO recorded at 5 K, 60 K, and 300 K in ZFC mode.

assigned to the presence of the ferrimagnetic Fe_3O_4, which displays a strong RT magnetic resultant and high Néel temperature at around 860 K [189], even though this spurious phase, identified from the structural characterizations, constitutes a very small fraction of the entire investigated sample. The size of this FM component is effectively coherent with the 2.5% weight fraction of Fe_3O_4 estimated from Rietveld refinement, corresponding to around 1 mg in the total mass of measured KPFMO powders (and impurities), equal to 41.2 mg. Since the magnetic saturation at 300 K of Fe_3O_4 has been reported to be around 55 emu/g from literature [190] [191], the amount of this spurious magnetic phase should contribute to a 2.2 emu/g, which is coherent with the observed 2.02 emu/g value at 2 T in Figure 5-34. The intrinsic AFM state of KPFMO, previously pointed out from M(T) curves, is superimposed to the strong magnetic contribution of the spurious phase, as visible from the non-saturated loops at both 60 K and 5 K. Noteworthy, such a high magnetic impurity contribution in the reported magnetic characterization does not allow a quantitative analysis on the magnetic properties of KPFMO. Hence, purer samples are needed for a deep understanding of the magnetism of this material.

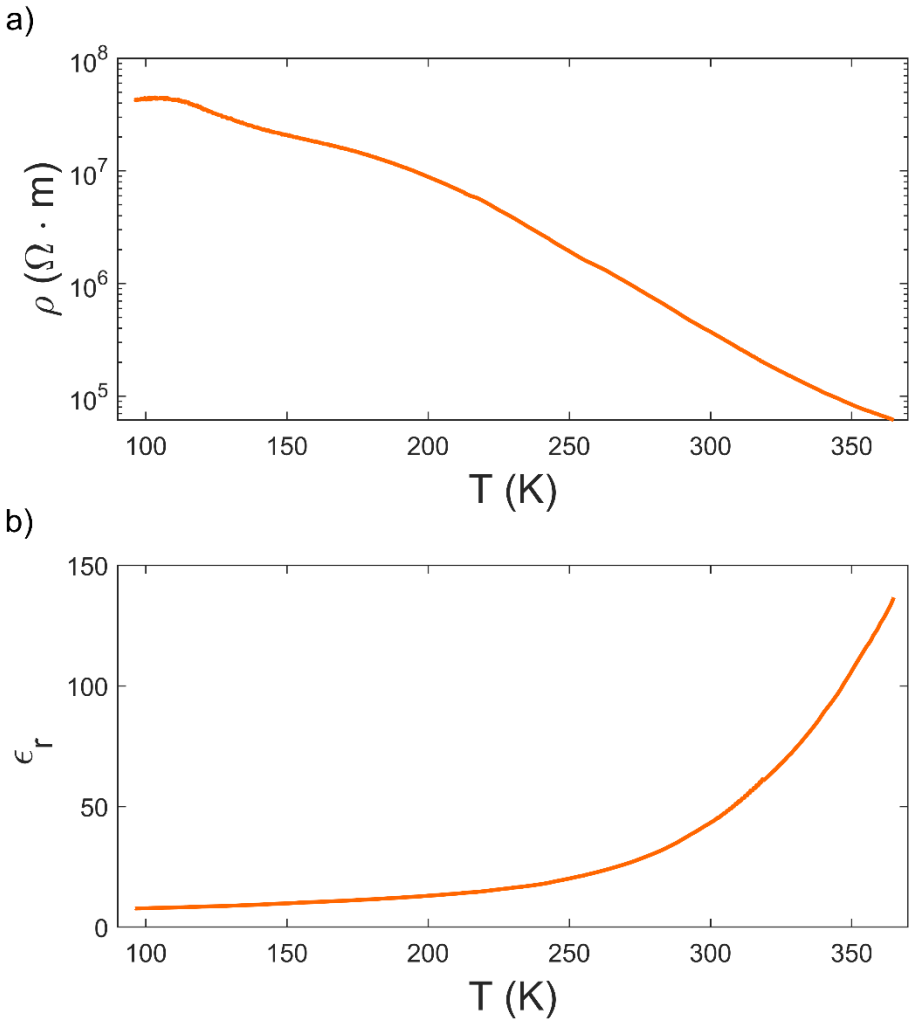

Figure 5-35 Resistivity (a) and relative permittivity constant measured at 1000 Hz (b) of KPFMO as a function of temperature.

5.3.6 Electric characterizations

The electric transport (two contacts configuration) and the dielectric character of KPFMO have been investigated in the thermal range between 370 and 90 K. The results are reported in Figure 5-35a and b, respectively. The resistivity, around 10^5 Ωm at room temperature, increases with a logarithmic trend by decreasing the temperature, getting closer to 10^8 Ωm values at around 100 K. Effectively KPFMO displays a quite good resistive character. Indeed, by comparing it with the electrical properties of its parent compound PFMO (see Paragraph 5.3.1), the partial introduction of potassium at the A site of the perovskite considerably increases the resistive nature of KPFMO of several order magnitudes, despite the

resistivity of the two compounds has been measured with different configurations (i.e. van der Pauw vs planar-plate). Considering its AFM ordering and electrical transport, KPFMO has lost the magnetoresistive behaviour which was detected in PFMO (see Paragraph 5.3.1). Moreover, KPFMO relative permittivity (Figure 5-35b), recorded at 1000 Hz, is higher than 100 at 350 K, and decreases to around 40 at room temperature, confirming the overall dielectric nature of this perovskite, at least below 250 K, where the ε_R starts to flatten and be almost invariant with temperature as expected for a capacitive system.

5.3.7 Conclusions on KPFMO

$KPbFeMoO_6$ perovskite has been presented in the previous paragraphs as a novel compound. Starting from the extensively studied Pb_2FeMoO_6, the partial chemical substitution of Pb^{2+} with K^{+1} cation at the A site has been revealed effectively as a good solution to tune and tailor the PFMO magnetic and electrical properties. Specifically, KPFMO has been synthesized under HP/HT conditions, in which the effect of the pressure plays a crucial role in order to stabilize the potassium cation at the A site of the perovskite. Preliminary structural investigations suggest a possible isostructural crystallographic cubic system for KPFMO to its parent compound with lead only at the A site. From this tentative refinement, a K:Pb ratio of about 1:2 has been estimated, which is consistent with the indexed spurious phases. On the contrary, the insertion of K^{+1} has strongly influenced the magnetism, switching from the high-temperature long-range ferrimagnetic ordering, with T_N at about 275 K of PFMO to the antiferromagnetism displayed at around 50 K of KPFMO. Although the near RT ordering has been lost, KPFMO electrical properties radically changed from the high conductivity intrinsic of PFMO. Indeed, the system moves from semi-metallicity towards dielectricity, with a significant increase in the resistivity constant and a capacitive behavior below 250 K. A possible solution to fine-tuning the physical properties, aiming at the coexistence of a high temperature magnetic state and a dielectric nature, could be the exploration of the $K_{1-x}Pb_xFeMoO_6$ solid solutions.

Nevertheless, further characterizations are mandatory to clarify many features of KPFMO, starting from the crystalline structure. Namely, in order to properly solve the crystallographic symmetry, the combination of complementary

structural characterizations, such as TEM-SAED and neutron powder diffraction, as in the case of BCMO, is required, getting information also about the stoichiometry and eventual cationic ordering. Moreover, some improvements can be made also on the purity level obtainable, by exploring more HP/HT synthesis conditions, needed also to remove the presence of spurious phases (at least the magnetic one) to allow a proper characterization of the magnetic character and properties of the system.

5.4 Ongoing publications

Synthesizing a novel compound and performing, at least, the standard characterization of its physical properties, with the relative discussion, requires a non-negligible amount of time. Consequently, I want to cite the ongoing publications coming from my experimental work discussed in this Chapter, which, unfortunately, have not yet been published. Specifically, an upcoming scientific publication, which I have recently finalized as first and corresponding author, deals with the electric and magnetoelectric characterizations of PFMO (reported here in Paragraph 5.3.1) and it is, up to now, under final revision from the submitted journal. Another work, the one that holds the stronger emotional attachment to me, is in preparation regarding the synthesis and characterization of the novel $BiCu_{0.5}Mn_{0.5}O_3$ (reported in Paragraph 5.2) and it will be submitted, hopefully, in the following weeks. On the contrary, a few months more I think will be required in order to properly investigate KPFMO or other intermediate members of BCMO solid-solution, and thus finalize the relative scientific publications.

Moreover, during the long period of my PhD activity, I had the opportunity to work not only on perovskite systems or on high pressure techniques, being part of some side projects, from various fields and topic, in which my contribution has been helpful and has resulted in scientific publications. Engaging with multiple disciplines not only enriched my multidisciplinary academic experience but also equipped me with versatile skills to tackle multifaceted challenges in innovative ways. In the final Appendix section, I will provide a brief description of these research papers' topics and in which terms I have been involved.

6 Conclusions

This chapter summarizes my research activities during my doctorate in Materials Science and Technology at the University of Parma carried out at the Institute of Materials for Electronics and Magnetism (IMEM) of the National Research Council (CNR).

My PhD activity has been focused on the investigation of functional materials with perovskite structures, which have garnered significant interest within the scientific community, both in terms of fundamental exploration and applied research. Particularly, I dealt with the synthesis and investigation of potential multiferroic perovskites, compounds distinguished by the coexistence of multiple ferroic orders, aiming to achieve the synergy between ferromagnetism and ferroelectricity. However, the spontaneous occurrence of these two primary orders is exceptionally rare in nature, due to strong structural and physical constraints preventing the simultaneous presence of these two phenomenologies. As a result, the adoption of unconventional methods, such as high pressure/high temperature (HP/HT) synthesis, is often needed to force the stabilization of multifunctional artificial phases.

In this framework, I have investigated the prospect of creating novel bulk multifunctional materials by performing chemical substitutions on known double perovskite structures previously examined in the literature, by HP/HT solid-state reactions, exploiting the versatility of the crystallographic structure to accommodate structural distortions. In order to achieve the multiferroicity, I have tried to merge in such compounds ferroelectricity and ferromagnetism by splitting these two contributions on the two distinct (A and B) sites of the perovskite. Namely, Bi^{3+} or Pb^{2+} cations have been introduced at the A-site, since their stereochemical effect can lead to a net electric dipole formation, while at the B-site

the magnetism has been promoted by the insertion of transition metals from III-IV period, with partially filled d-shells. Moreover, the combination of two different cations at the B site allows to explore different super-exchange interaction mechanisms, which result in particular macroscopic magnetic ordered states in $A_2B'B''O_6$ ordered or in $AB'_{0.5}B''_{0.5}O_3$ disordered double perovskites. Recognizing the pivotal role of crystallographic structure analysis in maximizing the potential of these compounds, I have dedicated significant efforts over these years to the study of structural characterization techniques. This has allowed me to gain a comprehensive understanding of their potentialities and peculiarities, especially in relation to the type of probe employed, such as X-rays, electrons, and neutrons. As a consequence, I immersed myself in the intricate processes of structural resolution and refinement.

In this PhD thesis, I presented the results related to the synthesis and structural, magnetic, and electrical characterization of two newly synthesized perovskites, namely $BiCu_{0.5}Mn_{0.5}O_3$ (BCMO) and $KPbFeMoO_6$ (KPFMO), described in detail in Paragraphs 5.2 and 5.3, respectively.

BCMO displays an orthorhombic structure with a Pbam centrosymmetric space group. The distortion of the octahedral scheme is attributed to the stereochemical effect of Bi^{3+}. Cationic disorder was detected at the B site, even though compositional inhomogeneities have been revealed in the mesoscale distribution of Cu^{2+} and Mn^{4+} species, resulting in the absence of long-range magnetic orderings. This system displays a correlation between the magnetic and the electrical properties, since both magnetically ordered states and transport mechanisms concomitantly evolve in temperature probably guided by a partial localization of the electrons on Mn sites. Indeed, BCMO is paramagnetic at high temperatures, undergoing a weak FM-like transition at around 320 K, with significant room temperature spontaneous magnetization and high polarizability. In the high temperature regime, the compound displays bad conductive behaviour with a thermally activated electrical transport characterized by E_A= 0.26 eV. When the FM-like state saturates, the partial electron localization leads to different Mn^{4+} coordinations and to the formation of a minority Mn^{3+} population, causing a shift from a standard thermally activated semiconductive behaviour to a 3D variable

range hopping model. In the low-temperature regime, at about 50 K, complete electron localization associates with a spin-glassy or mesoscale antiferromagnetic order, possibly leading to a dielectric state. By comparing BCMO with the parent compound $BiFe_{0.5}Mn_{0.5}O_3$(BFMO), which inspires its conceptualization and synthesis, the chemical substitution of Cu^{2+} for Fe^{3+} cation resulted in significant modifications of structural, magnetic, and electrical properties. While the characteristic antiferroelectric arrangement with the possibility to induce ferroelectricity through a proper external bias of BFMO is lost, BCMO exhibited an increased magnitude of the FM-like state observed at high T, and the transition onset was shifted, resulting in potentially more interesting magnetic properties for technological applications. Moreover, preliminary results demonstrated an additional degree of tunability and a further improvement of the room-temperature magnetism obtainable by exploring different compositions of $BiCu_{1-x}Mn_xO_3$. solid solution.

KPFMO exhibited completely distinct features. This new perovskite derives from the parent compound Pb_2FeMoO_6 (PFMO), whose magnetoelectrical properties have been studied and reported in Paragraph 5.3.1, and shows effective tuning of magnetic and electrical properties by partially substituting Pb^{2+} with K^+ at the A site. Although KPFMO seems to exhibit isostructural characteristics to PFMO, the introduction of potassium alters the magnetic properties, from PFMO's high temperature ferrimagnetic ordering to less interesting antiferromagnetism at around 50 K. As a positive countereffect, KPFMO undergoes a significant shift in its electrical behaviour with respect to PFMO, moving from PFMO high conductivity to a more resistive behaviour, behaving as dielectric below 250 K.

Unfortunately, the investigation of BCMO and KPFMO properties has unveiled the impossibility of the coexistence of ferroelectricity and ferromagnetism for both these materials; thereby multiferroism in these compounds is ruled out for complementary reasons. Nevertheless, they have revealed interesting physical properties and the comprehensive physical characterizations enable to define them as proper functional materials.

In conclusion, the research outlined in this thesis unveils promising perspectives for future exploration of BCMO and KPFMO, along with their

respective solid solutions, and beyond, with the possibility to exploit chemical substitutions and unconventional synthesis techniques to significantly modify the properties of perovskites, owing to the versatility of this crystallographic structure.

Appendix

A. Graphene-based magnetocaloric composites for energy conversion

Authors: Chiara Coppi, Francesco Cugini, Giacomo Magnani, Chiara Milanese, Lucia Nasi, Laura Lazzarini, Daniele Pontiroli, Mauro Riccò, Massimo Solzi

DOI: https://doi.org/10.1002/adem.202200811

This study is mainly related to my Master Thesis' project, born from an intriguing idea to try something new. In this work, we presented a simple, versatile, and cost-effective method to fabricate innovative thermal conductive magnetocaloric composites, that offers a solution to overcome the actual thermal and mechanical limits of the most studied magnetocaloric materials. The composites were prepared by mixing powder of a magnetocaloric material and an epoxy binder matrix enriched by a graphene-based material, obtained by thermal exfoliation of graphite oxide. The final graphene-enriched composites showed a significant improvement of the magnetocaloric time-response to the magnetic field, due to the formation of a 3D network that bridges the magnetocaloric particles and reduces the metal-matrix contact resistance, thus creating a percolation path for an efficient heat transfer. Because of the simplicity and scalability of the preparation method and the great enhancement in response time, these new functional composites represent an important step for the effective application of magnetocaloric materials in thermomagnetic devices for the energy conversion. In this framework, I had the chance to handle all this complete study, starting from the sample's preparation, passing through the evaluation of the thermal evolution by

performing finite-elements simulations, ending with all the physical characterizations of the composites.

B. High-Pressure Bulk Synthesis of InN by Solid-State Reaction of Binary Oxide in a Multi-Anvil Apparatus

Authors: Elena Del Canale, Lorenzo Fornari, Chiara Coppi, Giulia Spaggiari, Francesco Mezzadri, Giovanna Trevisi, Patrizia Ferro, Edmondo Gilioli, Massimo Mazzer, Davide Delmonte

DOI: https://doi.org/10.1021/acs.inorgchem.3c00231

This work is closer to my actual research activity, as we have presented a new method to synthesize bulk indium nitride by means of a simple solid-state chemical reaction carried out under hydrostatic high-pressure/high-temperature conditions in a multi-anvil apparatus, not involving gases or solvents during the process. The reaction occurs between the binary oxide In_2O_3 and the highly reactive Li_3N as the nitrogen source, in the powder form. The formation of the hexagonal phase of InN, occurring at 350 °C and $P \geq 3$ GPa, was successfully confirmed by powder X-ray diffraction, with the presence of Li2O as a unique byproduct. A simple washing process in weak acidic solution followed by centrifugation allowed us to obtain pure InN polycrystalline powders as a precipitate. With an analogous procedure, it was possible to obtain pure bulk GaN, from Ga_2O_3 and Li_3N at temperatures higher than 600 °C and pressures greater than 2.5 GPa. These results pointed out, particularly for InN, a clean, and innovative way to produce significant quantities of one of the most promising nitrides in the field of electronics and energy technologies. In this framework, I have performed the solid-state reactions carried out with the Walker-type multianvil press employed also to synthetise my perovskites.

C. Factors associated with delirium in a real-world acute-care setting: analysis considering the interdependence of clinical variables with the frailty syndrome

Authors: Andrea Ticinesi, Alberto Parise, Davide Delmonte, Chiara Coppi, Beatrice Prati, Nicoletta Cerundolo, Angela Guerra, Antonio Nouvenne, Tiziana Meschi

Accepted for publication in January 2024
(manuscript EGEM-D-23-00567R2)

This paper has resulted from an interesting and unexpected collaboration with a group of doctors from the Department of Medicine and Surgery of University of Parma. We have evaluated the delirium risk, a specific medical condition of acute confusion, within a clinical set of around 600 geriatric patients. This acute-care setting generally does not consider the presence of frailty. The objective of our retrospective study was to identify factors associated with delirium, considering the interdependency of clinical variables with frailty in complex older patients. The clinical records of all the participants were reviewed, with collection of clinical, anamnestic and pharmacological data. The correlations of exposure variables with delirium and its subtypes were investigated selecting variables not showing a high overlap with frailty, and fixing correlations associated with 25% excess of frequency in comparison with the average of the population as statistically significant. In this work, my scientific contribution is related with the data treatment. Indeed, this analysis has been carried out by writing a specific script on Matlab software to proper handle and discriminate significant data and correlations. Delirium was detected in the 20% of participants. The presence of one among age>85 years old, frailty CFS>4 and invasive devices, occurring in 72% of participants, explained 95% of delirium cases. The main factors maximizing delirium incidence were dementia, other psychiatric conditions, chronic antipsychotic treatment, and invasive devices. The coexistence of three of these

parameters was associated with a peak frequency of delirium ranging from 57% to 61%. All of these conditions were more associated with hypoactive than hyperactive specific forms of delirium. In an acute-care setting, the presence of frailty, in addition to older age and use of invasive devices, maximized delirium incidence. At the individual patient level, dementia and use of antipsychotics remained important risk factors. In conclusion, we have observed that modern clinical prediction tools for delirium should account for frailty.

References

[1] A. K. Rajagopal and R. Srinivasan, “Lattice dynamics of cubic perovskite structures, in particular SrTiO3,” *Journal of Physics and Chemistry of Solids,* vol. 23, no. 6, pp. 633-638, 1962.

[2] S. Hirotsu, J. Harada, M. Iizumi and K. Gesi, “Structural Phase Transitions in CsPbBr3,” *Journal of the Physical Society of Japan,* vol. 37, no. 5, pp. 1393-1398, 1974.

[3] E. L. da Silva, J. M. Skelton, S. C. Parker and A. Walsh, “Phase stability and transformations in the halide perovskite CsSnI3,” *Phys. Rev. B,* vol. 91, no. 14, p. 144107, 2015.

[4] V. M. Goldschmidt, “Geochemische Verteilungsgesetze der Elemente”, Oslo: Skrifter Norske Videnskaps, 1926.

[5] C. Li, K. C. Kwan Soh and P. Wu, “Formability of ABO3 perovskites,” *Journal of Alloys and Compounds,* vol. 372, no. 1-2, pp. 40-48, 2004.

[6] M. R. Filip and F. Giustino, “The geometric blueprint of perovskites,” *PNAS,* vol. 115, no. 21, pp. 5397-5402, 2018.

[7] C. Ye, J. Yang, L. Yao and N. Chen, “Regularities of formation and lattice distortion of perovskite-type compounds.,” *Chin.Sci.Bull.,* vol. 47, p. 458–460, 2002.

[8] Q. Sun and W.-J. Yin, “Thermodynamic Stability Trend of Cubic Perovskites,” *Journal of the American Chemical Society,* vol. 139, no. 42, pp. 14905-14908, 2017.

[9] A. Kumar, A. S. Verma and S. R. Bhardwaj, “Prediction of Formability in Perovskite-Type Oxides,” *The Open Applied Physics Journal,* vol. 1, no. 1874-1835, pp. 11-19, 2008.

[10] W. Eerenstein, N. Mathur and J. Scott, “Multiferroic and magnetoelectric materials.,” *Nature,* vol. 442, p. 759–765, 2006.

[11] J. L. Clabel Huamán, V. A. Garcia Rivera, A. H. Pinto and E. Marega, Multiferroic perovskite ceramics: Properties and applications, Series in Advanced Ceramic Materials, Perovskite Ceramics, 2023, pp. 339-381.

[12] P. Barone, B. Sanyal and S. Picozzi, “Multiferroics: theory, mechanisms, and materials,” *Science and Technology of Atomic,*

Molecular, Condensed Matter & Biological Systems,, vol. 2, pp. 129-161, 2012.

[13] X. Liang, H. Chen and N. X. Sun, "Magnetoelectric materials and devices," *APL Mater,* vol. 9, no. 4, p. 041114, 2021.

[14] S. Dong, H. Xiang and E. Dagotto, "Magnetoelectricity in multiferroics: a theoretical perspective," *National Science Review,* vol. 6, no. 4, pp. 629-641, 2019.

[15] N. Spaldin and R. Ramesh, "Advances in magnetoelectric multiferroics.," *Nature Mater,* vol. 18, p. 203–212, 2019.

[16] T.-Y. Cai and Z.-Y. Li, "The effect of the itinerant spin-polarized carriers on magnetization in double-perovskite ferrimagnet Sr2FeMoO6," *Journal of Physics: Condensed Matter,* vol. 16, no. 21, p. 3737, 2004.

[17] "Magnetostriction and thermal expansion anomalies near the Curie point of the compound La0.7Sr0.3MnO3 with the perovskite structure," *Jetp Lett,* vol. 65, p. 474–478, 1997.

[18] K. Kobayashi, T. Kimura, H. Sawada, K. Terakura and Y. Tokura, "Room-temperature magnetoresistance in an oxide material with an ordered double-perovskite structure," *Nature,* vol. 395, no. 6703, pp. 677-680, 1998.

[19] R. Nechache, C. Harnagea, S. Li, L. Cardenas, W. Huang, J. Chakrabartty and F. Rosei, "Bandgap tuning of multiferroic oxide solar cells," *Nature Photonics,* vol. 9, no. 1, pp. 61-67, 2015.

[20] I. Grinberg, D. V. West, M. Torres, G. Gou, D. M. Stein, L. Wu, G. Chen, E. M. Gallo, A. R. Akbashev, P. K. Davies, J. E. Spanier and A. M. Rappe, "Perovskite oxides for visible-light-absorbing ferroelectric and photovoltaic materials," *Nature,* vol. 503, no. 7477, pp. 509-512, 2013.

[21] Y. Xu, J. Dhainaut, J.-P. Dacquin, A.-S. Mamede, M. Marinova, J.-F. Lamonier, H. Vezin, H. Zhang and S. Royer, "La1-x(Sr, Na, K)xMnO3 perovskites for HCHO oxidation: The role of oxygen species on the catalytic mechanism," *Applied Catalysis B: Environmental,* vol. 287, p. 119955, 2021.

[22] R. Phatak, S. K. Gupta, K. Krishnan, S. K. Sali, S. V. Godbole and A. Das, "Crystallographic site swapping of La3+ ion in BaA′LaTeO6 (A′ = Na, K, Rb) double perovskite type compounds: diffraction and photoluminescence evidence for the site swapping," *Dalton Trans.,* vol. 43, no. 8, pp. 3306-3312, 2014.

[23] H. Falcón, J. A. Barbero, G. Araujo, M. T. Casais, M. J. Martínez-Lope, J. A. Alonso and J. L. G. Fierro, "Double perovskite oxides A2FeMoO6−δ (A=Ca, Sr and Ba) as catalysts for methane combustion," *Applied Catalysis B: Environmental,* vol. 53, no. 1, pp. 37-45, 2004.

[24] Y. Li, X. P. Gao, G. R. Li, G. L. Pan, T. Y. Yan and H. Y. Zhu, "Titanate Nanofiber Reactivity: Fabrication of MTiO3 (M = Ca, Sr, and Ba) Perovskite Oxides," *J. Phys. Chem. C,* vol. 113, no. 11, pp. 4386-4394, 2009.

[25] H. S. Bhatti, S. T. Hussain, F. A. Khan and S. Hussain, "Synthesis and induced multiferroicity of perovskite PbTiO3; a review," *Applied Surface Science,* vol. 367, pp. 291-306, 2016.

[26] E. Solana-Madruga, C. Ritter, C. Aguilar-Maldonado, O. Mentré, J. P. Attfield and A. M. Arévalo-López, "Mn3MnNb2O9: high-pressure triple perovskite with 1 : 2 B-site order and modulated spins," *Chem. Commun.,* vol. 57, no. 68, pp. 8441-8444, 2021.

[27] X. Kang, R. Ishikawa, A. A. Belik, Y. Tsujimoto, M. Arai, S. Kawata and K. Yamaura, "Cd2FeReO6: A High-TC Double Perovskite Oxide with Remarkable Tunneling Magnetoresistance," *Inorg. Chem.,* vol. 62, no. 45, pp. 18474-18484, 2023.

[28] N. Özbay and R. Z. Y. Şahin, "Preparation and characterization of LaMnO3 and LaNiO3 perovskite type oxides by the hydrothermal synthesis method," *AIP Conference Proceedings,* vol. 1809, no. 1, p. 020040, 2017.

[29] A. A. Belik, K. Komada, N. Igawa, S. Shamoto, K. Kosuda and E. Takayama-Muromachi, "Crystal and Magnetic Structures and Properties of BiMnO3+δ," *J. Am. Chem. Soc.,* vol. 132, no. 23, pp. 8137-8144, 2010.

[30] T. Ishihara, H. Matsuda and Y. Takita, "Effects of rare earth cations doped for La site on the oxide ionic conductivity of LaGaO3-based perovskite type oxide," *Solid State Ionics,* vol. 79, no. 0167-2738, pp. 147-151, 1995.

[31] M. Azuma, H. Hojo, K. Oka, H. Yamamoto, K. Shimizu, K. Shigematsu and Y. Sakai, "Functional Transition Metal Perovskite Oxides with 6s2 Lone Pair Activity Stabilized by High-Pressure Synthesis," *Annual Review of Materials Research,* vol. 51, pp. 329-349, 2021.

[32] X. Liang, W. Yan, Y. Yu, K. Zhang, W. An, H. Chen, Y. Zou, X. Zhao and X. Zou, "Electrocatalytic Water Oxidation Activity-Stability Maps for Perovskite Oxides Containing 3d, 4d and 5d Transition Metals," *Angew. Chem. Int. Ed.,* vol. 62, no. 46, 2023.

[33] K. Leng, Q. Tang, Y. Wei, L. Yang, Y. Xie, Z. Wu and X. Zhu, "Recent advances in Re-based double perovskites: Synthesis, structural characterization, physical properties, advanced applications, and theoretical studies," *AIP Advances,* vol. 10, no. 12, p. 120701, 2020.

[34] S. Royer, D. Duprez, F. Can, X. Courtois, C. Batiot-Dupeyrat, S. Laassiri and H. Alamdari, "Perovskites as Substitutes of Noble Metals for Heterogeneous Catalysis: Dream or Reality," *Chem. Rev.,* vol. 114, no. 20, pp. 10292-10368, 2014.

[35] H. Sun, G. Chen, Y. Zhu, B. Liu, W. Zhou and Z. Shao, "B-Site Cation Ordered Double Perovskites as Efficient and Stable Electrocatalysts for Oxygen Evolution Reaction," *Chem. Eur. J.,* vol. 23, no. 24, pp. 5722-5728, 2017.

[36] S. Vasala and M. Karppinen, "A2B′B″O6 perovskites: A review," *Progress in Solid State Chemistry,* vol. 43, no. 1–2, pp. 1-36, 2015.

[37] Z. J. L. Bare, R. J. Morelock and C. B. Musgrave, “Dataset of theoretical multinary perovskite oxides,” *Sci Data,* vol. 10, no. 1, p. 244, 2023.

[38] M. T. Anderson, K. B. Greenwood, G. A. Taylor and K. R. Poeppelmeier, “B-cation arrangements in double perovskites,” *Progress in Solid State Chemistry,* vol. 22, no. 3, pp. 197-233, 1993.

[39] K. Tezuka, K. Henmi, Y. Hinatsu and N. M. Masaki, “Magnetic Susceptibilities and Mössbauer Spectra of Perovskites A2FeNbO6 (A=Sr, Ba),” *Journal of Solid State Chemistry,* vol. 154, no. 2, pp. 591-597, 200.

[40] D. E. Cox, G. Shirane and B. C. Frazer, “Neutron-Diffraction Study of Antiferromagnetic Ba2CoWO6 and Ba2NiWO6,” *Journal of Applied Physics,* vol. 38, no. 3, pp. 1459-1460, 1967.

[41] F. Mezzadri, D. Delmonte, F. Orlandi, C. Pernechele, G. Calestani, M. Solzi, M. Lantieri, G. Spina, R. Cabassi, F. Bolzoni, M. Fittipaldi, M. Merlini, A. Migliori, P. Manuel and E. Gilioli, “Structural and magnetic characterization of the Pb2FeMoO6,” *Journal of Materials Chemistry C,* vol. 4, pp. 1533-1542, 2016.

[42] J. Rodrìguez-Carvajal, M. Hennion, F. Moussa, A. H. Moudden, L. Pinsard and A. Revcolevschi, “Neutron-diffraction study of the Jahn-Teller transition in stoichiometric LaMnO3,” *Phys. Rev. B,* vol. 57, no. 6, pp. R3189--R3192, 1998.

[43] S. Geller, “Crystal Structure of Gadolinium Orthoferrite, GdFeO3,” *J. Chem. Phys.,* vol. 24, no. 6, pp. 1236-1239, 2004.

[44] Y. Kawazoe, T. Kanomata and R. Note, “o-YbMnO3 (Synthesized Under Pressure),” in *High Pressure Materials Properties: Magnetic Properties of Oxides Under Pressure*, Springer Berlin Heidelberg, 2023, pp. 683--685.

[45] M. P. Attfield, P. D. Battle, S. K. Bollen, T. C. Gibb and R. J. Whitehead, “The crystal structure and magnetic properties of SrLaFeSnO6 and SrLaNiSbO6,” *Journal of Solid State Chemistry,* vol. 100, no. 1, pp. 37-48, 1992.

[46] W. A. Groen and D. J. W. IJdo, “The monoclinic perovskites Sr2CaUO6 and Ba2SrUO6. A Rietveld refinement of neutron powder diffraction data,” *Acta Cryst.,* vol. C43, pp. 1033-1036, 1987.

[47] P. D. Battle and W. J. Macklin, “The crystal and magnetic structures of Sr2YRuO6,” *Journal of Solid State Chemistry,* vol. 52, no. 2, pp. 138-145, 1984.

[48] P. M. Woodward, “Octahedral Tilting in Perovskites. I. Geometrical Considerations,” *Acta Cryst.,* vol. B53, pp. 32-43, 1997.

[49] W. Liu, R. Cong, A. P. Reyes, I. R. Fisher and V. F. Mitrovic, “Nature of lattice distortions in the cubic double perovskite Ba2NaOsO6,” *Phys. Rev. B,* vol. 97, no. 22, p. 224103, 2018.

[50] E. K. Albrecht and A. J. Karttunen, “Structural principles of cation ordering and octahedral tilting in A-site ordered double perovskites: ferroelectric CaMnTi2O6 as a model system,” *Dalton Trans.,* vol. 51, no. 43, pp. 16508-16516, 2022.

[51] W. Yi, I. A. Presniakov, A. V. Sobolev, Y. S. Glazkova, Y. Matsushita, M. Tanaka, K. Kosuda, Y. Tsujimoto, K. Yamaura and A. A. Belik, “Structure and cation distribution in perovskites with small cations at the A site: the case of ScCoO3,” *Science and Technology of Advanced Materials,* vol. 16, no. 2, p. 024801, 2015.

[52] A. Hossain, P. Bandyopadhyay and S. Roy, “An overview of double perovskites A2B'B"O6 with small ions at A site:,” *Journal of Alloys and Compounds,* vol. 740, pp. 414-427, 2018.

[53] A. M. Glazer, “The classification of tilted octahedra in perovskites,” *Acta Cryst.,* vol. B28, pp. 3384-3392, 1972.

[54] W. T. Fu and D. J. W. IJdo, “New insight into the symmetry and the structure of the double perovskites Ba2LnNbO6 (Ln=lanthanides and Y),” *Journal of Solid State Chemistry,* vol. 179, no. 4, pp. 1022-1028, 2006.

[55] M. Celeba, D. Zagorac, K. Batalovic, J. Radakovic, B. Stojadinovic, V. Spasojevic and R. Hercigonia, “BiFeO3 perovskites: A multidisciplinary approach to multiferroics,” *Ceramics International,* vol. 43, no. 1, pp. 1256-1264, 2017.

[56] H. A. Jahn and E. Teller, “Stability of polyatomic molecules in degenerate electronic states - I—Orbital degeneracy,” *Proc. R. Soc. Lond. A,* vol. 161, no. 905, pp. 220-235, 1937.

[57] M. W. Lufaso and P. M. Woodward, “Jahn-Teller distortions, cation ordering and octahedral tilting in perovskites,” *Acta Cryst.,* vol. B60, no. 0108-7681, pp. 10-20, 2004.

[58] D. Iwanaga, Y. Inaguma and M. Itoh, “Crystal Structure and Magnetic Properties of B-Site Ordered Perovskite-type Oxides A2CuB′O6 (A=Ba, Sr; B′=W, Te),” *Journal of Solid State Chemistry,* vol. 147, no. 1, pp. 291-295, 1999.

[59] M. Tachibana, T. Shimoyama, H. Kawaji, T. Atake and E. Takayama-Muromachi, “Jahn-Teller distortion and magnetic transitions in perovskite RMnO3 (R=Ho, Er, Tm, Yb, and Lu),” *Phys. Rev. B,* vol. 75, no. 14, p. 144425, 2007.

[60] F.-K. Chiang, M.-V. Chu, F. C. Chou, H. T. Jeng, H. S. Sheu, F. R. Chen and C. H. Chen, “Effect of Jahn-Teller distortion on magnetic ordering in Dy(Fe,Mn)O3 perovskites,” *Phys. Rev. B,* vol. 83, no. 24, p. 245105, 2011.

[61] G. A. Gehring and K. A. Gehring, “Co-operative Jahn-Teller effects,” *Reports on Progress in Physics,* vol. 38, no. 1, p. 1, 1975.

[62] W. J. Kim, M. A. Smeaton, C. Jia, B. H. Goodge, B.-G. Cho, K. Lee, M. Osada, D. Jost, A. V. Ievlev, B. Moritz, L. F. Kourkoutis, T. P. Devereaux and H. Y. Hwang, “Geometric frustration of Jahn–Teller order in the infinite-layer lattice,” *Nature,* vol. 615, no. 7951, pp. 237-243, 2023.

[63] J. B. Neaton, C. Ederer, U. V. Waghmare, N. A. Spaldin and K. M. Rabe, “First-principles study of spontaneous polarization in multiferroic BiFeO3,” *Phys. Rev. B,* vol. 71, no. 1, p. 014113, 2005.

[64] R. Seshadri and N. A. Hill, “Visualizing the Role of Bi 6s “Lone Pairs” in the Off-Center Distortion in Ferromagnetic BiMnO3,” *Chemistry of Materials,* vol. 13, no. 9, p. 2892, 2001.

[65] R. Cohen, “Origin of ferroelectricity in perovskite oxides,” *Nature,* vol. 358, no. 6382, p. 136, 1992.

[66] D. Delmonte, F. Mezzadri, C. Pernechele, G. Calestani, G. Spina, M. Lantieri, M. Solzi, R. Cabassi, F. Bolzoni, A. Migliori, C. RItter and E. Gilioli, “Thermally activated magnetization reversal in bulk BiFe0.5Mn0.5O3,” *Phys. Rev. B,* vol. 88, no. 1, p. 014431, 2013.

[67] M. Etter, M. Isobe, H. Sakurai, A. Yaresko, R. E. Dinnebier and H. Takagi, “Charge disproportionation of mixed-valent Cr triggered by Bi lone-pair effect in the A-site-ordered perovskite BiC3Cr4O12,” *Phys. Rev. B,* vol. 97, no. 19, p. 195111, 2018.

[68] V. F. Michel, T. Esswein and N. A. Spaldin, “Interplay between ferroelectricity and metallicity in BaTiO3,” *J. Mater. Chem. C,* vol. 9, pp. 8640-8649, 2021.

[69] C. Kittel, Introduction to solid state physics, John Wiley & sons, 1953.

[70] S. Moharana, T. Badapanda, S. Kumar Satpathy, R. N. Mahaling and R. Kumar, Perovskite Metal Oxides, Elsevier Science, 2023.

[71] L. Brillouin, “Les électrons libres dans les métaux et le role des réflexions de Bragg,” *J. Phys. Radium,* vol. 1, no. 11, pp. 377-400, 1930.

[72] J. Wu, H. Zhang, N. Meng, V. Koval, A. Mahajan, Z. Gao, D. Zhang and H. Yan, “Perovskite Bi0.5Na0.5TiO3-based materials for dielectric capacitors with ultrahigh thermal stability,” *Materials & Design,* vol. 198, p. 109344, 2021.

[73] L. Zhu, X. Shang, K. Lei, C. Wu, S. Zheng, C. Chen and H. Song, “Doping in Semiconductor Oxides-Based Electron Transport Materials for Perovskite Solar Cells Application,” *Solar RRL,* vol. 5, no. 3, p. 2000605, 2021.

[74] A. Thind, S. Kavadiya, M. Kouhnavard, R. Wheelus, S. B. Cho, L.-Y. Lin, C. Kacica, H. K. Mulmudi, K. A. Unocic, A. Y. Borisevich, G. Pilania, P. Biswas and R. Mishra, “KBaTeBiO6: A Lead-Free, Inorganic Double-Perovskite Semiconductor for Photovoltaic Applications,” *Chem. Mater.,* vol. 31, no. 13, pp. 4769-4778, 2019.

[75] G. Abiram, M. Thanihaichelvan, P. Ravirajan and D. Velauthapillai, “Review on Perovskite Semiconductor Field-Effect Transistors and Their Applications,” *Nanomaterials,* vol. 12, no. 14, 2022.

[76] A. Guerrero and J. Bisquert, “Perovskite semiconductors for photoelectrochemical water splitting applications,” *Current Opinion in Electrochemistry,* vol. 2, no. 1, pp. 144-147, 2017.

[77] F. Deschler, D. Neher and L. Schmidt-Mende, “Perovskite semiconductors for next generation optoelectronic applications,” *APL Materials,* vol. 7, no. 8, p. 080401, 2019.

[78] J. Androulakis, N. Katsarakis, J. Giapintzakis, N. Vouroutzis, E. Pavlidou, K. Chrissafis, E. K. Polychroniadis and V. Perdikatsis, “LaSrMnCoO6: a new cubic double perovskite oxide,” *Journal of Solid State Chemistry,* vol. 173, no. 2, pp. 350-354, 2003.

[79] R. Mukherjee, B. Ghosh, S. Saha, C. Bharti and T. P. Sinha, “Structural and electrical transport properties of a rare earth double perovskite oxide: Ba2ErNbO6,” *Journal of Rare Earths,* vol. 32, no. 4, pp. 334-342, 2014.

[80] H. Ullmann and N. Trofimenko, “Composition, structure and transport properties of perovskite-type oxides,” *Solid State Ionics,* vol. 119, no. 1-4, pp. 1-8, 1999.

[81] F. Bridges , L. Downward , J. J. Neumeier and T. A. Tyson , “Detailed relationship between local structure, polarons, and magnetization for La1−xCaxMnO3 ($0.21 \geq x \geq 0.45$),” *Phys. Rev. B: Condens. Matter Mater. Phys.,* vol. 81, no. 18, p. 184401, 2010.

[82] S. Mollah, Z. A. Khan, D. K. Shukla, M. Arshad, R. Kumar and A. Das, “Adiabatic small polaron-hopping conduction in Ln0.85Ca0.15MnO3 (Ln=Nd, Pr and Sm) perovskites,” *Journal of Physics and Chemistry of Solids,* vol. 69, no. 4, pp. 1023-1028, 2008.

[83] K. P. Mohamed Jibri, J. Archana, M. Navaneethan and S. Harish, “Small polaron hopping conduction mechanism and enhanced thermoelectric power factor in the perovskite LaCoO3 ceramic,” *Phys. Chem. Chem. Phys.,* vol. 25, no. 18, pp. 12914-12922, 2023.

[84] B. Fisher, J. Genossar, K. B. Chashka, A. Knizhnik, L. Knizhnik and G. M. Reisner, “Variable range hopping in A2MnReO6 (A= Ca, Sr, Ba),” *J. Appl. Phys.,* vol. 104, no. 3, p. 033716, 2008.

[85] P. M. Woodward, J. Goldberger, M. W. Stoltzfus, H. W. Eng, R. A. Ricciardo, P. N. Santhosh, P. Karen and A. R. Moodenbaugh, “Electronic, Magnetic, and Structural Properties of Sr2MnRuO6 and LaSrMnRuO6 Double Perovskites,” *Journal of the American Ceramic Society,* vol. 91, no. 6, pp. 1796-1806, 2008.

[86] K. Aswathi, J. P Palakkal, P. N. Lekshmi and M. R Varma, “A Griffiths-like phase and variable range hopping of polarons in orthorhombic perovskite Pr2CrMnO6,” *New J. Chem.,* vol. 43, no. 44, pp. 17351-17357, 2019.

[87] T. Okugawa, K. Ohno, Y. Noda and S. Nakamura, “Weakly spin-dependent band structures of antiferromagnetic perovskite LaMO3 (M = Cr, Mn, Fe),” *Journal of Physics: Condensed Matter,* vol. 30, no. 7, p. 075502, 2018.

[88] Y. K. Wakabayashi, K. Yoshiharu, T. Naoto, B. Tommy, T. Shinji, T. Yoshitaka and Y. Hideki, "Ferromagnetism above 1000 K in a highly cation-ordered double-perovskite insulator Sr3OsO6," *Nature Communications,* vol. 10, no. 1, p. 535, 2019.

[89] E. Solana-Madruga, P. S. Kearins, C. Ritter, A. M. Kearins and J. P. Attfield, "1 : 1 Ca2+ :Cu2+ A-site Order in a Ferrimagnetic Double Double Perovskite," *Angew Chem Int Ed Engl,* 2022.

[90] J. B. Goodenough, "Theory of the Role of Covalence in the Perovskite-Type Manganites [La, M(II)]MnO3," *Phys. Rev.,* vol. 100, no. 2, pp. 564-573, 1955.

[91] J. Kanamori, "Superexchange interaction and symmetry properties of electron orbitals," *Journal of Physics and Chemistry of Solids,* vol. 10, no. 2-3, pp. 87-98, 1959.

[92] P. W. Anderson, "Antiferromagnetism. Theory of Superexchange Interaction," *Phys. Rev.,* vol. 79, no. 2, pp. 350-356, 1950.

[93] J. H. Van Vleck, "The Dirac Vector Model in Complex Spectra," *Phys. Rev.,* vol. 45, no. 6, pp. 405-419, 1934.

[94] H. Weihe and H. U. Güdel, "Quantitative Interpretation of the Goodenough−Kanamori Rules: A Critical Analysis," *Inorg. Chem.,* vol. 36, no. 17, pp. 3632-3639, 1997.

[95] R. P. Madhogaria, N. S. Bingham, R. Das, M.-H. Phan and H. Srikanth, "Competing magnetic interactions and emergent phase diagrams in double perovskite Y2NixCo1−xMnO6," *Journal of Alloys and Compounds,* vol. 888, p. 161624, 2021.

[96] A. Paul Blessington Selvadurai, V. Pazhanivelu, C. Jagadeeshwaran, R. Murugaraj, I. Panneer Muthuselvam and F. C. Chou, "Influence of Cr substitution on structural, magnetic and electrical conductivity spectra of LaFeO3," *Journal of Alloys and Compounds,* vol. 646, pp. 924-931, 2015.

[97] J. L. García-Muñoz, J. Rodríguez-Carvajal and P. Lacorre, "Neutron-diffraction study of the magnetic ordering in the insulating regime of the perovskites RNiO3 (R=Pr and Nd)," *Phys. Rev. B,* vol. 50, no. 2, pp. 978-992, 1994.

[98] I. Dzyaloshinsky, "A thermodynamic theory of "weak" ferromagnetism of antiferromagnetics," *Journal of Physics and Chemistry of Solids,* vol. 4, no. 4, pp. 241-255, 1958.

[99] T. Moriya, "Anisotropic Superexchange Interaction and Weak Ferromagnetism," *Phys. Rev.,* vol. 120, no. 1, pp. 91-98, 1960.

[100] C. Weingart, N. A. Spaldin and E. Bousquet, "Noncollinear magnetism and single-ion anisotropy in multiferroic perovskites," *Phys. Rev. B,* vol. 86, no. 9, p. 094413, 2012.

[101] A. J. Dos Santos-García, C. Ritter, E. Solana-Madruga and R. Sáez-Puche, "Magnetic and crystal structure determination of Mn2FeSbO6 double perovskite," *J. Phys.: Condens. Matter,* vol. 25, p. 206004, 2013.

[102] Á. M. Arévalo-López, E. Solana-Madruga, C. Aguilar-Maldonado, C. Ritter, O. Mentré and J. P. Attfield, "Magnetic frustration in the high-pressure Mn2MnTeO6 (Mn3TeO6-II) double perovskite," *Chem. Commun.,* vol. 55, no. 96, pp. 14470-14473, 2019.

[103] K. Ji, R. Chen, P. Manuel and J. P. Attfield, "Coexisting commensurate and incommensurate magnetic orders in the double double perovskite CaMnCoWO6," *Z. Anorg. Allg. Chem.,* vol. 649, no. 15, 2023.

[104] J.-W. Cai, C. Wang, B.-G. Shen, J.-G. Zhao and W.-S. Zhan, "Colossal magnetoresistance of spin-glass perovskite La0.67Ca0.33Mn0.9Fe0.1O3," *Applied Physics Letters,* vol. 71, no. 12, pp. 1727-1729, 1997.

[105] R. Pradheesh, H. S. Nair, C. M. N. Kumar, J. Lamsal, R. Nirmala, P. N. Santhosh, W. B. Yelon, S. K. Malik, V. Sankaranarayanan and K. Sethupathi, "Observation of spin glass state in weakly ferromagnetic Sr2FeCoO6 double perovskite," *Journal of Applied Physics,* vol. 111, no. 5, p. 053905, 2012.

[106] P. Kearins, E. Solana-Madruga, K. Ji, C. Ritter and J. P. Attfield, "Cluster Spin Glass Formation in the Double Double Perovskite CaMnFeTaO6," *J. Phys. Chem. C,* vol. 125, no. 17, pp. 9550-9555, 2021.

[107] J. Guo, S. Wang, W. Li, D. Lu, X. Ye, Z. Liu, S. Qin, X. Wang, Z. Hu, H.-J. Lin, C.-T. Chen, J. Wan, Q. Zhang and Y. Long, "A-site Mn2+ tuned magnetism and electrical transport properties in the transition-metal-only perovskite oxide MnCu3Mn4O12," *Phys. Rev. B,* vol. 105, no. 5, p. 054409, 2022.

[108] V. Celorrio, A. S. Leach, H. Huang, S. Hayama, A. Freeman, D. W. Inwood, D. J. Fermin and A. E. Russell, "Relationship between Mn Oxidation State Changes and Oxygen Reduction Activity in (La,Ca)MnO3 as Probed by In Situ XAS and XES," *ACS Catalysis,* vol. 11, no. 11, pp. 6431-6439, 2021.

[109] C. A. López, M. E. Saleta, J. C. Pedregosa, R. D. Sánchez, J. A. Alonso and M. T. Fernández-Díaz, "Cationic disorder and Mn3+/Mn4+ charge ordering in the B′ and B″ sites of Ca3Mn2NbO9 perovskite: a comparison with Ca3Mn2WO9," *Journal of Solid State Chemistry,* vol. 210, no. 1, pp. 1-9, 2014.

[110] C. E. Frank, M. Emma E., F. Orlandi, P. Manuel, X. Tan, Z. Deng, M. Croft, V. Cascos, T. Emge, H. L. Feng, S. Lapidus, C. Jin, M. Wu, M. R. Li, S. Ehrlich, S. Khalid, N. Quackenbush, S. Yu, D. Walker and M. Greenblatt, "Mn2CoReO6: a robust multisublattice antiferromagnetic perovskite with small A-site cation," *Chem. Commun.,* vol. 55, no. 23, pp. 3331-3334, 2019.

[111] M. Sharannia, P. Kayser, S. S. Pillai, B. J. Kennedy, M. Avdeev, R. Nirmala and P. N. Santhosh, "Observation of Nd ordering in a novel double perovskite Nd2MgRuO6 with weak exchange interaction at B-site," *Journal of Solid State Chemistry,* vol. 259, pp. 73-78, 2018.

[112] Y. Zhang, Y. Tian, Z. Zhang, Y. Jia, B. Zhang, M. Jiang, J. Wang and Z. Ren, "Magnetic properties and giant cryogenic magnetocaloric effect in B-site ordered antiferromagnetic Gd2MgTiO6 double perovskite oxide," *Acta Materialia,* vol. 226, p. 117669, 2022.

[113] A. A. Belik, Y. Matsushita, M. Tanaka and E. Takayama-Muromachi, "Crystal Structures and Properties of Perovskites ScCrO3 and InCrO3 with Small Ions at the A Site," *Chem. Mater.,* vol. 24, no. 11, pp. 2197-2203, 2012.

[114] W. Yi, Q. Liang, Y. Matsushita, M. Tanaka and A. A. Belik, "High-Pressure Synthesis, Crystal Structure, and Properties of In2NiMnO6 with Antiferromagnetic Order and Field-Induced Phase Transition," *Inorg. Chem.,* vol. 52, no. 24, pp. 14108-14115, 2013.

[115] C. Meyer, P. Ksoll, V. Roddatis and V. Moshnyaga, "Spin-Phonon Coupling in A2BMnO6 (A = La, Pr, Nd, Sm, Gd; B = Co, Ni) Double-Perovskite Thin Films: Impact of the A-Site Cation Radius," *Crystals,* vol. 11, no. 7, 2021.

[116] L. Li and M. Yan, "Recent progress in the development of RE2TMTM'O6 double perovskite oxides for cryogenic magnetic refrigeration," *Journal of Materials Science & Technology,* vol. 136, pp. 1-12, 2023.

[117] A. A. Belik and W. Yi, "High-pressure synthesis, crystal chemistry and physics of perovskites with small cations at the A site," *J. Phys.: Condens. Matter,* vol. 26, no. 16, p. 163201, 2014.

[118] W. Dong, A. Yaqub, N. K. Janjua, R. Raza, M. Afzal and B. Zhu, "All in One Multifunctional Perovskite Material for Next Generation SOFC," *Electrochimica Acta,* vol. 193, pp. 225-230, 2016.

[119] R. Shen, J. Nie, K. Wang, Y. Xiang and B. Wang, "Applying multifunctional perovskite LaNiO3 as electrolyte and anode for low-temperature solid oxide fuel cell," *Journal of Materials Science: Materials in Electronics,* vol. 32, no. 4, pp. 4196-4204, 2021.

[120] O. Jongprateep, N. Sato, R. Techapiesancharoenkij, K. Surawathanawises, P. Siwayaprahm and P. Watthanarat, "Photocatalytic and antimicrobial activities of SrxCa1-xTiO3 (x=0, 0.25, 0.5, 0.75 and 1) powders synthesized by solution combustion technique," *J Met Mater Miner,* vol. 29, no. 3, 2019.

[121] K.-I. Kobayashi, T. Kimura, H. Sawada, K. Terakura and Y. Tokura, "Room-temperature magnetoresistance in an oxide material with an ordered double-perovskite structure," *Nature,* vol. 395, no. 6703, pp. 677-680, 1998.

[122] O. Chmaissem, B. Dabrowski, S. Kolesnik, S. Short and J. D. Jorgensen, "Nuclear and magnetic structural properties of Ba2FeMoO6," *Phys. Rev. B,* vol. 71, no. 17, p. 174421, 2005.

[123] R. Nechache, C. Harnagea, S. Li, L. Cardenas, W. Huang, J. Chakrabartty and F. Rosei, "Bandgap tuning of multiferroic oxide solar cells," *Nature Photonics,* vol. 9, pp. 61 - 67, 2014.

[124] N. A. Spaladin, S.-W. Cheong and R. Ramesh, "Multiferroics: Past, present, and future," *Physic Today,* vol. 63, no. 10, pp. 38-43, 2010.

[125] A. V. Shubnikov, Symmetry and antisymmetry of finite figures, Moscow: USSR Academy of Sciences , 1951.

[126] M. Azuma, K. Takata, T. Saito, S. Ishiwata, Y. Shimakawa and M. Takano, "Designed Ferromagnetic, Ferroelectric Bi2NiMnO6," *J. Am. Chem. Soc.,* vol. 127, no. 24, p. 8889–8892, 2005.

[127] M. Fiebig, "Revival of the magnetoelectric effect," *J. Phys. D: Appl. Phys.,* vol. 38, no. 8, 2005.

[128] L. D. Landau and E. Lifshitz, Electrodynamics of continuous media, Pergamon Press, 1960.

[129] R. M. Hazen, The New Alchemists: Breaking through the Barriers of High Pressure, New York: Times Books, 1993.

[130] N. Kawai and S. Endo, "The Generation of Ultrahigh Hydrostatic Pressures by a Split Sphere Apparatus," *Rev. Sci. Instrum.,* vol. 41, no. 8, p. 1178, 1970.

[131] N. Nishiyama , Y. Wang , T. Sanehira , T. Irifune and M. L. Rivers , "Development of the Multi-anvil Assembly 6-6 for DIA and D-DIA type high-pressure apparatuses," *High Pressure Research,* vol. 28, no. 3, p. 307, 2008.

[132] D. Walker, M. A. Carpenter and C. M. Hitch, "Some simplifications to multianvil devices for high pressure experiments," *American Mineralogist,* vol. 75, no. 9-10, pp. 1020-1028, 1990.

[133] D. Walker, "Lubrication, gasketing, and precision in multianvil experiments," *American Mineralogist,* vol. 76, pp. 1092-1100, 1991.

[134] E. Montanari, L. Righi, G. Calestani, A. Migliori, E. Gilioli and F. Bolzoni, "Room Temperature Polymorphism in Metastable BiMnO3 Prepared by High-Pressure Synthesis," *Chem. Mater.,* vol. 17, no. 7, p. 1765–1773, 2005.

[135] C. Goujon, C. Darie, M. Bacia, H. Klein, L. Ortega and P. Bordet, "High pressure synthesis of BiCrO3, a candidate for multiferroism," *J. Phys.: Conf. Ser.,* vol. 121, p. 022009, 2008.

[136] J. Chadwick, "Possible Existence of a Neutron," *Nature,* vol. 129, no. 3252, p. 312, 1932.

[137] L. Chapon, P. Manuel, C. Benson, L. Perrott, S. Ansell, N. Rhodes, D. Raspino, D. Duxbury, E. Spill and J. Norris, "Wish: The new powder and single crystal magnetic diffractometer on the second target station," *Neutron News,* vol. 22, no. 2, p. 22–25, 2011.

[138] V. K. Pecharsky and P. Y. Zavalij, Fundamentals of Powder Diffraction and Structural Characterization of Materials, Second Edition, Springer, 2008.

[139] W. I. F. David, Structure Determination from Powder Diffraction Data, Oxford University Press, 2002.

[140] International Tables for Crystallography, Volume A, Space-group symmetry., Wiley, 2016.

[141] A. Le Bail, H. Duroy and J. L. Fourquet, "Ab initio structure determination of LiSbWO6 by X-ray," *Mat. Res. Bull.,* vol. 23, no. 3, pp. 447-452, 1988.

[142] G. S. Pawley, "Unit-cell refinement from powder diffraction scans," *Journal of Applied Crystallography,* vol. 14, no. 6, pp. 357--361, 1981.

[143] H. M. Rietveld, "A profile refinement method for nuclear and magnetic structures," *J. Appl. Cryst.,* vol. 2, no. 2, pp. 65-71, 1969.

[144] D. B. Litvin, Magnetic Group Tables, 1-, 2- and 3-Dimensional Magnetic Subperiodic Groups and Magnetic Space Groups.

[145] J. Rodríguez-Carvajal, "Recent advances in magnetic structure determination by neutron powder diffraction," *Physica B: Condensed Matter,* vol. 192, no. 1-2, pp. 55-69, 1993.

[146] A. Altomare, C. Cuocci, C. Giacovazzo, A. Moliterni, R. Rizzi, N. Corriero and A. Falcicchio, "EXPO2013: a kit of tools for phasing crystal structures from powder data," *Journal of Applied Crystallography,* vol. 46, no. 4, pp. 1231--1235, 2013.

[147] W. Kraus and G. Nolze, "POWDER CELL - a program for the representation and manipulation of crystal structures and calculation of the resulting X-ray powder patterns," *Journal of Applied Crystallography,* vol. 29, no. 3, pp. 301--303, 1996.

[148] B. H. Toby and R. B. Von Dreele, "GSAS-II: the genesis of a modern open-source all purpose crystallography software package," *Journal of Applied Crystallography,* vol. 46, no. 2, pp. 544-549, 2013.

[149] V. Petříček, L. Palatinus, J. Plášil and M. Dušek, "Jana2020 – a new version of the crystallographic computing system Jana," *Zeitschrift für Kristallographie - Crystalline Materials,* vol. 238, no. 7-8, pp. 271-282, 2023.

[150] D. B. William and C. B. Carter, Transmission Electron Microscopy, Springer, 1996.

[151] S. V. Kalinin, C. Ophus, P. M. Voyles, R. Erni, D. Kepaptsoglou, V. Grillo, A. R. Lupini, M. P. Oxley, E. Schwenker, M. K. Y. Chan, J. Etheridge, X. Li, G. G. D. Han, M. Ziatdinov, N. Shibata and S. J. Pennycook, "Machine learning in scanning transmission electron microscopy," *Nature Reviews Methods Primers,* vol. 2, no. 1, p. 11, 2022.

[152] E. Rotunno, A. H. Tavabi, P. Rosi, S. Frabboni, P. Tiemeijer, R. E. Dunin-Borkowski and V. Grillo, "Alignment of electron optical beam shaping elements using a convolutional neural network," *Ultramicroscopy,* vol. 228, p. 113338, 2021.

[153] "DigitalMicrograph Software," [Online]. Available: https://gatan.com/products/tem-analysis/gatan-microscopy-suite-software#resources.

[154] G. Allodi, A. Banderini, R. De Renzi and C. Vignali, "HyReSpect: A broadband fast-averaging spectrometer for nuclear magnetic resonance of magnetic materials," *Rev. Sci. Instrum.,* vol. 76, no. 8, p. 083911, 2005.

[155] G. Allodi, R. De Renzi, K. Zheng, S. Sanna, A. Sidorenko, C. Baumann, L. Righi, F. Orlandi and G. Calestani, "Band filling effect on polaron localization in La1−x(CaySr1−y)xMnO3 manganites," *Journal of Physics: Condensed Matter,* vol. 26, no. 26, p. 266004, 2014.

[156] N. A. Hill, "Why Are There so Few Magnetic Ferroelectrics?," *The Journal of Physical Chemistry B,* vol. 104, no. 29, pp. 6694-6709, 2000.

[157] M. Guennou, M. Viret and J. Kreisel, "Bismuth-based perovskites as multiferroics," *Comptes Rendus Physique,* vol. 16, no. 2, pp. 182-192, 2015.

[158] A. V. Sobolev, A. V. Bokov, W. Yi, A. A. Belik, I. A. Presniakov and I. S. Glazkova, "Electric Hyperfine Interactions of 57Fe Impurity Atoms in ACrO3 Perovskite-Type Chromites (A = Sc, In, Tl, Bi)," *Soviet Journal of Experimental and Theoretical Physics,* vol. 129, no. 5, pp. 896-902, 2019.

[159] D. V. Karpinsky, M. V. Silibin, S. I. Latushka, D. V. Zhaludkevich, V. V. Sikolenko, H. Al-Ghamdi, A. H. Almuqrin, M. I. Sayyed and A. A. Belik, "Structural and Magnetic Phase Transitions in BiFe1-xMnxO3 Solid Solution Driven by Temperature," *Nanomaterials,* vol. 12, no. 9, p. 1565, 2022.

[160] G. Catalan and J. F. Scott, "Physics and Applications of Bismuth Ferrite," *Advanced Materials,* vol. 21, no. 24, pp. 2463-2485, 2009.

[161] A. K. Pradhan, K. Zhang, D. Hunter, J. B. Dadson, G. B. Loiutts, P. Bhattacharya, R. Katiyar, J. Zhang, D. J. Sellmyer, U. N. Roy, Y. Cui and A. Burger, "Magnetic and electrical properties of single-phase multiferroic BiFeO3," *Journal of Applied Physics,* vol. 97, no. 9, p. 093903, 2005.

[162] J. Silva, A. Reyes, H. Esparza, H. Camacho and L. Fuentes, "BiFeO3: A Review on Synthesis, Doping and Crystal Structure," *Integrated Ferroelectrics,* vol. 126, no. 1, pp. 47-59, 2011.

[163] J. Lu, A. Günther, F. Schrettle, F. Mayr, S. Krohns, P. Lunkenheimer, A. Pimenov, V. D. Travkin, A. A. Mukhin and A. Loidl, "On the room temperature multiferroic BiFeO3: magnetic,dielectric and thermal properties," *The European Physical Journal B,* vol. 75, no. 4, pp. 451-460, 2010.

[164] P. Baettig, R. Seshadri and N. A. Spaldin, "Anti-Polarity in Ideal BiMnO3," *J. Am. Chem. Soc.,* vol. 129, no. 32, pp. 9854-9855, 2007.

[165] P. Mandal, A. Sundaresan, C. N. R. Rao, A. Iyo, P. M. Shirage, Y. Tanaka, C. Simon, V. Pralong, O. I. Lebedev, V. Caignaert and B. Raveau, "Temperature-induced magnetization reversal in BiFe0.5Mn0.5O3 synthesized at high pressure," *Phys. Rev. B,* vol. 82, no. 10, p. 100416, 2010.

[166] A. A. Belik, "Origin of Magnetization Reversal and Exchange Bias Phenomena in Solid Solutions of BiFeO3–BiMnO3: Intrinsic or Extrinsic?," *Inorg. Chem.,* vol. 52, no. 4, pp. 2015-2021, 2013.

[167] D. Delmonte, F. Mezzadri, C. Pernechele, E. Gilioli, G. Calestani, R. Cabassi, F. Bolzoni, G. Spina, M. Lantieri and M. Solzi, "Field effects on spontaneous magnetization reversal of bulk BiFe0.5Mn0.5O3, an effective strategy for the study of magnetic disordered systems," *Journal of Physics: Condensed Matter,* vol. 27, no. 28, p. 286002, 2015.

[168] D. Delmonte, F. Mezzadri, E. Gilioli, M. Solzi, G. Calestani, F. Bolzoni and R. Cabassi, "Poling-Written Ferroelectricity in Bulk Multiferroic Double-Perovskite," *Inorg Chem,* vol. 55, no. 12, pp. 6308-14, 2016.

[169] R. D. Shannon, "Revised Effective Ionic Radii and Systematic Studies of Interatomic Distances in Halides and Chalcogenides," *Acta Cryst.,* vol. A32, pp. 751-767, 1976.

[170] D. L. Corker, A. M. Glazer, J. Dec, K. Roleder and R. W. Whatmore, "A Re-investigation of the Crystal Structure of the Perovskite PbZrO3 by X-ray and Neutron Diffraction," *Acta Crystallographica Section B,* vol. 53, no. 1, pp. 135--142, 1997.

[171] H. Shen, Z. Cheng, F. Hong, J. Xu, S. Yuan, S. Cao and X. Wang, "Magnetic field induced discontinuous spin reorientation in ErFeO3 single crystal," *2013,* vol. 103, no. 19, p. 192404, Applied Physics Letters.

[172] J. H. Hu and H. L. Johnston, "Low Temperature Heat Capacities of Inorganic Solids. XVI. Heat Capacity of Cupric Oxide from 15 to 300° K," *Journal of the American Chemical Society,* vol. 75, no. 10, pp. 2471-2473, 1953.

[173] S. B. Ota and E. Gmelin, "Incommensurate antiferromagnetism in copper(II) oxide: Specific-heat study in a magnetic field," *Phys. Rev. B,* vol. 46, no. 18, pp. 11632--11635, 1992.

[174] H. T. Stokes, D. M. Hatch and B. J. Campbell, "ISODISPLACE: An Internet Tool for Exploring Structural Distortions.," *J. Appl. Cryst.,* vol. 39, pp. 607-614, 2006.

[175] M. Ain, A. Menelle, B. M. Wanklyn and E. F. Bertaut, "Magnetic structure of CuO by neutron diffraction with polarization analysis," *Journal of Physics: Condensed Matter,* vol. 4, no. 23, p. 5327, 1992.

[176] C. A. M. Mulder, A. J. van Duyneveldt and J. A. Mydosh, "Susceptibility of the CuMn spin-glass: Frequency and field dependences," *Phys. Rev. B,* vol. 23, no. 3, pp. 1384--1396, 1981.

[177] A. N. Ulyanov, H. D. Quang, K. W. Lee, S. C. Yu, N. H. Sinh, Y. M. Kang and S. I. Yoo, "Magnetic Relaxation Behavior in Nd0.5Sr0.5MnO3: Observation of Negative Imaginary Component of ac Magnetic Susceptibility," *IEEE Transactions on Magnetics,* vol. 44, no. 11, pp. 3060-3062, 2008.

[178] Y. Tomioka, T. Okuda, Y. Okimoto, R. Kumai, K.-Y. Kobayashi and Y. Tokura, "Magnetic and electronic properties of a single crystal of ordered double perovskite Sr2FeMoO6," *Phys. Rev. B,* vol. 61, no. 1, pp. 422--427, 2000.

[179] J. Navarro, L. Balcells, F. Sandiumenge, M. Bibes, A. Roig, B. Martínez and J. Fontcuberta, "Antisite defects and magnetoresistance in Sr2FeMoO6 double perovskite," *Journal of Physics: Condensed Matter,* vol. 13, no. 37, p. 8481, 2001.

[180] R. P. Panguluri, S. Xu, Y. Moritomo, I. V. Solovyev and B. Nadgorny, "Disorder effects in half-metallic Sr2FeMoO6 single crystals," *Appl. Phys. Lett.,* vol. 94, no. 1, p. 012501, 2009.

[181] V. N. Singh and P. Majumdar, "Antiferromagnetic order and phase coexistence in a model of antisite disordered double perovskites," *The European Physical Journal B,* vol. 83, no. 2, p. 147, 2011.

[182] M. Retuerto , M. J. Martínez-Lope, M. García-Hernández and J. A.-. Alonso , "High-pressure synthesis of the double perovskite Sr(2)FeMoO(6): increment of the cationic ordering and enhanced magnetic properties," *J Phys Condens Matter.,* vol. 21, no. 18, p. 186003, 2009.

[183] D. Sanchez, J. A. Alonso, M. Garcia-Hernandez, M. J. Martinez-Lope, J. L. Martinez and A. Mellergard, "Origin of neutron magnetic scattering in antisite-disordered Sr2FeMoO6 double perovskites," *Phys. Rev. B,* vol. 65, no. 10, p. 104426, 2002.

[184] X. Yuan, M. Xu and Y. Chen, "Magnetic properties and magnetoresistance effect of Pb2FeMoO6," *Appl. Phys. Lett.,* vol. 113, no. 5, p. 052411, 2013.

[185] W. Xie, S. Zhu, X. Tang, J. He, Y. Yan, V. Ponnambalam, Q. Zhang, S. J. Poon and T. Tritt, "Synthesis and thermoelectric properties of (Ti,Zr,Hf)(Co,Pd)Sb half-Heusler compounds," *Journal of Physics D: Applied Physics,* vol. 42, no. 23, p. 235407, 2009.

[186] A. Biswas and Y. H. Jeong, "Persistent semi-metal-like nature of epitaxial perovskite CaIrO3 thin films," *Journal of Applied Physics,* vol. 117, no. 19, p. 195305, 2015.

[187] S. Chatterjee, S. Chatterjee, S. Giri and S. Majumdar, "Transport properties of Heusler compounds and alloys," *Journal of Physics: Condensed Matter,* vol. 34, no. 1, p. 013001, 2021.

[188] Q. Tang and X. Zhu, “Half-metallic double perovskite oxides: recent developments and future perspectives,” *J. Mater. Chem. C,* vol. 10, no. 41, pp. 15301-15338, 2022.

[189] X. H. Liu, C. F. Chang, L. H. Tjeng, A. C. Komarek and S. Wirth, “Large magnetoresistance effects in Fe3O4,” *Journal of Physics: Condensed Matter,* vol. 31, no. 22, p. 225803, 2019.

[190] R. Han, W. Li and W. Pan, “1D Magnetic Materials of Fe3O4 and Fe with High Performance of Microwave Absorption Fabricated by Electrospinning Method.,” *Sci Rep,* vol. 4, no. 7493, 2014.

[191] V. E. Orel, M. Tselepi, T. Mitrelias and M. Zabolotny, “The comparison between superparamagnetic and ferromagnetic iron oxide nanoparticles for cancer nanotherapy in the magnetic resonance system,” *Nanotechnology,* vol. 30, no. 4, p. 415701, 2019.

[192] C. A. Occhialini, G. G. Guzmán-Verri, S. U. Handunkanda and J. N. Hancock, “Negative Thermal Expansion Near the Precipice of Structural Stability in Open Perovskites,” *Frontiers in Chemistry,* vol. 6, 2018.

[193] W.-J. Yin, B. Weng, J. Ge, Q. Sun, Z. Li and Y. Yan, “Oxide perovskites, double perovskites and derivatives for electrocatalysis, photocatalysis, and photovoltaics,” *Energy Environ. Sci.,* vol. 12, pp. 442-462, 2019.

[194] A. B. Christian, Magnetic and Thermal Properties of Low-Dimensional Single-Crystalline Transition-Metal Antimonates and Tantalates, 2017.

[195] W. Gao, C. Addiego, H. Wang, X. Yan, Y. Hou, D. Ji, C. Heikes, Y. Zhang, L. Li, H. Huyan, T. Blum, T. Aoki, Y. Nie, D. G. Schlom, R. Wu and X. Pan, “Real-space charge-density imaging with sub-ångström resolution by four-dimensional electron microscopy,” *Nature,* vol. 575, no. 7783, p. 480–484, 2019.

[196] H. Li, Z. D. Deng and T. Carlson, “Piezoelectric Materials Used in Underwater Acoustic Transducers,” *Sensor Letters,* vol. 10, no. 3-4, pp. 679-697, 2012.

[197] “Fermi Level,” [Online]. Available: https://commons.wikimedia.org/wiki/File:Band_filling_diagram.svg.

[198] “Semimetal,” [Online]. Available: https://en.wikipedia.org/wiki/Semimetal.

[199] S. Shahrokhi, W. Gao, Y. Wang, P. R. Anandan, M. Z. Rahaman, S. Singh, D. Wang, C. Cazorla, G. Yuan, J.-M. Liu and T. Wu, “Emergence of Ferroelectricity in Halide Perovskites,” *Small Methods,* vol. 4, no. 8, p. 2000149, 2020.

[200] Y. Mao, H. Zhou and S. S. Wong, Synthesis, Properties, and Applications of Perovskite - Phase Metal Oxide Nanostructures, 2011.

[201] A. Sharma, Probing non-collinear spin textures using variable temperature magnetic force microscopy, 2022.

[202] "The Multi-Anvil Apparatus," [Online]. Available: https://serc.carleton.edu/msu_nanotech/methods/Multi_Anvil.html .

[203] "LibreTexts Chemistry," [Online]. Available: https://chem.libretexts.org/Bookshelves/Physical_and_Theoretical_Chemistry_Textbook_Maps/Physical_Chemistry_%28LibreTexts%29/31%3A_Solids_and_Surface_Chemistry/31.04%3A_The_Total_Scattering_Intensity_Is_Related_to_the_Periodic_Structure_of_the_Electron_De.

[204] W. T. Heller, "Small-Angle Neutron Scattering for Studying Lipid Bilayer Membranes," *Biomolecules,* vol. 12, no. 11, p. 1591, 2022.

[205] G. E. Pérez , J. M. Brittain, I. McClelland, S. Hull, M. O. Jones, H. Y. Playford, S. A. Cussen, P. J. Baker and E. M. Reynolds, "Neutron and muon characterisation techniques for battery materials," *J. Mater. Chem. A,* vol. 11, pp. 10493-10531, 2023.

[206] I. Chilibon and J. N. Marat-Mendes, "Ferroelectric ceramics by sol–gel methods and applications: a review," *J. Sol-Gel Sci. Technol.,* vol. 64, no. 3, p. 571–611, 201264.

Acknowledgments

I am deeply thankful to Prof. Enrico Dalcanale for his invaluable guidance as my doctoral program Coordinator. His support and insights have greatly influenced my academic journey.

Firstly, I express my heartfelt appreciation to all the collaborators, both internal and external to IMEM-CNR, who dedicated their expertise to conducting extensive measurements on my samples, thereby enriching the content of my doctoral thesis. Special thanks go to Dr. Riccardo Cabassi for his contributions to electrical measurements, Dr. Giovanna Trevisi and Dr. Ferdinando Vescovi for SEM investigations, Dr. Andrea Migliori for TEM analyses, Prof. Massimo Solzi and Dr. Francesco Cugini for their contribution for SQUID measurements, and Dr. Giuseppe Allodi for the very large number of solid-state NMR measurements. Their collective efforts have significantly elevated the quality and depth of my research.

I would like to express my gratitude to the ISIS Neutron and Muon Source (UK) of Science and Technology Facilities Council (STFC) for accepting my experiment proposal (RB2320119) on the WISH diffractometer and the related financial support of Consiglio Nazionale delle Ricerche within CNR-STFC Agreement 2021-2027 (N 0065606). Special thanks to Dr. Fabio Orlandi for his assistance during the measurement and for his invaluable teachings on crystallography and structural magnetism. His guidance was fundamental in the structural resolution process.

My deep appreciation goes to Prof. Francesco Mezzadri for introducing me to the fascinating world of crystallography and igniting my passion for it. His

guidance has shown me the intricacies of this field, emphasizing the importance of patience. Simultaneously, he has made me realize that working in this realm is precisely what I aspire to do in the future.

In this framework, I want to thank all the organizers of the HERCULES 2023 European School of Neutrons and Synchrotron Radiation, for giving me the opportunity to attend this course last year and providing me with the opportunity to greatly expand my knowledge of large-scale facilities. This experience has deeply resonated with me and has left an indelible mark on my academic journey, enriching my professional growth.

Among the IMEM-CNR researchers, I extend my sincere gratitude to Dr. Andrea Zappettini, Director of IMEM-CNR, for giving me the opportunity to undertake my doctoral thesis at his institute in the research group of “Magnetic Materials and Multiferroics”.

Undoubtedly, I wish to express my sincere appreciation to Dr. Laura Lazzarini and Dr. Lucia Nasi for their invaluable guidance and teachings throughout the entire first year of doctoral studies. Their expertise and mentorship in the field of transmission electron microscopy have been instrumental in shaping my understanding of this intricate domain.

Special gratitude is owed to my doctoral supervisor, Dr. Edmondo Gilioli, and to all the Green Energy Group and MatFun Group, for providing me with the opportunity to work in his laboratories and delve into the realm of high-pressure synthesis. I would also like to extend my thanks for the various opportunities he has afforded me, allowing my participation in several international conferences and schools.

And yes, in the end, I have to extend my deepest gratitude to Dr. Davide Delmonte, my “Capetto”, who, willingly or unwillingly, has undeniably played a pivotal role in the success (and rescue!) of my doctoral journey. Under his mentorship, I have not only grown significantly as a scientist, especially learning how to control the evil HP/HT instruments, but, to some extent, as an individual. His mentorship has instilled in me a newfound confidence in myself and my

abilities, as he consistently placed me in challenging situations while always being ready to lend a helping hand. I am profoundly grateful for his unwavering belief in me and for his dedication to my growth and success.

Now, after all these pages, I truly believe that it's time to go back to my mother language for the less formal thanks.

Senza dubbio occorre ringraziare i ragazzi dell'IMEM e dintorni, tra cui Elena e Lorenzo (ovvero i miei colleghi del team "The Procrastinators"), Gianlu, Giulia, Bronz, Nadia, Tiz, Fiore, Elena, Filo, Vitti, Edo, Michele, Manu, Vale, che hanno condiviso con me tanti momenti. Sono stati compagni di sentimenti contrastanti ma anche (fortunatamente) di aperitivi risolutivi.

I miei amici di sempre, Davide, Anna, Ale, Frafi, Mari e Eri, sono stati fondamentali per sostenermi in questo difficile percorso. Con tutti i vari impegni, è diventato più complicato vedersi spesso, ma volevo proprio ringraziarvi di cuore e dirvi che, nonostante la distanza fisica, proprio come siete stati al mio fianco, ci sarò sempre per voi.

In questo contesto, vorrei dare un forte abbraccio al mio papà e alla mia mamma, e chiedergli scusa se non sono stata abbastanza presente in certi momenti. Tutti, lo sappiamo, facciamo degli errori, ma il bello è poter porre rimedio con gli interessi. Grazie per avermi capita, io credo di aver capito voi. Farò del mio meglio, promesso.

E poi c'è Dario. Ho provato a buttare giù qualche riga ma mi sono resa conto che sarebbe riduttivo esprimerti qui la mia gratitudine per essere al mio fianco ogni giorno. Ti avverto che da domani si ricomincia a ballare sulle note di "Hooked on a feeling" in cucina. Ora concludo qui e poi prenoto il campo coperto per domani alle 18.00, brum!

Durante questo dottorato sono cambiate tantissime cose nella mia vita, e non è certo il contesto giusto per farne un elenco. Quello che in sunto posso dire è che, inaspettatamente, mi sento di essere stata molto coraggiosa nell'affrontare e prendere in mano certe situazioni. Brava Chiaretta, hai saputo diventare un po' più grande e, presuntuosamente, migliore, anche soffrendo.

E quindi adesso? Sì, finalmente sottometto.

30th January 2024

Chiara Coppi